



Universiteit
Leiden
The Netherlands

High-frequency EPR on high-spin transitions-metal sites

Mathies, G.

Citation

Mathies, G. (2012, March 1). *High-frequency EPR on high-spin transitions-metal sites*. *Casimir PhD Series*. Retrieved from <https://hdl.handle.net/1887/18552>

Version: Not Applicable (or Unknown)

License: [Leiden University Non-exclusive license](#)

Downloaded from: <https://hdl.handle.net/1887/18552>

Note: To cite this publication please use the final published version (if applicable).

Cover Page



Universiteit Leiden



The handle <http://hdl.handle.net/1887/18552> holds various files of this Leiden University dissertation.

Author: Mathies, Guinevere

Title: High-frequency EPR on high-spin transition-metal sites

Issue Date: 2012-03-01

High-frequency EPR on high-spin transition-metal sites

Guinevere Mathies

High-frequency EPR on high-spin transition-metal sites

PROEFSCHRIFT

ter verkrijging van
de graad van Doctor aan de Universiteit Leiden,
op gezag van de Rector Magnificus prof. mr. P.F. van der Heijden,
volgens besluit van het College voor Promoties
te verdedigen op donderdag 1 maart 2012
klokke 16.15 uur

door

Guinevere Mathies
geboren te Leiden
in 1981

PROMOTIECOMMISSIE

Promotor:	Prof. dr. E. J. J. Groenen	Universiteit Leiden
Leden:	Prof. dr. E. R. Eliel	Universiteit Leiden
	Prof. dr. M. C. van Hemert	Universiteit Leiden
	Prof. dr. W. Lubitz	MPI für Bioanorganische Chemie, Mülheim an der Ruhr
	Prof. dr. J. Schmidt	Universiteit Leiden
	Dr. G. Smith	University of St Andrews
	Prof. dr. J. H. van der Waals	Universiteit Leiden

The work reported in this thesis was carried out at the “Leids Instituut voor Onderzoek in de Natuurkunde” (LION) and was supported with financial aid by The Netherlands Organization for Scientific Research (NWO), Department of Chemical Sciences (CW).

An electronic version of this dissertation is available at the Leiden University Repository (<https://openaccess.leidenuniv.nl>).

ISBN: 978-90-8593-926-9

Casimir PhD Series, Delft-Leiden, 2012-4

Contents

1	Introduction	1
1.1	Electron paramagnetic resonance and the study of transition-metal sites	2
1.2	Thesis outline	7
2	Continuous-wave EPR at 275 GHz: Application to high-spin Fe³⁺ systems	9
2.1	Introduction	10
2.2	Experimental	12
2.2.1	The cw probe head	12
2.2.2	Samples	12
2.3	Results	14
2.3.1	Absolute sensitivity	14
2.3.2	Operating the spectrometer in cw mode	14
2.3.3	High-spin Fe ³⁺ spectra	16
2.4	Analysis	16
2.5	Discussion	21
2.6	Conclusion	23
3	Multi-frequency EPR study of Fe³⁺ and Co²⁺ in the active site of desulforedoxin	25
3.1	Introduction	26
3.2	Materials and methods	27
3.3	Results and analysis	27
3.3.1	Desulforedoxin	27
3.3.2	Co(II)-desulforedoxin	30
3.4	Discussion	33
3.5	Conclusion	39
4	A W-band pulsed EPR/ENDOR study of Co(II)S₄ coordination in the Co[(SPPH₂)(SPⁱPr₂)N]₂ complex	41
4.1	Introduction	42
4.2	Materials and methods	43

Contents

4.3	Theoretical background	44
4.4	Results	45
4.5	Discussion	50
4.6	Conclusion	53
5	High-frequency EPR study of the pseudo-tetrahedral high-spin Fe²⁺ complex Fe[(SPh₂)₂N]₂	55
5.1	Introduction	56
5.2	Materials and methods	57
5.2.1	Sample preparation	57
5.2.2	EPR experiments	57
5.3	Results	58
5.4	Analysis	61
5.5	Discussion	66
5.6	Conclusion	68
6	The two Fe³⁺ binding sites in human serum transferrin distinguished by high-frequency EPR	69
6.1	Introduction	70
6.2	Materials and methods	71
6.3	Results	71
6.4	Analysis	72
6.5	Discussion	75
6.6	Conclusion	76
7	Configuration of spheroidene in the photosynthetic reaction center of <i>Rb. sphaeroides</i>: A comparison of wild type and reconstituted R26	77
7.1	Introduction	78
7.2	Methods	79
7.3	Results and discussion	81
7.4	Conclusion	86
A	Continuous-wave 275.7 GHz EPR spectra of rubredoxin from <i>Pyrococcus furiosus</i> and <i>Megasphaera elsdenii</i>	89
B	The revised mount of the modulation coil of the 275.7 GHz continuous-wave probe head	93
C	EPR spectroscopy on Co(II)-rubredoxin	95
C.1	Introduction	95
C.2	Materials and methods	95
C.3	Results	96

C.4 Discussion	98
D Supporting information on Chapter 7	101
Bibliography	105
Samenvatting	113
List of publications	117
Curriculum vitae	119
Acknowledgement	121

Contents

Chapter 1

Introduction

The phrase “transition-metal sites” in the title of this thesis refers, on the one hand, to the central metal ion bonded to the ligands in transition-metal complexes. On the other hand it refers to metal centers in proteins and enzymes. The unpaired electrons often found at these transition metals make these sites amenable to study by electron-paramagnetic-resonance (EPR) spectroscopy, which is the main subject of this thesis.

The presence of one or more unpaired electrons results in a net spin angular momentum, which causes a Zeeman splitting of the magnetic sublevels of a transition-metal site by an externally applied magnetic field. For a free electron ($S = 1/2$) the splitting of the states with $m_S = \pm 1/2$ is 9.5 GHz at 340 mT. In a typical EPR experiment the paramagnetic material is placed in a cavity and microwaves are applied at a fixed frequency, usually 9.5 GHz or X band. The absorption of the microwaves is detected as the magnetic field is swept. The magnetic sublevels are influenced by the interaction of the unpaired electrons with their environment and hence the observed EPR spectrum provides information on the electronic structure of the transition-metal site.

In a transition-metal site the ligands affect the d electrons of the transition-metal ion through their electrostatic field and covalent bonding. The degeneracy of the five d orbitals is lifted by the ligand field, in accordance with the rules of group theory. The size of the splitting of the d orbitals depends on the strength of the ligand field. If the splitting is much smaller than the Coulomb and exchange energies of the electrons in the free ion, the ground-state electron configuration will have the highest total spin, consistent with the Pauli exclusion principle. This is called the weak-field or high-spin case. If the splitting becomes larger, it becomes favorable to fill up the low-lying d orbitals. This is the strong-field or low-spin case.

High-spin transition-metal sites show a splitting of the $2S + 1$ magnetic sublevels even if no external magnetic field is applied, the zero-field splitting (ZFS). To optimize the amount of information that can be obtained for these sites by EPR spectroscopy, these sites should be studied at microwave frequencies comparable to

1. Introduction

or higher than the ZFS. In this thesis we study high-spin Co^{2+} sites, for which this splitting is very large, approaching 1000 GHz, and high-spin Fe^{2+} and Fe^{3+} sites, for which it tends to be more moderate, between 100 - 400 GHz and < 100 GHz, respectively. We set out to do EPR at frequencies higher than the standard 9.5 GHz, which comes with considerable technical difficulties, particularly if one requires the sensitivity needed to study biological materials.

1.1 Electron paramagnetic resonance and the study of transition-metal sites

An electron-paramagnetic-resonance transition can be induced by applying microwaves continuously, continuous-wave (cw) mode, or by applying microwave pulses. In spite of the enormous flexibility and applicability of pulsed EPR techniques and the current strong development in this field, [1] the larger part of this thesis concerns cw EPR. The main reason is that short relaxation times, which make a study by pulsed EPR impossible, are not uncommon in transition-metal sites. A disadvantage of cw EPR is the need to detect the absorption of the microwaves by the paramagnetic sample using lock-in detection. The modulation of the EPR signal is usually created through modulation of the magnetic field. The problems this entails are described in Chapter 2.

The perturbation of the ground state of a paramagnetic site by the interaction of the unpaired electron(s) with their environment and the magnetic field can be captured in a spin Hamiltonian. [2] Depending on the system various terms are incorporated in the spin Hamiltonian to cover all interactions. The strength of the interactions, which is characteristic of the system and may be anisotropic, is represented by usually symmetric interaction “tensors”. The spin Hamiltonian describing the electronic interactions of the unpaired electrons in a transition-metal site should at least contain the following two terms. [3]

$$H_e = \mu_B \vec{B}_0 \cdot \vec{g} \cdot \vec{S} + \vec{S} \cdot \vec{D} \cdot \vec{S} \quad (1.1)$$

The first term describes the electron Zeeman interaction. The g tensor describes the anisotropic deviation from the free electron value of $g_e = 2.0023$ owing to an orbital angular momentum component contributing to the magnetic moment. The energy levels are perturbed by the spin-orbit coupling, which causes a mixing of the ground state with electronically excited states and partially restores the orbital angular momentum. The second term describes the ZFS, which arises also mainly from the spin-orbit coupling. Because EPR spectroscopy shows transitions between magnetic sublevels, we observe only the anisotropy of this effect. This means that the ZFS tensor can be taken traceless and characterized by two parameters, D and E .

$$D = 3/2D_z, \quad E = 1/2(D_x - D_y) \quad (1.2)$$

1.1. Electron paramagnetic resonance and the study of transition-metal sites

D_x , D_y and D_z are the principal values of \vec{D} . The “rhombicity” of \vec{D} is given by the ratio $\lambda = E/D$.

To observe the orientation of the principal axes of an interaction tensor describing a site, it is necessary to study the site trapped in a crystal. The principal values of the interaction, however, may also be obtained from a powder or frozen solution containing all orientations in equal amounts.

Degenerate perturbation theory is used to establish the eigenstates that will result from the perturbation described by the spin Hamiltonian. Thus, the spin Hamiltonian is expressed in a basis of the unperturbed states, $m_S = \pm 1/2, \dots$, and diagonalized. The EPR spectrum shows transitions between the eigenstates of the spin Hamiltonian.

Kramers’ theorem states that no electrostatic interaction can completely lift the degeneracy of a system containing an odd number of electrons. [4] As a consequence, the sublevels of a half-integer spin system, $S = 1/2, 3/2, 5/2, \dots$, will be split in zero field in so-called Kramers doublets.

The behavior of the four magnetic sublevels of a high-spin Co^{2+} , $S = 3/2$, system between 0 and 0.5 T is shown in Figure 1.1. The X-band transitions are shown by vertical lines. In the field range plotted $\vec{S} \cdot \vec{D} \cdot \vec{S} \gg \mu_B \vec{B}_0 \cdot \vec{g} \cdot \vec{S}$. The eigenvalues and eigenvectors of the dominant ZFS term can be calculated analytically. Two Kramers doublets are found, which are separated in energy by $2\sqrt{D^2 + 3E^2}$.

$$\begin{aligned} |\pm 3/2\rangle &= \cos\theta|3/2, \pm 3/2\rangle + \sin\theta|3/2, \mp 1/2\rangle \\ |\pm 1/2\rangle &= \cos\theta|3/2, \pm 1/2\rangle - \sin\theta|3/2, \mp 3/2\rangle \end{aligned} \quad (1.3)$$

where $\tan 2\theta = \sqrt{3}E/D$. Although m_S is not a “good” quantum number, the two doublets are referred to as $\pm 3/2$ and $\pm 1/2$. “Forbidden” transitions may occur, i.e. transitions that following the qualification of the doublets by m_S do not seem to obey the selection rule $\Delta m_S = \pm 1$.

The Zeeman interaction can be treated as a perturbation on top of the ZFS. The Zeeman term is expressed in a basis of the states given by Equation 1.3 and diagonalized. The result is referred to as the effective $S' = 1/2$ approximation: each of the two doublets can be described by an effective g' tensor. [7] The principal values of this tensor depend on the g -values and λ , but not on D , cf. Chapters 3 and 4.

If a high-spin Fe^{3+} , $S = 5/2$, system is studied at X band, the microwave quantum is not yet large enough to induce inter-doublet transitions, but the effective $S' = 1/2$ approximation starts to break down. However, the high-field limit, $\vec{S} \cdot \vec{D} \cdot \vec{S} \ll \mu_B \vec{B}_0 \cdot \vec{g} \cdot \vec{S}$, comes within the reach of the experimentalist. At high magnetic fields the Zeeman term dominates, which means that, with B_0 in the z direction, m_S is almost a “good” quantum number. Subsequently, the ZFS term may be taken into account using first-order perturbation theory since the degeneracy of the states is

1. Introduction

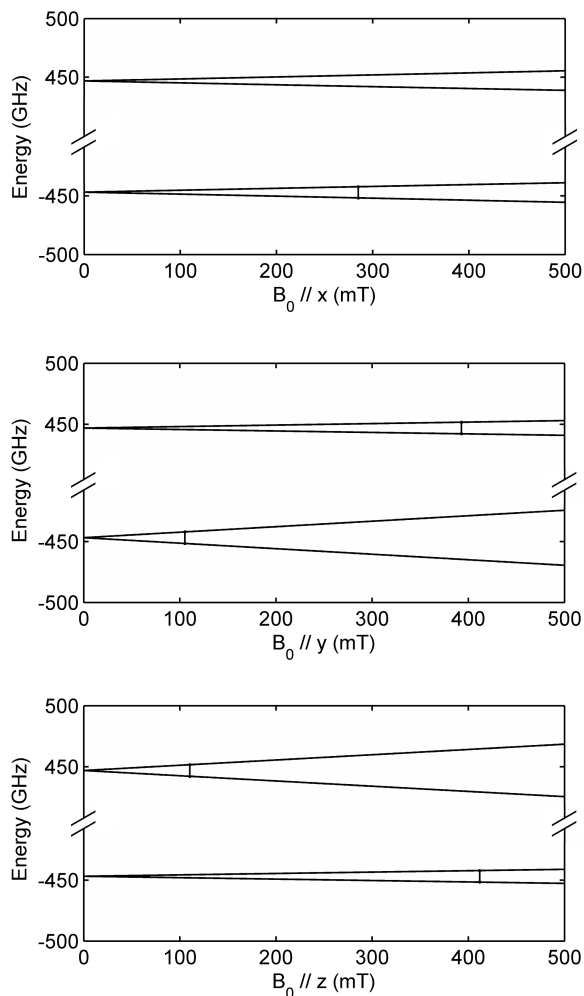


Figure 1.1: The dependence of the energy of the four magnetic sublevels of a high-spin Co^{2+} system, $S = 3/2$, on the magnitude of the magnetic field applied along the x , y and z principal directions of the g and ZFS tensor, which are assumed to be collinear. The example is that of the coordination complex $\text{Co}[(\text{SPPPh}_2)(\text{SP}^i\text{Pr}_2)\text{N}]_2$, see Reference [5] and Chapter 4. To calculate the energies of the magnetic sublevels the spin Hamiltonian was diagonalized numerically using the EPR simulation package EasySpin. [6] Because $\lambda = 1/3$ for this system the sign of D remains indeterminate. It was, however, taken positive to create these level plots. The vertical lines show 9.5 GHz resonances.

already completely lifted. As a result allowed, equidistant transitions are expected, the distance being determined by the principal values D_i , cf. Chapters 2 and 6. Figure 1.2 shows the behavior of the six magnetic sublevels of a high-spin Fe^{3+} system between 0 and 12 T. Transitions of 275.7 GHz (J band) are shown by vertical

1.1. Electron paramagnetic resonance and the study of transition-metal sites

lines: the solid lines represent allowed transitions, which occur only at high fields, the dashed lines represent forbidden transition, which occur at lower fields.

High-spin Fe^{2+} has an integer spin, $S = 2$. The degeneracy of the magnetic sublevels may be completely lifted in zero field and as a result many high-spin Fe^{2+} systems are EPR silent at X band. However, at J band multiple transitions are expected to show up. The energies and composition of the magnetic sublevels can be calculated analytically in zero field, cf. Chapter 5. To calculate the behavior of the sublevels at magnetic fields at which J-band transitions become possible the spin Hamiltonian in Equation 1.1 must be diagonalized numerically.

A hyperfine interaction with a nearby nuclear spin, I , will split the magnetic sublevels according to the possible values of m_I . For instance in the 5 K spectrum in Figure 3.3 in Chapter 3, a splitting of about 4 mT due to the interaction with the cobalt nucleus, $I = 7/2$, is partially resolved. Small splittings may be hard to resolve in an EPR spectrum, but electron nuclear double resonance (ENDOR) can help. As the magnetic field is set to an EPR resonance radio waves are applied. The radio frequency is swept, and if a resonance with the splitting induced by the combined hyperfine *and* nuclear Zeeman interactions is hit the intensity of the observed EPR transition will change. The following nuclear spin Hamiltonian is used to analyze the ENDOR spectra

$$H_n = -\gamma_N \vec{I} \cdot \vec{B} + \langle \vec{S} \rangle \cdot \vec{A} \cdot \vec{I} \quad (1.4)$$

The mixing by the hyperfine interaction of the electron-spin states is assumed to be negligible, which justifies the use of the expectation value of the electron-spin angular momentum, cf. Chapter 4.

Transition-metal sites in proteins and enzymes play an essential role in many biological processes. The relation between the (geometric) structure, electronic structure and function of these active sites is studied in bioinorganic chemistry, and EPR spectroscopy is one of its most important tools.

The starting point is the observation of EPR spectra of these transition-metal sites and the interpretation in terms of their spin-Hamiltonian parameters. In the case of high-spin sites it is advantageous, or required, to record EPR spectra at microwave frequencies higher than the standard 9.5 GHz. Even if the technical challenges of generating microwave radiation at these high frequencies and the required high magnetic fields are overcome, the observation and analysis of these spectra is not straightforward, as will become clear in Chapters 2 and 3.

Once the spin-Hamiltonian parameters, which characterize a transition-metal site, are obtained, one would like to translate them into the molecular wave functions. This step requires advanced quantum-chemical calculations. [8] Significant progress has been made the last decade, particularly using density-functional-theory (DFT). However, the translation of the ZFS term is still problematic.

Progress in the calculation of ZFS parameters requires calibration by experi-

1. Introduction

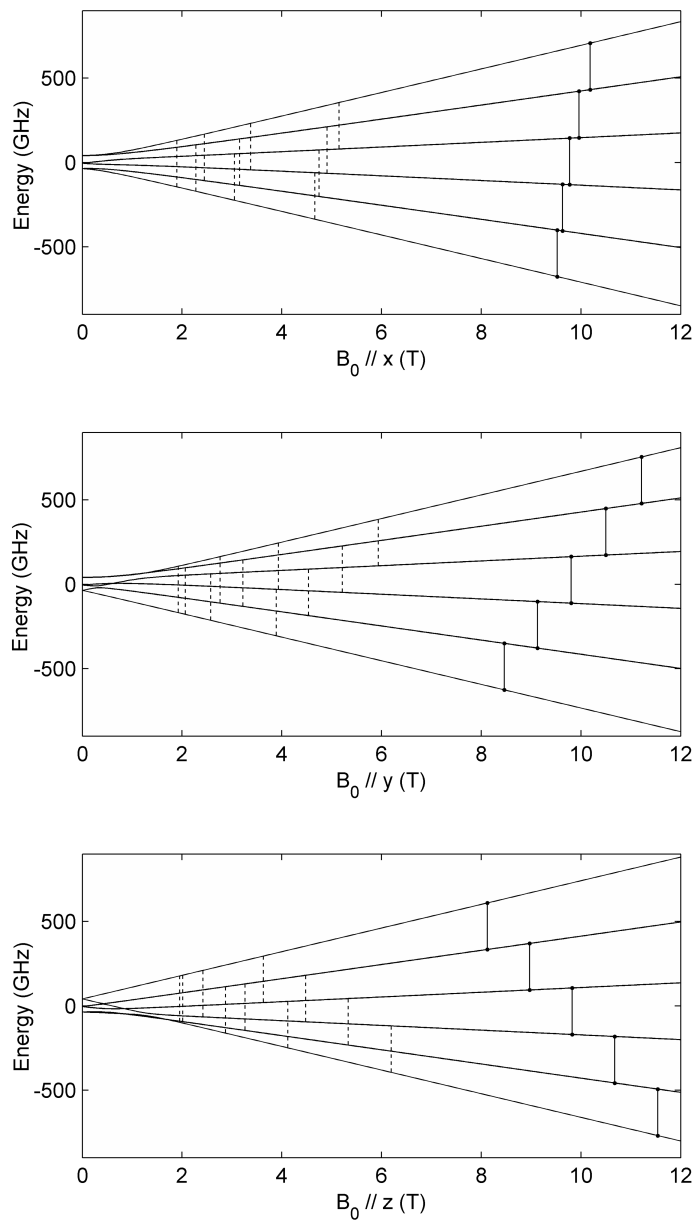


Figure 1.2: The dependence of the energy of the six magnetic sublevels of a high-spin Fe^{3+} system, $S = 5/2$, on the magnitude of the magnetic field applied along the x , y and z principal directions of the g and ZFS tensors, which are assumed to be collinear. [6] The example is that of an iron ion bound to the N-lobe of human serum transferrin, see Chapter 6. The vertical lines show 275.7 GHz resonances. The dashed resonances are “forbidden” transitions.

mentally observed ZFS parameters in different molecular environments. To avoid complications arising in the observation and analysis of EPR spectra of metalloproteins, it is helpful to study biomimetic model complexes, examples of which are reported in Chapters 4 and 5.

1.2 Thesis outline

When the Leiden 275.7 GHz or J-band EPR spectrometer was first taken into operation in 2004 [9] it was equipped with a multi-purpose probe head, suitable for operation in both pulsed and cw mode, and moreover, the cavity had slits to allow optical illumination and ENDOR. The sensitivity and signal stability that could be achieved with this probe head were not sufficient to detect in cw mode the broad resonances of frozen solutions of high-spin metalloproteins. Chapter 2 describes the development of a probe head for the Leiden J-band EPR spectrometer specialized for operation in continuous-wave (cw) mode, which meets these requirements.

To illustrate the possibilities of the J-band spectrometer with the new, cw probe head, spectra are recorded of frozen solutions of the high-spin Fe^{3+} protein rubredoxin [10] from three different organisms: *Desulfovibrio gigas*, found in a small inland sea in the south of France, [11] *Pyrococcus furiosus*, first isolated from geothermally heated marine sediments with temperatures between 90 and 100 °C, [12] and *Megasphaera elsdenii* found in the intestines of cattle. [13] Due to the different environments in which these microorganisms live, the structure of these rubredoxins varies considerably. [14] [15] The structure of the active site, however, hardly differs, and we have found that the same is true for the electronic structure of the sites. The differences in the ZFS parameters are on the order of 1 GHz, which illustrates the close relation between the electronic structure and the function of the active site.

In Chapter 3 the protein desulfiredoxin, which is related to rubredoxin, is studied with cw EPR at multiple frequencies. The active site of this protein is studied both in its natural high-spin Fe^{3+} form and substituted with high-spin Co^{2+} . Remarkable differences in electronic structure between the active sites of desulfiredoxin and rubredoxin are observed, which are related to the differences in structure and undoubtedly to the function of the active sites.

In Chapter 4 of this thesis the full hyperfine tensors of the four phosphorus nuclei, $I = 1/2$, in the high-spin Co^{2+} complex $\text{Co}[(\text{SPPPh}_2)(\text{SP}^i\text{Pr}_2)\text{N}]_2$, previously characterized by multi-frequency EPR, [5] are determined by pulsed ENDOR at 94.9 GHz (W band). These hyperfine tensors are found to depend on whether two phenyl (Ph) or two isopropyl (^iPr) groups are bonded to the phosphorus atom. Thus, the Co–S bonds are non-equivalent as a result of a subtle difference relatively far away from the Co(II)S_4 core.

In Chapter 5 the high-spin Fe^{2+} complex $\text{Fe}[(\text{SPPPh}_2)_2\text{N}]_2$ is studied by cw EPR at 9.5, 94.1 and 275.7 GHz. Powder spectra at W band and J band showed the

1. Introduction

presence of two molecules with a slightly different electronic structure near the iron ion. Spectra recorded at J band on a crystal made it possible to distinguish the signals arising from the two molecules and their spin-Hamiltonian parameters could be determined with high accuracy.

Chapter 6 describes the results of cw EPR at J band on transferrin, a protein that plays an important role in the iron metabolism of all vertebrates. [16] Most transferrins consist of two homologous lobes each containing a deep cleft capable of strong, but reversible binding of a high-spin Fe^{3+} ion. In the research on transferrin EPR has been used, but not nearly to a full extent, because at X band the information that can be obtained on a high-spin Fe^{3+} site is limited. The two lobes are not distinguished and, moreover, the characteristic X-band spectrum of transferrin is not quantitatively understood. At J band the two lobes are distinguished in the spectrum of human serum transferrin and the spectrum is satisfactorily reproduced by simulation. The observation of the signals due to the two lobes is supported by spectra recorded on two monoferric forms of human serum transferrin in which either of the binding sites is disabled by a local mutation.

The final chapter of this thesis does not deal with EPR on transition-metal sites. Instead resonance Raman spectroscopy is employed to observe the vibrational modes of spheroidene in the photosynthetic reaction center (RC) of *Rhodobacter sphaeroides*. This carotenoid is believed to have a photoprotective function, although the exact mechanism is not understood. In literature no consensus existed on the configuration of the spheroidene molecule in the RC. Using as a calibration resonance Raman spectra obtained on isotope labeled spheroidene, reconstituted into the RCs of the carotenoidless mutant of *Rb. sphaeroides* R26, a method to calculate the resonance Raman spectra of spheroidene in a particular conformation has been developed in the last decade. [17, 18] In Chapter 7 resonance Raman spectra detected at different excitation wavelengths of wild-type RCs are compared to those of reconstituted R26 RCs. Combining these spectra with the calculations allowed us to establish the configuration of spheroidene in the RC of wild-type *Rb. sphaeroides* to be 15,15'-*cis*. However, in the reconstituted R26 RCs spheroidene occurs in two configurations, namely 15,15'-*cis* and 13,14-*cis*.

Chapter 2

Continuous-wave EPR at 275 GHz: Application to high-spin Fe^{3+} systems

The 275 GHz electron-paramagnetic-resonance spectrometer we reported on in 2004 has been equipped with a new probe head, which contains a cavity especially designed for operation in continuous-wave mode. The sensitivity and signal stability achieved with this new probe head is illustrated with 275 GHz continuous-wave spectra of a 1 mM frozen solution of the complex Fe(III)-ethylenediamine tetra-acetic acid (EDTA) and of 10 mM frozen solutions of the protein rubredoxin, which contains Fe^{3+} in its active site, from three different organisms. The high quality of the spectra of the rubredoxins allows the determination of the zero-field splitting parameters with an accuracy of 0.5 GHz. The success of our approach results partially from the enhanced absolute sensitivity, which can be reached using a single-mode cavity. At least as important is the signal stability that we were able to achieve with the new probe head.

G. Mathies, H. Blok, J.A.J.M. Disselhorst, P. Gast, H. van der Meer, D.M. Miedema, R.M. Almeida, J.J.G. Moura, W.R. Hagen and E.J.J. Groenen, *J. Magn. Res.*, 210 (2011) 126-132.

2.1 Introduction

The understanding of complex electron-paramagnetic resonance (EPR) spectra of the active sites of metalloproteins is often greatly advanced by studies at more than one microwave frequency. High-frequency/high-field (HF) EPR is particularly useful for systems that have a large zero-field splitting. Integer spin systems tend to be EPR silent at conventional microwave frequencies and for half-integer spin systems the ease and precision by which the zero-field splitting parameters can be determined is enhanced. The goal of this work is to extend the possibilities of HF EPR for metalloproteins.

The HF EPR spectra of metalloproteins with a zero-field splitting on the order of the microwave quantum are difficult to record. These spectra cover large field ranges. Due to conformational strain the resonances in the HF EPR spectra are broad, and line widths of 1 T are no exception. Moreover, the available amount of protein is often limited and the same holds for the concentration. Relaxation times can be very short, which makes only continuous-wave (cw) EPR feasible. In order to achieve our goal, we need a HF cw EPR spectrometer with high sensitivity and signal stability, which is maintained while using a large modulation amplitude.

High-frequency/high-field EPR was introduced by the group of Lebedev in Moscow. [19–21] Their spectrometer operated at a frequency of 140 GHz, which is the highest frequency at which conventional waveguides can be used. Indeed, HF EPR comes with technical difficulties. Major progress was made by the introduction of quasi-optical techniques and in the development of high-frequency microwave components and high-field magnets. Spectrometers that operate in cw mode at frequencies above 140 GHz are found in specialized research groups at Cornell (250 GHz [22] and 100-300 GHz [23]), in Grenoble (160 - 525 GHz [24–26]), St. Andrews (80 - 200 GHz [27]), Berlin (360 GHz [28]), Tallahassee (24 GHz - 3 THz [29, 30]), Frankfurt (180 GHz [31]), Leiden (275 GHz [9, 32]) and Mülheim an der Ruhr (244 GHz [33]). This year Bruker has released a spectrometer that operates at 263 GHz.¹ For recent reviews see references 34 and 35.

In 2004 we reported on the construction of a cw and pulsed EPR spectrometer operating at 275 GHz. [9] This spectrometer is equipped with a multi-functional TE₀₁₁ cylindrical cavity, which has slits to allow optical access and ENDOR. [32] With this cavity it is possible to measure cw EPR of paramagnetic species that have narrow resonances (for instance spin-labels), but spectra of species that show broad resonances are poor. Our approach to improve the quality of these spectra is to equip the spectrometer with a second probe head, which contains a single-mode cavity optimized for operation in cw mode.

Currently all other HF cw EPR spectrometers operate in non-resonant transmission or reflection or use a Fabry-Perot interferometer. However the use of a

¹<http://www.bruker-biospin.com/e780.html>

single-mode cavity has several advantages. First, one can profit from the increase of the absolute sensitivity with an increasing microwave frequency, which theory predicts. [36–39] Secondly, the high B_1 field at the sample, which can be generated with a single-mode cavity, is advantageous for fast-relaxing species. Finally, the small sample volume makes it relatively easy to achieve a high, homogeneous modulation field throughout the sample. Drawbacks of using a single-mode cavity could be sample handling and the problem of constructing a single-mode cavity of the dimensions that fit 275 GHz, but the former is not a problem for solutions of proteins due to the capillary force and we already showed that we could overcome the latter.

An ever persisting problem in cw HF EPR is signal stability. The high magnetic field induces strong Lorentz forces on the modulation coil, which cause vibrations in the probe head at the modulation frequency or its harmonics. This is called microphonics. [27, 40, 41] This interference tends to be in phase with the modulated EPR signal and can seriously deteriorate the signal-to-noise ratio. This is particularly a problem when recording broad resonances with a large modulation amplitude. Operation in induction mode can reduce the effect of microphonics on the EPR signal [27, 42], but this is not an option when a single-mode cavity is used. We show that the use of a single-mode cavity also allows the reduction of the influence of microphonics such that high-quality spectra of frozen solutions of low concentrations of metalloproteins can be recorded.

The achieved sensitivity and stability is illustrated by 275 GHz cw EPR spectra of a 1 mM frozen solution of the complex Fe(III)-ethylenediamine tetra-acetic acid (EDTA) and of 10 mM frozen solutions of the protein rubredoxin, which contains Fe^{3+} in its active site. The iron ion is in a high-spin state, which leaves five unpaired electrons ($S = 5/2$). We have chosen Fe(III)-EDTA as a model complex to demonstrate the performance of our spectrometer, because of its representative spectrum and because several HF EPR studies have been performed on frozen solutions of Fe(III)-EDTA on other spectrometers. [33, 43–45] Rubredoxins are small proteins (typically 50–54 amino acids) that are found in sulfur-metabolizing bacteria and archaea, in which they participate in single-electron transfer. They have been studied extensively. [10] The iron ion in the active site is approximately tetrahedrally coordinated to the sulfur atoms of four cysteine residues occurring in a Cys-x-x-Cys-Gly and a Cys-Pro-x-Cys-Gly segment. Our studies show that we are able to acquire high-quality HF cw EPR spectra of small amounts of dilute frozen solutions of high-spin Fe^{3+} systems.

2.2 Experimental

2.2.1 The cw probe head

The cw probe head is similar to the probe head that contained the general purpose cavity. [9] This probe head can be placed into a helium flow cryostat located in the room-temperature bore of the superconducting magnet. The microwaves are guided through an oversized corrugated waveguide, which ends in a corrugated tapered transition to a fundamental-mode rectangular waveguide from where the microwaves couple into the cavity.

Figure 2.1 shows a drawing of the cavity. The design considerations for the cw cavity were to have a high quality factor and to minimize microwave leakage, since this could destabilize the EPR signal. The cavity is a 14 mm long cylinder with a diameter of 1.40 mm in a massive bronze block, which was made by electrical discharge machining. It was polished with diamond paste and gold plated. At both open ends of the cylinder a bronze plunger enters, which has a choke joint at the front. We tune the cavity to the microwave frequency of 275.7 GHz by moving the plungers in or out of the cylinder using a set of gears. The length of the cavity can be varied in this way between 0.80 and 1.40 mm with a position accuracy of 1 μm . A quartz sample tube with outer diameter 0.25 mm can be inserted into the cavity through the plungers. With an inner diameter of 0.15 mm the sample volume inside the cavity is 25 nl. The coupling between the fundamental-mode rectangular waveguide and the cavity is varied by rotating the cavity-plunger-gear combination around a vertical axis through the rectangular waveguide and the coupling hole.

Also shown in Figure 2.1 is the modulation coil. The modulation coil consists of 80 turns of 0.2 mm diameter copper wire, which are encased in Stycast epoxy. The coil is placed on a solid rexolite mount, which is fixed on a pertinax plate, which is attached to the end of the probe head. The distance between the coil and the cavity block is 0.5 mm, and the two are mechanically isolated. The modulation coil leads are fixed to the mount with Stycast and go up to the top of the probe head as a twisted pair. The resistance of the modulation coil at room temperature is about 1 Ω . The modulation amplitude is 7 mT/A peak-peak.¹

2.2.2 Samples

Fe(III)-EDTA sodium salt (Sigma-Aldrich Chemie GmbH) was dissolved in an aqueous solution which was kept at pH 5 by a citric acid buffer. Samples consisted of one part of this solution and one part glycerol. Rubredoxin from *Desulfovibrio gigas* [14, 46] was purified according to a previously reported method. [47] To ensure that no other metal forms of rubredoxin, other than iron, were present in the sample, the

¹After submission of this work the design of the mount of the modulation coil was altered to improve the endurance against repeated cooling cycles. See Appendix B.

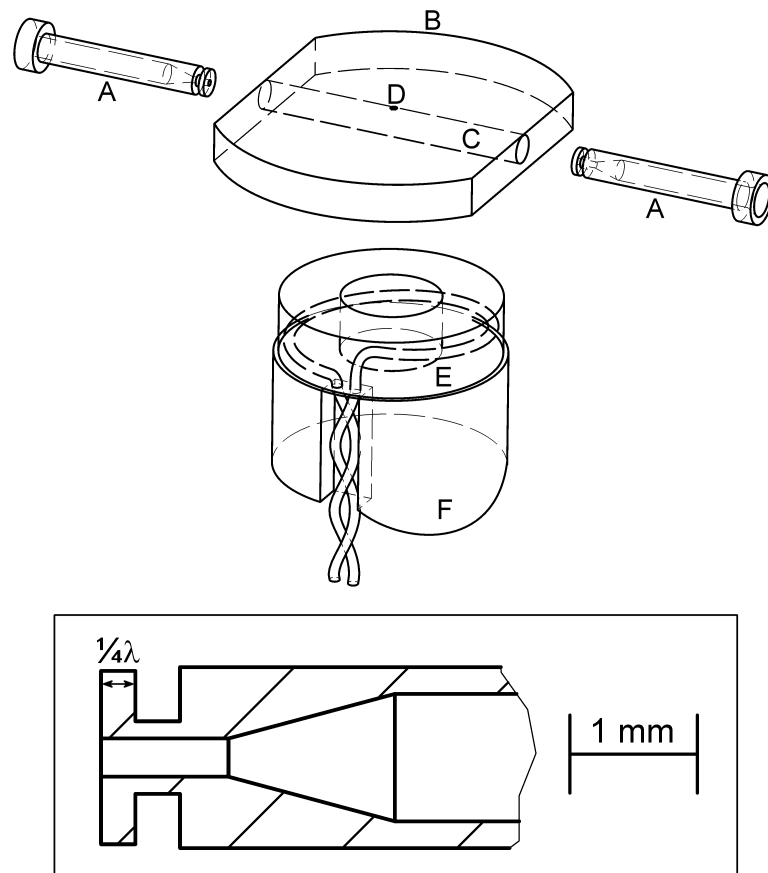


Figure 2.1: Schematic drawing of the 275 GHz cw cavity and the modulation coil. A: plungers, B: cavity block, C: cavity, D: coupling hole, E: modulation coil encased in Styrcast (for clarity only one turn is depicted) F: modulation coil mount. The inset shows the choke joint at the end of the plungers in detail.

2. Continuous-wave EPR at 275 GHz: Application to high-spin Fe³⁺ systems

protein was injected in a 6 ml Resource Q column (GE Biosciences) equilibrated with 10 mM Tris-HCl pH 7.6 buffer and eluted in a linear NaCl gradient (0 - 500 mM in buffer). Throughout the purification procedure the purity of the rubredoxin fractions was assessed by SDS-PAGE, and by measuring the A_{280}/A_{493} ratio, which for pure Fe-rubredoxin is 2.4. Rubredoxin from *Pyrococcus furiosus* [15, 48] and *Megasphaera elsdenii* were prepared as described in reference [49] and [50] respectively.

2.3 Results

2.3.1 Absolute sensitivity

In Figure 2.2 the room temperature 275 GHz cw EPR spectrum of a 10^{-4} M solution of the spin label TEMPO (Sigma-Aldrich Chemie GmbH) in toluene is shown. This spectrum was recorded using a modulation amplitude of 0.05 mT, a time constant of 100 ms and a microwave power of $50 \mu\text{W}$.¹ The three lines originate from the hyperfine interaction with the ¹⁴N nuclear spin ($I = 1$). We determine the absolute sensitivity of our spectrometer from this spectrum. Assuming that the volume of the sample that contributes to the EPR signal is one-third of the sample volume inside the cavity, the spectrum originates from 10^{12} spins. The signal-to-noise ratio of the spectrum shown in Figure 2.2 is 320. The total line width of the spectrum is $3 \times 0.35 \text{ mT} = 1.05 \text{ mT}$. This gives an absolute sensitivity of $8 \cdot 10^8 \text{ spins/mT}/\sqrt{\text{Hz}}$.

2.3.2 Operating the spectrometer in cw mode

Microphonics are observed as an unstable component at the modulation frequency in the frequency spectrum of the output voltage of the detection diode. This component, which is not related to absorption of microwaves by the paramagnetic sample, becomes stronger as the magnetic field strength is increased. Tuning the cavity by moving the plungers with care brings down this modulation frequency pick-up. If the cavity is properly tuned the reflection of the microwaves by the cavity is at a minimum, which means that a small detuning of the cavity will hardly affect the reflection. It is thus necessary to tune at a high magnetic field strength where no EPR signal is observed.

The high-spin Fe³⁺ spectra are recorded with a scan rate of 2 mT/s and acquiring these spectra takes hours. The microwave frequency of the current bridge of our spectrometer is fixed. This means that we have to take care to keep conditions inside the cryostat constant. Small variations in temperature and helium pressure inside

¹The power output of the microwave bridge is 1 mW, but the maximum power that can be used in cw experiments at room temperature is about $50 \mu\text{W}$. Coupling of the microwaves into the cavity is not fully critical and at higher output powers reflected microwaves cause saturation in the detection path.

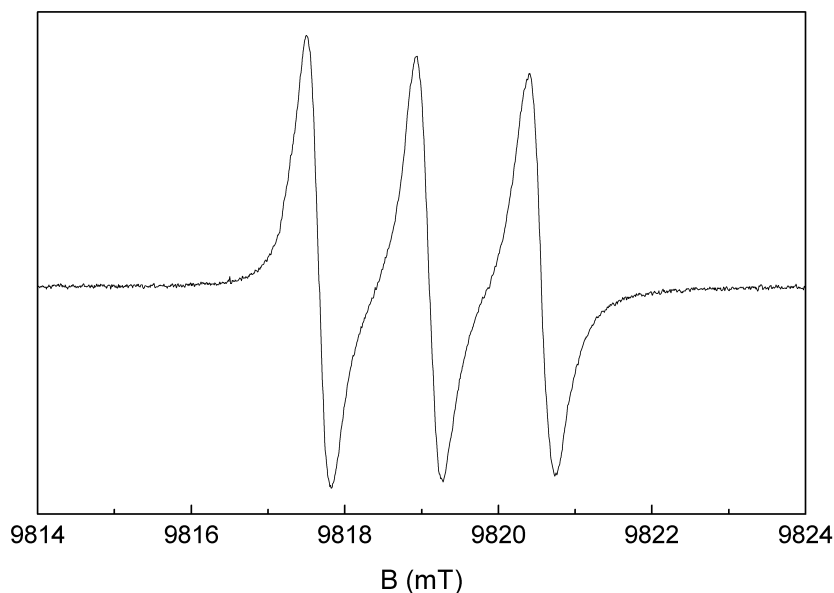


Figure 2.2: The room temperature cw EPR spectrum at 275 GHz of a 10^{-4} M solution of the spin label TEMPO in toluene. Experimental conditions: modulation amplitude: 0.05 mT, time constant: 100 ms, microwave power: $50 \mu\text{W}$.

the flow cryostat may detune the cavity, which leads to drift of the baseline of the EPR spectrum and increases the effect that microphonics have on the EPR signal. The use of a high modulation amplitude is essential to detect the broad resonances of Fe^{3+} . This makes minimization of microphonics even more challenging. In practice a modulation current of about 600 mA was found to be optimal. No dependence of the microphonics on the modulation frequency was found. The modulation frequency was chosen between 1 and 2 kHz.

A decrease of the sample temperature does not automatically mean an increase of the sensitivity of the spectrometer. When the probe head is cooled by cold helium gas, the circumstances in the cavity, which have a strong influence on the reflected microwaves, tend to vary more strongly. This has a negative effect on the signal stability. Also the quality factor of the cavity increases strongly as it is cooled down, due to an increase in the conductivity of the gold-plated walls of the cavity. An increased quality factor means an increase in the effect on the EPR signal of a slight detuning of the cavity which means that microphonics become more of a problem. In order to compensate for this effect we had to attenuate the microwave power in order to record the Fe^{3+} spectra.

2. Continuous-wave EPR at 275 GHz: Application to high-spin Fe³⁺ systems

2.3.3 High-spin Fe³⁺ spectra

In Figure 2.3 the cw EPR spectra recorded at 275 GHz of a 1 mM frozen solution of Fe(III)-EDTA are shown. The recorded spectra cover 6 T. Around 6.6 T a resonance with a width of 0.5 T is observed. As the temperature is increased, this resonance decreases in intensity, while the resonances in the $g = 2$ region gain intensity ($g = 2$ corresponds to a magnetic field of 9.85 T for 275.7 GHz). In Figure 2.4 the $g = 2$ region is shown in detail. The signal-to-noise ratio for the resonance around 9.8 T (peak to peak) at 15 K is 130. Another resonance is observed around 8.2 T, which is equidistant with the resonances around 6.6 T and 9.8 T. Two more resonances are observed around 10.2 T and 11.3 T. Note that the resonances are broadest at the extremes of the spectrum. Resonances that do not originate from Fe(III)-EDTA are present in the spectra. At temperatures above 5 K in the $g = 2$ region six lines due to a manganese impurity could be properly recorded by scanning slowly with a lower modulation amplitude. The resonance at 7.6 T is due to a contamination of the frozen sample solution with molecular oxygen. [51] The origin of the resonance that is observed at 9.6 T in the 5 K spectrum is not known.

Figure 2.5 shows cw EPR spectra recorded at 275 GHz of a frozen solution of the protein rubredoxin from *D. gigas*. The recorded spectra cover 12 T and resonances of a width of 1 T are observed. The resonances observed at low field (up to 4 T) lose intensity with temperature. Broad resonances around 6.8 T, 8.7 T, 10.2 T and 11.3 T increase in intensity upon an increase in temperature from 5 to 10 K. In the $g = 2$ region resonances at 9.5 T and 9.7 T appear at higher temperature. The signal-to-noise ratio for the resonance at 9.7 T (peak to peak) at 25 K is 200. At 4.4 T and 7.6 T resonances due to molecular oxygen are seen. [51] As in the Fe(III)-EDTA spectra, a resonance of unknown origin is observed at 9.6 T in the 5 K spectrum. The narrow resonance at 9.8 T ($g \approx 2$) that is visible at 10 and 25 K is due to an impurity.

In Figure 2.6 cw EPR spectra recorded at 275 GHz of rubredoxin from three different species are compared. The spectra are similar, but the precise position of the resonances around 6.8 T, 8.7 T, 10.2 T and 11.3 T varies for the different species by a few tens of mT. Also the shape of the spectra of rubredoxin from *P. furiosus* and in particular from *M. elsdenii* differs from that of the spectrum from *D. gigas*. For these two species of rubredoxin a broad background signal seems to be present. A manganese resonance is observed in the spectrum of rubredoxin from *P. furiosus*.

2.4 Analysis

The following spin Hamiltonian was used to analyze the spectra of high-spin Fe³⁺ ($S = 5/2$).

$$H = \mu_B \vec{B} \cdot \vec{g} \cdot \vec{S} + \vec{S} \cdot \vec{D} \cdot \vec{S} \quad (2.1)$$

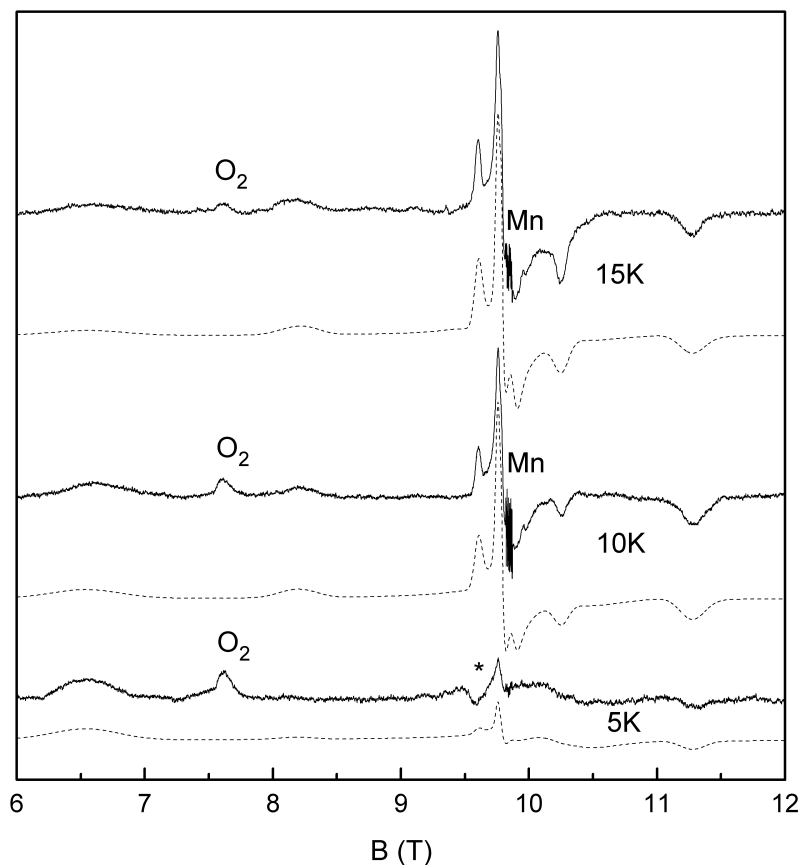


Figure 2.3: The 275 GHz cw EPR spectra of a 1 mM frozen solution of the model complex Fe(III)-EDTA at three temperatures. Experimental conditions: modulation amplitude: 3 mT, time constant: 1 s, scan rate: 2 mT/s, microwave power: 1 μ W. Spectra were recorded at least twice to ensure reproducibility of all features. The solid lines are the experimentally observed spectra and the dashed lines are the spectra calculated by EasySpin with the parameters given in Table 2.1. The origin of the resonance marked with a \star in the 5 K spectrum is unknown. In the 10 K spectrum a weak EPR signal between 8.5 and 9.5 T that does not originate from the Fe(III)-EDTA was subtracted for clarity.

The first term is the electron Zeeman term. A first-order contribution from spin-orbit coupling induces g -anisotropy, but this effect is expected to be small, since high-spin Fe^{3+} has a ${}^6S_{5/2}$ ground state. The second term is a field independent fine-structure term (the zero-field splitting, ZFS). The tensor \vec{D} mainly consists of a second-order contribution from spin-orbit coupling. It is symmetric and taken traceless, and it

2. Continuous-wave EPR at 275 GHz: Application to high-spin Fe³⁺ systems

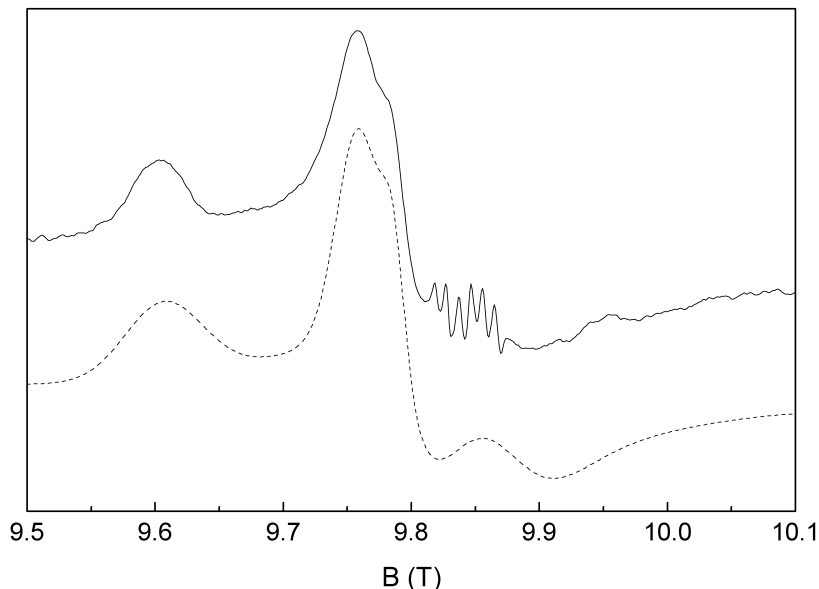


Figure 2.4: Detail of the 275 GHz cw EPR spectrum of a 1 mM frozen solution of the model complex Fe(III)-EDTA at 15 K in Figure 2.3. The solid line is the experimentally observed spectrum and the dashed line is the spectrum calculated by EasySpin with the parameters given in Table 2.1.

can be characterized by two parameters, D and E .

$$D = 3/2D_z, E = 1/2(D_x - D_y) \quad (2.2)$$

The rhombicity of \vec{D} is given by the ratio $\lambda = E/D$. The principal axes are chosen such that $|D_z| > |D_y| > |D_x|$ and thus $0 < \lambda < 1/3$.

In the weak-field limit ($\vec{S} \cdot \vec{D} \cdot \vec{S} \gg \mu_B \vec{B} \cdot \vec{g} \cdot \vec{S}$) the effective $S = 1/2$ picture, in which the effect of the zero-field splitting can be incorporated in an effective g -tensor, is applicable. This is the case when rubredoxin is studied at X-band. The absolute value and sign of D can be determined only indirectly from the temperature dependence of the spectra and the effective g -values at which resonances are observed. [52]

In the high-field limit ($\vec{S} \cdot \vec{D} \cdot \vec{S} \ll \mu_B \vec{B} \cdot \vec{g} \cdot \vec{S}$) the frozen solution spectrum shows the transitions associated with the principal axes of the g -tensor, because the energy levels vary linearly with the field strength. At low temperature the large polarization effect greatly simplifies the spectra and the sign of D can be determined from the spectra directly.[45] Transitions arising from one principal direction are separated in

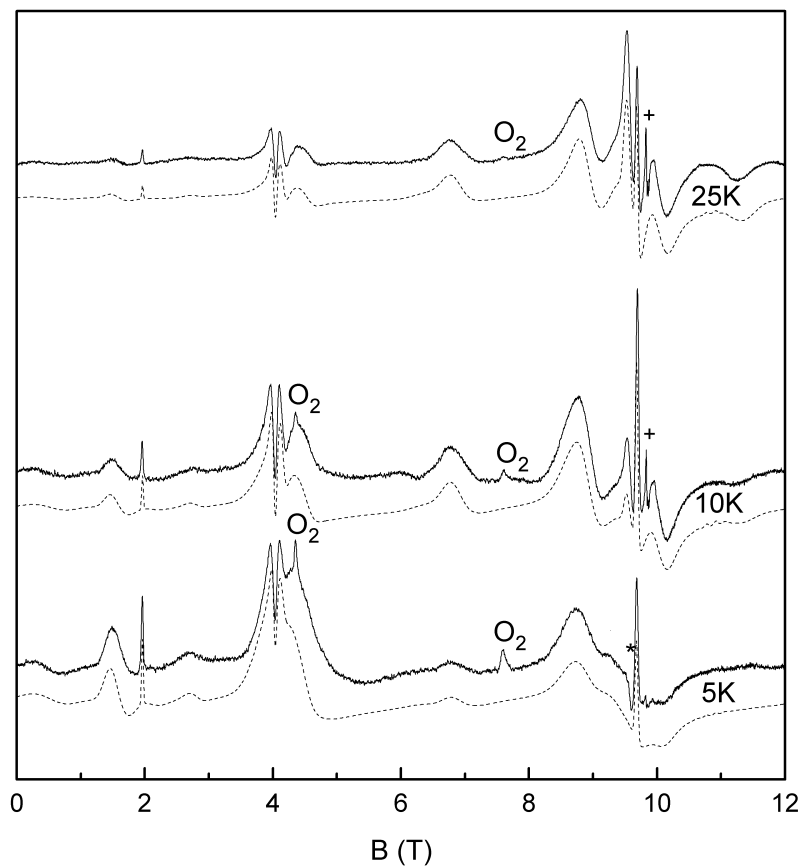


Figure 2.5: The 275 GHz cw EPR spectra of a 10 mM frozen solution of the protein rubredoxin from *D. gigas* at three temperatures. Experimental conditions: modulation amplitude: 4 mT, time constant: 1 s, scan rate: 2 mT/s, microwave power: 1 μ W. The solid lines are the experimentally observed spectra and the dashed lines are the spectra calculated by EasySpin with the parameters given in Table 2.1. The origin of the resonance marked with a \star in the 5 K spectrum is unknown. The resonance marked with a $+$ in the 10 K spectrum derives from an impurity.

field by:

$$\Delta B = \frac{3D_i}{\mu_B g_i} \quad (2.3)$$

where i is x , y or z . The case of Fe(III)-EDTA at 275 GHz is near the high-field limit. Resonances are observed at 6.6 T, 8.2 T and 9.85 T. These resonances are roughly 1.6 T apart, which gives an absolute value of about 15 GHz for the largest principal value of \vec{D} , D_z . Since these resonances are observed below $g = 2$, the sign of D_z is negative. A resonance is observed at 11.3 T, which is 1.45 T above 9.85 T. From

2. Continuous-wave EPR at 275 GHz: Application to high-spin Fe³⁺ systems

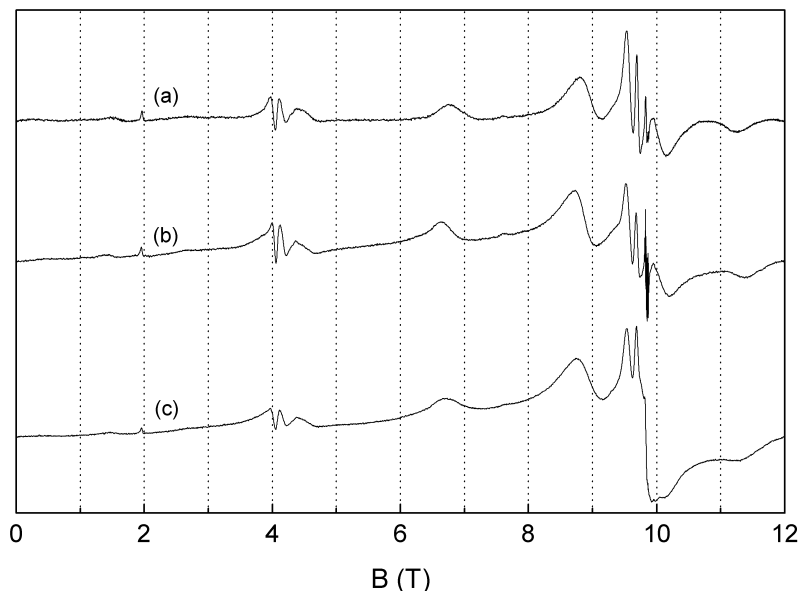


Figure 2.6: The cw EPR spectra of 10 mM frozen solutions of rubredoxin from three different organisms at 25 K: (a) *D. gigas*, (b) *P. furiosus*, and (c) *M. elsdenii*. The vertical dashed lines are displayed to guide the eye to the differences between the three spectra. Simulations of the spectra of rubredoxin from *P. furiosus* and *M. elsdenii* are presented in Appendix A.

this we estimate $D_y \approx 14$ GHz, which gives $D \approx -22.5$ GHz and $E \approx -6.5$ GHz.

In the intermediate region the ZFS-term and the Zeeman term are similar in size. This is the situation of rubredoxin at 275 GHz. As can be seen in Figure 2.5 this gives rise to complex spectra. The way to extract the spin Hamiltonian parameters from the observed spectra is by comparison with spectra that were calculated by numerical diagonalization of the spin Hamiltonian. For this we used EasySpin. [6] We assume that the D - and g -tensor are collinear.

The spin Hamiltonian parameters that were found to fit the experimental spectra of the different types of rubredoxin best are shown in Table 2.1. The resonances below 4 T are due to forbidden transitions. The shape of the resonance around 4 T strongly depends on λ . The positions of the 6.8 T, 10.1 T and 11.3 T resonances are determined by the values of E and D . The position of the resonance at 8.7 T is influenced by both D and g_x . The values of g_y and g_z are determined by the positions of the 9.5 T and 9.7 T resonances respectively.

Also the Fe(III)-EDTA spectra were compared with spectra calculated with EasySpin and the parameters with which these spectra were best reproduced are summarized in Table 2.1. The value of D_z is determined by the position of the resonance around 6.6 T. The value of g_z must be slightly higher than g_x and g_y to

reproduce the shape of the spectrum just below 9.8 T.

	D (GHz)	E (GHz)	λ	g_x	g_y	g_z	D -strain (GHz)	E -strain (GHz)
Fe(III)-EDTA	-23.3	-6.3	0.27	2.004	2.004	2.005	4.3	1.7
<i>D. gigas</i> Rd	47.5	12.5	0.26	2.02	2.021	2.014	9.0	2.5
<i>P. furiosus</i> Rd	49.5	13.0	0.26	2.02	2.021	2.014	9.0	2.5
<i>M. elsdenii</i> Rd	48.5	13.0	0.27	2.02	2.021	2.014	9.0	2.5

Table 2.1: Spin Hamiltonian parameters that best reproduce the experimental spectra. The strains are quantified by the FWHM of the Gaussian distribution in the D - and E -values. Errors are estimated from the sensitivity of the calculated spectrum to a variation in a parameter: ± 0.5 GHz for the zero-field splitting parameters, ± 0.001 for the g -values and ± 0.5 GHz for the strains. The spectra of rubredoxin are relatively insensitive to a change in g_x . The error in this parameter is estimated to be ± 0.005 . The error in the measured magnetic field values was estimated to be 2 mT at 10 T and gives a negligible contribution.

The resonances of the Fe(III)-EDTA are broader when they are further away from $g = 2$. Transitions between energy levels that have the larger $|m|$ are broader, which points to the presence of D - and E -strain. In fact the shape of the observed spectra of both Fe(III)-EDTA and rubredoxin could only be reproduced by taking into account D - and E -strain in the EasySpin calculations (see Table 2.1).¹ No additional isotropic line-broadening was taken into account.

2.5 Discussion

The modifications to our spectrometer have made it possible to acquire high-quality cw EPR spectra at 275 GHz on 25 nl of a 1 mM frozen solution of the high-spin Fe³⁺ model complex Fe(III)-EDTA. We have also acquired high-quality spectra of 10 mM frozen solutions of the high-spin Fe³⁺ protein rubredoxin. The signal-to-noise ratio of these spectra is such that a lower protein concentration could have been used. The sensitivity and baseline stability of our spectrometer are high enough to resolve resonances that have a width of 1 T in spectra that are acquired at low temperature, range over 12 T and require several hours to record. The quality of the spectra allows accurate determination of the parameters of the spin Hamiltonian by comparison to

¹In the online documentation on EasySpin the author notes that the effect of strains on the spectra are calculated using an approximation, which is only applicable as long as the strain distribution width is much smaller than the parameter itself. In our situation this is not immediately clear. However spectra that were calculated by running a loop over a distribution of spin Hamiltonian parameters matched almost exactly with the spectra that were calculated in the (much less time consuming) EasySpin approximation. The approximation is thus valid.

2. Continuous-wave EPR at 275 GHz: Application to high-spin Fe³⁺ systems

spectra that were calculated from numerical diagonalization of the spin Hamiltonian while taking into account line broadening due to D - and E -strain.

The sensitivity that can be obtained with a particular spectrometer for a particular system in practice depends on the width of the resonance that has to be recorded, the modulation amplitude that can be generated and the microwave power that can be applied. The spectrum shown in Figure 2.2 from which we determined the absolute sensitivity of our spectrometer to be $8 \cdot 10^8$ spins/mT/ \sqrt{Hz} was acquired at maximum power and with a modulation amplitude that was optimal with respect to the line width.

The absence of slits and the complete closure of the cw cavity for microwaves by means of the choke joints assures that the quality factor of the cw cavity is higher than that of the general purpose cavity. [9] To estimate this increase we have determined the length of a $\pi/2$ -pulse for a single crystal of gamma-ray irradiated lithium fluoride ($S = 1/2$). At room temperature this is 160 ns for the cw cavity and approximately 340 ns for the general purpose cavity. This corresponds to a twofold increase in the B_1 -field in the cavity and in the signal amplitude. Continuous-wave spectra recorded on TEMPO in toluene show that the absolute sensitivity at room temperature is approximately five times higher for the cw cavity. The additional increase is mainly due to improved coupling of the microwaves into the cavity.

The absolute sensitivity of our spectrometer is on the high end of the range of sensitivities achieved with other HF EPR spectrometers. [22–31, 33] In order to study high-spin metalloproteins by cw HF EPR, high sensitivity is a primary condition that must be fulfilled. Signal stability is as important, particularly for metalloproteins that show a large zero-field splitting. Hence, during low temperature experiments temperature and pressure in the cryostat must be controlled precisely. And microphonics must be minimized. The construction of a cavity that is completely closed for microwaves and the specific construction of the modulation coil have been instrumental in accomplishing this.

The quality of the spectra that we recorded on a 25 nl sample of 1 mM Fe(III)-EDTA is comparable to the quality accomplished by other authors at 285 and 244 GHz at concentrations that were higher by a factor of 60 or more. [33, 43, 44] The quality of the spectra acquired at 230 GHz as reported in [45] at 10 mM is slightly better than ours.

The chemistry of Fe(III)-EDTA in solution is very complex, which makes it difficult to compare spin Hamiltonian parameters found in various experiments. The coordination of the iron ion in EDTA is pH dependent as is its EPR spectrum. [53, 54] A study of Fe(III)-EDTA in the form of a crystalline powder of Co(III)-EDTA with impurities of ferric ions, ratio Co:Fe = 50:1, at X-band and Q-band gave $|D| = 24.9$ GHz and $E/D = 0.31$. [55] The X-band spectrum from this study is reproduced with the parameters that were found from our experiments, except for the D - and E -strain which must be set to zero and instead an isotropic line broadening of 3 mT must be introduced. Our spin Hamiltonian parameters resemble closely

the values reported in reference [45]. In this study no D - and E -strain were taken into account.

Rubredoxin from several organisms has been studied at the standard EPR frequency of 9 GHz. [10, 52, 56–58] The D -values are around 50 GHz and the rhombicity parameter λ is around 0.26. This is in line with our results. The natural variety in the amino-acid sequences of rubredoxins from different organisms results in small variations in the geometrical structure of the active site of the protein. [14, 15] This will lead to subtle variations in the electronic structure of the active site, which can very well be studied by HF EPR. [59] Figure 2.6 shows that at 275 GHz a change of 1 GHz in one of the zero-field-splitting parameters is obvious from the spectra. The quality of our spectra is such that we are able to determine the zero-field-splitting parameters with an accuracy of 0.5 GHz by comparison to spectra calculated from numerical diagonalization of a spin Hamiltonian.

The D - and E -strain that had to be included in the simulations to reproduce the experimental spectra is comparable in size for the model complex and the protein. A considerable active-site heterogeneity is common for proteins, but not for Fe(III)-EDTA. Heterogeneity in the coordination of the iron ion could be an explanation. [60]

Börger *et al.* interpreted the complicated frozen solution spectrum of rubredoxin at X-band by including E/D -strain into their simulations. [58] From X-band spectra the strain in D and E can not be determined independently. They found a Gaussian distribution of E/D with a width of $\sigma_{E/D} = 0.03$. If we take the square root of the sum of the squares of our relative D - and E -strain, we find a relative E/D -strain of 11%. On average the value of E/D found for rubredoxin is 0.26, which gives a value of 0.03 for $\sigma_{E/D}$.

The precise positions of the resonances around $g = 2$ made it necessary for both Fe(III)-EDTA and rubredoxin to include a small g -anisotropy in the simulations. The high magnetic field at which the spectra were recorded made it possible to determine reliable g -values directly. These g -values are clearly different from the g -values that were determined earlier, indirectly, from X-band spectra. [58]

2.6 Conclusion

Our studies of high-spin Fe^{3+} systems show that we are able to acquire high-quality HF cw EPR spectra of frozen solutions of small amounts of modest size metallo-proteins. The quality of the spectra is high enough to observe g -anisotropy and to determine the zero-field-splitting parameters with an accuracy of 0.5 GHz.

The success of our approach results partially from the enhanced absolute sensitivity that can be reached using a single-mode cavity, which was specifically constructed to be used for cw HF EPR. At least as important is the achieved signal stability.

2. Continuous-wave EPR at 275 GHz: Application to high-spin Fe³⁺ systems

Chapter 3

Multi-frequency EPR study of Fe^{3+} and Co^{2+} in the active site of desulforedoxin

The continuous-wave 275.7 GHz EPR spectra of a frozen solution of desulforedoxin provide the zero-field splitting (ZFS) parameters of the high-spin Fe^{3+} active site: $D = 72 \pm 1$ GHz and $\lambda = 0.074 \pm 0.002$. The X-band spectra of a frozen solution of Co(II)-substituted desulforedoxin at multiple temperatures allow an estimate of the ZFS parameters: $D < -300$ GHz and $\lambda = 0.26$. The typical variation in the geometry of the active site of a protein or enzyme, usually referred to as conformational strain, does not only make the detection of EPR spectra challenging, but also their analysis. The remarkable differences between the ZFS parameters of the high-spin Fe^{3+} site of desulforedoxin, the high-spin Fe^{3+} site of rubredoxin and the high-spin Co^{2+} substituted site of desulforedoxin are discussed.

Guinevere Mathies, Rui M. Almeida, Peter Gast, José J. G. Moura and Edgar J. J. Groenen, *in preparation*.

3. Multi-frequency EPR study of Fe^{3+} and Co^{2+} in the active site of desulforedoxin

3.1 Introduction

In many proteins and enzymes the active site contains a paramagnetic transition-metal ion and electron-paramagnetic-resonance (EPR) spectroscopy can provide detailed information on its electronic structure. This makes EPR spectroscopy an invaluable tool in the study of the relationship between structure and function of the active sites in biological molecules. [61–63] Whenever the transition-metal ions carry a spin angular momentum $S > 1/2$ the degeneracy of the magnetic sublevels may already (partly) be lifted in the absence of an external magnetic field. For such systems it is advantageous, or even required, to record EPR spectra at a microwave frequency comparable to or larger than this zero-field splitting (ZFS), and one needs an EPR spectrometer operating at a frequency higher than the standard 9.5 GHz (X band). Fortunately, the last decades have shown a strong increase in the possibilities to perform EPR spectroscopy at higher frequencies.

An EPR spectrum is to be analyzed in terms of its spin-Hamiltonian parameters, which then have to be translated into electronic structure using advanced quantum-chemical methods. Considerable progress has been made with such calculations in recent years, in particular based on density-functional theory, but calculation of the ZFS for transition-metal ions remains still in an exploratory stage, [8] particularly for biological sites. Consequently there is a need for more experimental data on such systems that can be used as benchmarks.

A challenge in high-frequency EPR is to achieve the sensitivity needed to study transition-metal sites in biological molecules. Recently we have demonstrated that, using a single-mode cavity, it is possible to record high-quality EPR spectra in continuous-wave (cw) mode at 275.7 GHz (J band) of mM frozen solutions of the protein rubredoxin, whose active site in the oxidized state contains high-spin Fe^{3+} , see Chapter 2. [64] We were able to detect differences on the order of 1 GHz in the ZFS between rubredoxins from different organisms. Here we study the closely related active site of the protein desulforedoxin by multi-frequency EPR, both in its natural high-spin Fe^{3+} ($S = 5/2$) form and substituted with high-spin Co^{2+} ($S = 3/2$).

The rubredoxin class of small proteins found in sulfur-metabolizing bacteria and archaea is known to participate in electron transport. [10] The rubredoxin active site comprises an iron atom bound in an approximately tetrahedral geometry to four cysteine residues, which occur in two ...x-Cys-x-x-Cys-x... segments. Desulforedoxin is a homodimer consisting of two, 36 amino acid chains [65, 66] and has two equivalent $\text{Fe}(\text{S-Cys})_4$ active sites. The site geometry is again approximately tetrahedral, but the four cysteine residues occur in an ...x-Cys-x-x-Cys-x... and an ...x-Cys-Cys-x... segment. [67]

High-spin Fe^{3+} in a four-sulfur coordination has been studied both theoretically [68–70] and experimentally by several spectroscopic methods, both in model complexes, [71–74] and in rubredoxin. [56–58] High-spin Co^{2+} in a four-sulfur coordination has been studied to a lesser extent. [5, 75–78] Cobalt does not occur as

frequently in biological molecules as iron; yet it can be a rewarding spectroscopic probe, for instance as a substitute for diamagnetic Zn^{2+} . [79]

Desulforedoxin has been investigated by Moura *et al.* by X-band EPR and by Mössbauer spectroscopy. [57, 80] Moura *et al.* also recorded an X-band spectrum of Co(II)-substituted desulforedoxin. [81]

We report cw EPR spectra of a frozen solution of Fe(III)-desulforedoxin at J band and X band. The J-band spectra make it possible to determine the ZFS parameters accurately and reveal a small g -anisotropy. No J-band spectrum could be observed of Co(II)-substituted desulforedoxin. The X-band spectra of a frozen solution of Co(II)-desulforedoxin at multiple temperatures allow an estimate of the spin-Hamiltonian parameters. The typical variation in the geometry of the active site of a protein or enzyme, referred to as conformational strain, does not only make the detection of their EPR spectra challenging, but also complicates the analysis. The differences between the ZFS parameters of the high-spin Fe^{3+} site of desulforedoxin, the high-spin Fe^{3+} site of rubredoxin and the high-spin Co^{2+} substituted site of desulforedoxin are discussed.

3.2 Materials and methods

Desulforedoxin from *Desulfovibrio gigas* was expressed in *E. coli* and purified following a procedure similar to the procedure described in reference 47 for rubredoxin. Reconstitution with Co^{2+} was performed as described in reference 81. All proteins were kept in Tris buffer at pH 7.6. Samples for X-band EPR contained 20% glycerol.

The cw J-band EPR spectra were recorded on an in-house developed spectrometer, [9] using a probe head specialized for operation in cw mode as described in Chapter 2. [64] The effective sample volume, limited by the microwave cavity, is approximately 20 nl. The cw W-band (94.1 GHz) spectra were recorded on a Bruker Elexsys E680 spectrometer using a W-band “ENDOR” probe head with a cylindrical TE_{011} cavity in a CF935W flow cryostat (Oxford Instruments). Pulsed W-band (94.9 GHz) spectra were recorded on an in-house developed spectrometer. [82] The cw X-band spectra were also recorded on a Bruker Elexsys E680 spectrometer, using a TE_{102} rectangular cavity equipped with an ESR 900 Cryostat (Oxford Instruments).

3.3 Results and analysis

3.3.1 Desulforedoxin

Figure 3.1 shows cw J-band spectra of a frozen solution of desulforedoxin at 5 and 25 K. The complex spectrum covers a field range of more than 10 T. The 5 K spectrum shows three signals that lose intensity at elevated temperatures at 1.7 T

3. Multi-frequency EPR study of Fe^{3+} and Co^{2+} in the active site of desulfiredoxin

and around 4.7 and 6.5 T. These last two signals have a width of almost 1 T. In the 25 K spectrum signals appear around 7.0, 8.4 and 9.0 T.

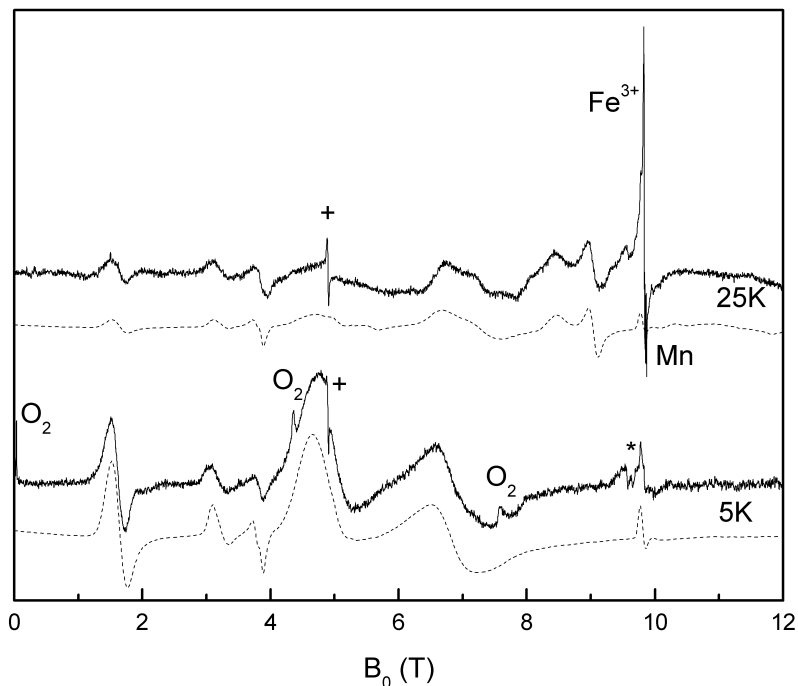


Figure 3.1: J-band cw EPR spectra of a 10 mM frozen solution of desulfiredoxin from *D. gigas* at 5 and 25 K. Experimental conditions: modulation amplitude: 3 mT, microwave power: $1 \mu\text{W}$, microwave frequency: 275.7 GHz. Solid lines: experimental spectra, dashed lines: spectra calculated using EasySpin and the spin-Hamiltonian parameters given in the text. Experimental spectra are smoothed by adjacent averaging and are baseline corrected at the low- and high-field end. An unknown impurity in the cavity gives a negative peak at 9.6 T, marked with \star . The following background signals arise from the frozen solution. At both temperatures a narrow transition at 4.9 T, marked with a +, is due to an unknown impurity. In the 5 K spectrum signals due to oxygen are observed. [51] At 25 K the strong transition around $g = 2$ (9.84 T), which has a shoulder on the low-field side, is due to an unknown rhombic high-spin Fe^{3+} contaminant and a detailed scan of the $g = 2$ region revealed six lines of Mn^{2+} .

Figure 3.2 shows cw X-band spectra of a frozen solution of desulfiredoxin at 5, 10 and 80 K. In the spectra three signals, at 86.6, 162 and 369 mT, lose intensity as temperature increases. The signals at 162 and 369 mT are considerably broader than the signal at 86.6 mT. A signal at 116.4 mT remains relatively strong at elevated temperatures.

The following spin Hamiltonian is used to interpret the EPR spectra arising from

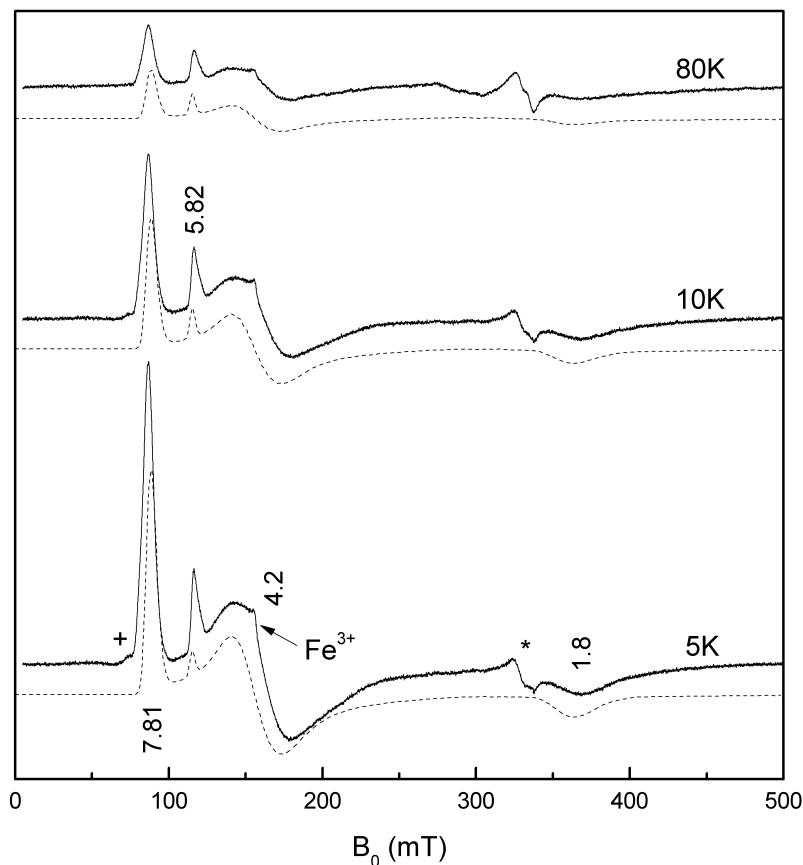


Figure 3.2: X-band cw EPR spectra of a 0.6 mM frozen solution of desulfuredoxin from *D. gigas* at 5, 10 and 80 K. Experimental conditions: modulation amplitude: 1 mT, microwave power: 5 and 10 K spectra: 1.3 mW, 80 K spectrum: 20 mW, microwave frequency: 9.491 GHz. Solid lines: experimental spectra, dashed lines: spectra calculated using EasySpin and the spin Hamiltonian parameters determined from the J-band spectra. The signal marked with a \star just below $g = 2$ (331 mT) is due to an impurity in the cavity. The signal marked with a $+$ is an unknown impurity in the frozen solution, which was also observed by Moura *et al.*, [57, 80] and the signal around $g = 4.3$ (157 mT) is due to an unknown rhombic high-spin Fe^{3+} contaminant.

high-spin Fe^{3+} , $S = 5/2$. [3]

$$H = \mu_B \vec{B}_0 \cdot \vec{g} \cdot \vec{S} + \vec{S} \cdot \vec{D} \cdot \vec{S} \quad (3.1)$$

The first term describes the electron Zeeman interaction. A first-order contribution from spin-orbit coupling induces g -anisotropy, but this anisotropy is expected to be small, since high-spin Fe^{3+} has an S ground state. The second term describes the ZFS, which splits the six magnetic sublevels into three Kramers doublets. The

3. Multi-frequency EPR study of Fe^{3+} and Co^{2+} in the active site of desulforedoxin

ZFS-tensor, \vec{D} , is symmetric, can be taken traceless, and is characterized by two parameters, D and E .

$$D = 3/2D_z, E = 1/2(D_x - D_y) \quad (3.2)$$

The rhombicity of \vec{D} is given by the ratio $\lambda = E/D$. The principal axes are chosen such that $|D_z| > |D_y| > |D_x|$ and $0 < \lambda < 1/3$.

From X-band EPR and Mössbauer spectra of desulforedoxin, Moura *et al.* estimated λ to be 0.08 and D to be 2 cm^{-1} or 60 GHz, [57, 80, 83] which explains the complexity of the desulforedoxin spectra in Figure 3.1. At J band the two terms in the spin Hamiltonian are comparable in size and the three Kramers doublets are intertwined. Analysis of the J-band spectra was performed by comparison to spectra calculated by numerical diagonalization of the spin Hamiltonian using the EPR simulation package EasySpin, [6] taking the parameters of Moura *et al.* as a starting point. The principal axes of the g -tensor are assumed to be collinear with those of the D -tensor. The experimental J-band spectra were best reproduced taking $D = 72 \text{ GHz}$ and $\lambda = 0.074$. Increasing the principal values of the g -tensor to above the free electron value improved the simulation: $g_x, g_y = 2.020$, $g_z = 2.025$. To reproduce the width and shape of the resonances in the J-band spectra a strain in D and E of 20% was taken into account using a first-order approximation,¹ cf. Discussion.

At X band the ZFS is larger than the microwave quantum of 9.5 GHz and only intra-doublet transitions can be observed. The system approaches the regime where each of the three Kramers doublets can be approximated as an effective $S' = 1/2$ system. [7] In this regime the anisotropic Zeeman splitting of each doublet is reflected in effective g' -values, g'_x , g'_y and g'_z , which depend on the g -values and λ , but not on D . The signals at the effective g' -values of 7.8, 4.2 and 1.8, which lose intensity at elevated temperatures, arise from the lowest doublet, $\pm 1/2$. The signal at $g' = 5.8$ is found to arise from the middle $\pm 3/2$ -doublet. The dashed lines in Figure 3.2 are spectra calculated using the parameters determined from the J-band spectra. In these spectra the line broadening was simulated by using a Gaussian distribution in λ of FWHM = 0.035, which corresponds to a distribution width of approximately 20% in D and E . The experimental spectra are reproduced, but there are small differences, on the order of 1 mT, between the calculated and experimental fields of resonance.

3.3.2 Co(II)-desulforedoxin

Figure 3.3 shows cw X-band spectra of a frozen solution of Co(II)-desulforedoxin at 5, 10, 25 and 40 K. At 5 K three transitions can be observed, around 110, 290,

¹See the online documentation on EasySpin.

and 420 mT. The middle- and high-field transitions are very broad and overlap. Upon increase of the temperature these three transitions lose intensity. At 25 and 40 K a new transition can be observed around 192 mT. The minimum found at low temperature around 420 mT shifts to around 380 mT at elevated temperatures. The transition around 110 mT preserves some of its intensity at 40 K and broadens.

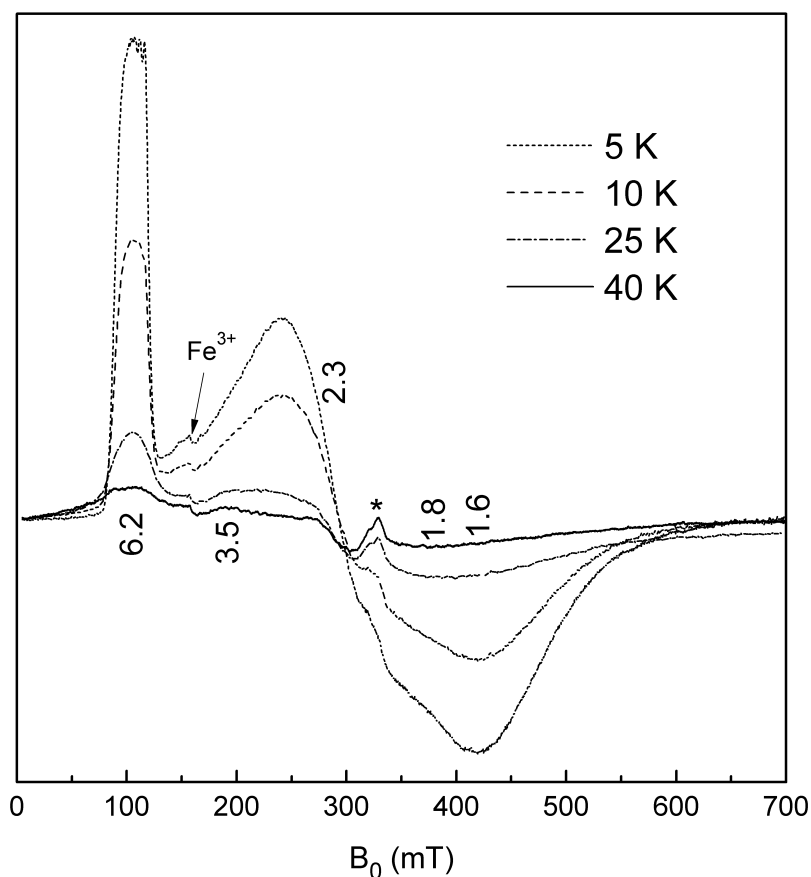


Figure 3.3: X-band cw EPR spectra of a 0.7 mM frozen solution of Co(II)-desulfiredoxin from *D. gigas* at 5, 10, 25 and 40 K. Experimental conditions: modulation amplitude: 1.5 mT, microwave power: 200 mW, microwave frequency: 9.495 GHz. A baseline was subtracted. The signal marked with a * around $g = 2$ (331 mT) is due to an impurity in the cavity. The signal around $g = 4.3$ (157 mT) is due to an unknown rhombic high-spin Fe^{3+} contaminant.

At J band no spectrum of Co(II)-desulfiredoxin could be detected. At W band an electron-spin-echo (ESE) detected EPR spectrum was observed at 1.7 K, shown in Figure 3.4. A spin echo due to Co(II)-desulfiredoxin was detected at magnetic fields above 1.1 T. The echo amplitude reached a maximum around 3.2 T. An attempt was made to measure the cw spectrum of a 4 mM frozen solution of Co(II)-desulfiredoxin

3. Multi-frequency EPR study of Fe^{3+} and Co^{2+} in the active site of desulfiredoxin

at W band. At 6.5 K a peak around 1 T showed up very weakly.

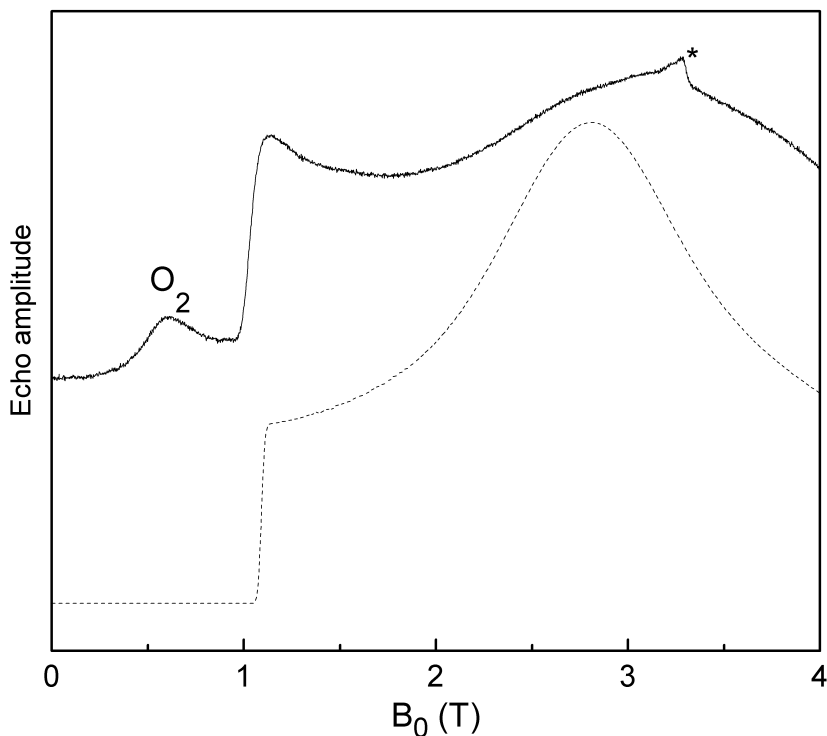


Figure 3.4: W-band ESE-detected EPR spectra of a 0.7 mM frozen solution of Co(II)-desulfiredoxin from *D. gigas* at 1.7 K. Experimental conditions: a two-pulse Hahn echo is generated by the pulse sequence $\pi/2 - \tau - \pi = 70 - 405 - 140$ ns, repetition time: 1 ms, microwave power: 1 mW, microwave frequency: 94.9 GHz. Solid line: experimental spectrum, dashed line: spectrum calculated using EasySpin and the spin-Hamiltonian parameters given in the text. The signal around 0.6 T results from oxygen in the frozen solution. [51] The signal marked with a \star at $g = 2$ (3.39 T) results from an unknown impurity.

To interpret the high-spin Co^{2+} , $S = 3/2$, spectra a term describing the hyperfine interaction with the ^{59}Co nucleus ($I = 7/2$) should be added to the spin Hamiltonian 3.1.

$$H = \mu_B \vec{B}_0 \cdot \vec{g} \cdot \vec{S} + \vec{S} \cdot \vec{D} \cdot \vec{S} + \vec{S} \cdot \vec{A} \cdot \vec{I} \quad (3.3)$$

The ground state of high-spin Co^{2+} is an F state. A first-order contribution from spin-orbit coupling induces considerable g -anisotropy. The ZFS, which is large, typically hundreds of GHz, splits the four energy levels of the ground state into two Kramers doublets. The contribution of a nuclear Zeeman interaction by cobalt can be neglected.

Analysis of the X-band spectra is performed under the assumption that the effective $S' = 1/2$ description of the doublets is valid. For an $S = 3/2$ system the effective g'_i -values are related to the g_i -values by [7, 84, 85]

$$\begin{aligned} g'_x &= g_x \left(1 \pm \frac{1 - 3\lambda}{\sqrt{1 + 3\lambda^2}} \right) \\ g'_y &= g_y \left(\pm 1 + \frac{1 + 3\lambda}{\sqrt{1 + 3\lambda^2}} \right) \\ g'_z &= g_z \left(\mp 1 + \frac{2}{\sqrt{1 + 3\lambda^2}} \right) \end{aligned} \quad (3.4)$$

The upper signs refer to the $\pm 1/2$ doublet and the lower signs to the $\pm 3/2$ doublet. Note that these relations presume that the principal axes of the g - and D -tensor are collinear.

The transitions observed in the 5 K spectrum, at effective g' -values 6.2, 2.3 and 1.6 respectively, are due to the anisotropic splitting of the lower Kramers doublet. At 25 and 40 K the spectra are dominated by three transitions at effective g' -values 6.2 (110 mT), 3.5 (192 mT) and 1.8 (380 mT), which arise from the upper Kramers doublet. Following Equation 3.4, the transition at $g' = 3.5$ must be the g'_x transition of the $\pm 1/2$ doublet. Hence, the $\pm 1/2$ doublet is higher in energy and D is negative. Equation 3.4 and a minimization procedure were used to estimate the values of λ and g_x , g_y , and g_z from the six observed effective g' -values. This gave $\lambda = 0.26$, $g_x = 2.9$, $g_y = 2.4$, and $g_z = 2.2$. These values are, together with a large, negative D , used to simulate the Co(II)-desulforedoxin spectra with EasySpin, [6] as shown for the 5 K spectrum in Figure 3.5. The shape of the experimental spectra is qualitatively reproduced by the simulation, but fine tuning is clearly needed. This has not been pursued, see Discussion.

To simulate line broadening in the X-band spectra, a Gaussian distribution in λ of FWHM 0.035 was used. The broadening of the $g'_z(\pm 3/2)$ transition is mainly due to a (partially resolved) hyperfine interaction with the ^{59}Co nucleus of approximately $A_z = 150$ MHz.

The dashed spectrum in Figure 3.4 is the absorption spectrum calculated using EasySpin and the spin-Hamiltonian parameters estimated from the frozen solution cw X-band spectra. It reproduces qualitatively the ESE detected EPR spectrum, i.e., the onset of the spin echo at 1.1 T, which corresponds to $g'_z(\pm 3/2) = 6.2$, and the broad field range over which an echo is observed.

3.4 Discussion

The cw J-band spectra of the frozen solution of desulforedoxin are well reproduced by spectra calculated from numerical diagonalization of the spin Hamiltonian, [6]

3. Multi-frequency EPR study of Fe^{3+} and Co^{2+} in the active site of desulforedoxin

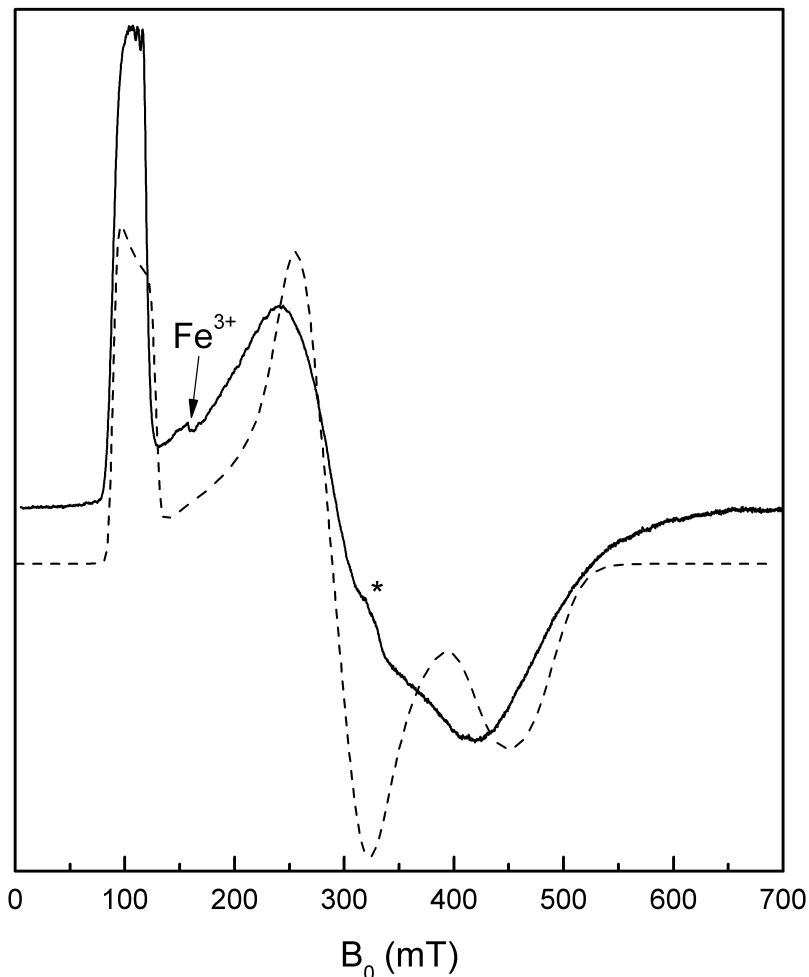


Figure 3.5: X-band cw EPR spectrum of a 0.7 mM frozen solution of Co(II)-desulforedoxin from *D. gigas* at 5 K. Solid line: experimental spectrum, dashed line: spectrum calculated using EasySpin and the spin-Hamiltonian parameters given in the text. The signal marked with a \star around $g = 2$ (331 mT) is due to an impurity in the cavity. The signal around $g = 4.3$ (157 mT) is due to an unknown rhombic high-spin Fe^{3+} contaminant.

see Figure 3.1, optimally with the ZFS parameters $D = 72 \pm 1$ GHz and $\lambda = 0.074 \pm 0.002$, and a small g -anisotropy, $g_x, g_y = 2.020 \pm 0.001$, $g_z = 2.025 \pm 0.005$. The uncertainty in a parameter was estimated from the calculated shift of the J-band resonances upon a change in that parameter. Because the microwave quantum ($\nu = 275.7$ GHz) is larger than the ZFS, inter-doublet transitions are possible and the spectrum is very sensitive to both E and D . An X-band spectrum, on the other hand, depends on $\lambda = E/D$, and D needs to be estimated via an elaborate

temperature study. [56] Moreover, at X band the small g -anisotropy of high-spin Fe^{3+} is not resolved.

Conformational strain is typical for proteins and enzymes. The geometrical variations affect the electronic structure of active sites, which translates into a distribution in the ZFS parameters for high-spin Fe^{3+} [58, 86] and in a distribution in the ZFS parameters and the principal values of the g -tensor for high-spin Co^{2+} . This does not only result in line broadening, which can make it difficult to detect the EPR spectrum of a biological site, but it may also deform the spectrum, which complicates its analysis. Particularly, if a change in a spin-Hamiltonian parameter results in a large change of the transition probability, strain can result in a shift of what appears to be the average field of resonance in the experimental EPR spectra.

In order to reproduce the line widths in the experimental J-band spectra of desulforedoxin, the spectra were simulated using EasySpin with a strain of about 20% in D and E . A first-order approximation is used, in which the spectrum was convoluted with a Gaussian of a width proportional to the derivative of the resonance field of a given transition with respect to, for instance, D ; the proportionality constant is chosen by the user. This approximation is valid if the strain is much smaller than the parameter itself. In the high-field limit, $\mu_B \vec{B}_0 \cdot \vec{g} \cdot \vec{S} \gg \vec{S} \cdot \vec{D} \cdot \vec{S}$, where the magnetic field at which the resonances in a frozen solution spectrum are observed depends linearly on the principal values of the D -tensor, [45] the approximation may also be valid for larger strains in D and E , if the transition probability does not depend strongly on these parameters. This was found to be the case for Fe(III)-rubredoxin, $D = 48$ GHz, by comparison to spectra calculated using a distribution in D and E . [64] For desulforedoxin, $D = 72$ GHz, such a comparison was not feasible, because the calculation of the individual spectra is too time consuming.

The X-band spectra of Fe(III)- and Co(II)-desulforedoxin are typical of a site that experiences large conformational strain: the resonances at low g -values are very broad, while the resonances at high g -values are narrower. The distributions in g'_x , g'_y and g'_z are of similar width, but the distribution in the resonance fields will be broader for the smaller g'_i -values. To simulate the experimental X-band spectra of both sites, the effect of conformational strain was taken into account by using a Gaussian distribution in λ . For Fe(III)-desulforedoxin the experimental line width was well reproduced, but small deviations in the resonance fields remained between the experimental spectra and the calculated spectra when using the spin-Hamiltonian parameters determined from the J-band spectra. For Co(II)-desulforedoxin the line width is poorly reproduced and it is hard to say if the resonance fields are reproduced properly. Of course, a proper simulation of the Co(II)-desulforedoxin X-band spectra requires not only a distribution in λ , but also in g_x , g_y and g_z .

For Co(II)-desulforedoxin not only the effect of conformational strain, but also the spin-Hamiltonian parameters are uncertain. The values of the parameters used in the simulation of the X-band spectra were merely an estimate. Following Equa-

3. Multi-frequency EPR study of Fe^{3+} and Co^{2+} in the active site of desulfiredoxin

tion 3.4 the only possible assignment for the peak observed at $g' = 3.5$ at elevated temperatures is the g'_x transition of the $\pm 1/2$ doublet, making $D < 0$. However, the value of 2.9 for g_x , which has to be invoked to fit the observed $g'_x(\pm 1/2) = 3.5$ and, particularly, the $g'_x(\pm 3/2) = 2.3$ transition, is unusually large. [87, 88] Besides the very large ZFS and the difficulties encountered when simulating the effects of conformational strain, there is a third reason that the X-band spectrum of Co(II)-desulfiredoxin can not provide more accurate information on the electronic structure. The covalent character of the bonding with the soft sulfur ligands may cause the principal axes of the D - and g -tensors to be non-collinear, [8, 89, 90] which implies that the g -values can not be calculated from Equation 3.4. Moreover, analysis by comparison to spectra calculated by numerical diagonalization of the spin Hamiltonian is not an option, since the relative orientation of the principal axes of interaction tensors is now a variable.

High-frequency EPR spectra of Co(II)-desulfiredoxin could be helpful. First, they can provide information on the relative orientation of the principal axes of the D - and g -tensors. At X band the direction of the effective magnetic field is dominated by the D -tensor. If spectra are recorded at higher frequency and higher magnetic field, the influence of the Zeeman interaction on the direction of the effective magnetic field becomes noticeable. Also, at higher frequency deviations from the effective $S' = 1/2$ picture start to occur, an effect that was used in the multi-frequency EPR study of a high-spin Co^{2+} complex to estimate D . [5] Or, ideally, the regime $\nu \approx D$ is reached and inter-doublet transitions become possible. [91–94]

Unfortunately no spectrum of Co(II)-desulfiredoxin could be observed in cw at J-band. The ESE-detected W-band spectrum corroborates our interpretation of the cw X-band spectra, but fine tuning of the parameters based on this spectrum is complicated by anisotropic relaxation times. No high-frequency studies of high-spin Co^{2+} in the active site of a protein are found in literature. The reason that high-frequency spectra of Co(II)-substituted desulfiredoxin, and of biological high-spin Co^{2+} systems in general, are hard to come by is the large g -anisotropy. Conformational strain results in a distribution in g_i , on top of a distribution in D and E , which, as long as the regime $\nu \approx D$ is not reached, causes a severe broadening of the resonances, particularly at high magnetic fields. Hence, the absence of a spectrum at J band suggests that $|D|$ is larger than about 300 GHz.

If we compare the spin-Hamiltonian parameters of the active site of desulfiredoxin to those of the active site of rubredoxin, we notice remarkable differences. First, the rhombicity of the ZFS-tensor of the high-spin Fe^{3+} sites differs considerably for desulfiredoxin and rubredoxin. The D and λ of rubredoxin from *D. gigas* are known to be 48.5 GHz and 0.26, see Chapter 2, [64] while we find $D = 72$ GHz and $\lambda = 0.074$ for desulfiredoxin. Second, while D is positive for the Fe^{3+} sites, D is negative for the Co(II)-substituted active site of desulfiredoxin and, moreover, the rhombicity of Co(II)-desulfiredoxin is comparable to that of the Fe^{3+} site of rubre-

doxin: $D < -300$ GHz and $\lambda = 0.26$. At this point it would be desirable to know the ZFS parameters of Co(II)-substituted rubredoxin, but, unfortunately, we were not successful in obtaining an EPR spectrum of Co(II)-rubredoxin, despite considerable effort, cf. Appendix C. However, the absence of an EPR spectrum suggests a $\lambda \approx 0$ and $D < 0$. In this situation a transition within the lowest doublet is (almost) forbidden and at elevated temperatures, where the higher doublet becomes populated, the transitions within this doublet may broaden strongly due to fast relaxation.

The electronic structure of sulfur-coordinated transition-metal sites is known to depend on the structure of the site beyond the first coordination sphere. [68–70, 74, 95] For both rubredoxin and desulfuredoxin from *D. gigas* the structures are known to a high resolution. [14, 46, 66] The structure of Co(II)-substituted rubredoxin is indistinguishable from the structure of Fe(III)-rubredoxin by X-ray diffraction. [96] No X-ray diffraction study of the structure of Co(II)-substituted desulfuredoxin has been performed, but we will assume that its structure is the same as that of Fe(III)-desulfuredoxin.

Figure 3.6a shows the structure of the active site of rubredoxin. The $\text{Fe}(\text{SC})_4$ geometry is approximately what is referred to in reference 70 as the $D_{2d}(1)$ or double-bird geometry. This conformation is the combined result of the site being built up from four cysteine residues on two amino acid strands and the sulfur-lone-pair repulsion. The FeS_4 core is elongated from T_d symmetry (two smaller angles and four larger ones). [95] Figure 3.6b shows the structure of the active site of desulfuredoxin. The angle S-Fe-S involving Cys28 and Cys29 is relatively large, 121.5° , due to the adjacency of the two cysteines, and $\text{C}_9\text{-S}_9\text{-Fe-S}_{29}\text{-C}_{29}$ is not able to assume the bird geometry on the Cys29 side.

Interpretation of the ZFS parameters in relation to the structure of the active sites is far from straightforward. Ligand-field considerations concerning the metal d -orbitals are of limited applicability because of the significant (anisotropic) covalency of the metal-sulfur bonds. Recently, the experimental ZFS parameters of a number of high-spin Co^{2+} complexes have been well reproduced by correlated ab-initio calculations. [97] In particular, for the truncated double-bird core of the complex $[\text{Co}(\text{SPh})_4]^{2-}$ a large negative D and $\lambda = 0$ were calculated. [76] The approximate double-bird geometry of the rubredoxin active site suggests similar ZFS parameters for the high-spin Co^{2+} site, which would be in line with the ZFS parameters predicted from the absence of an EPR spectrum. In this respect the $\lambda = 0.26$ of the Co(II)-substituted active site of desulfuredoxin, which is considerably more asymmetric than the rubredoxin site, is in line with expectations.

The $\lambda = 0$ for the double-bird geometry or D_{2d} symmetry of the Co^{2+} site of the $[\text{Co}(\text{SPh})_4]^{2-}$ complex does not merely follow from the ab initio calculations. All interaction tensors must be axial if the symmetry of the site is S_4 or higher. From this perspective the $\lambda = 0.26$ observed for high-spin Fe^{3+} rubredoxin is remarkable. Moreover, a ZFS tensor that is closer to axial, $\lambda = 0.074$, is observed for high-spin Fe^{3+} desulfuredoxin. These observations illustrate how difficult it is to predict the

3. Multi-frequency EPR study of Fe^{3+} and Co^{2+} in the active site of desulforedoxin

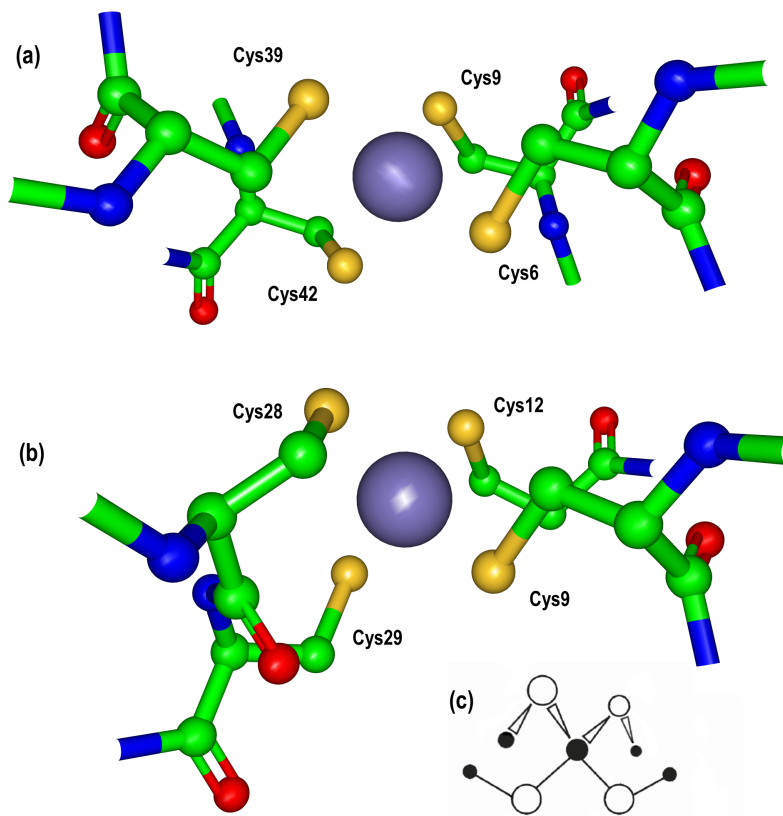


Figure 3.6: a) The structure of the active site of rubredoxin from *D. gigas*. b) The structure of the active site of desulforedoxin from *D. gigas*. c) Schematic drawing of the double-bird geometry.

effects of deviations from a presumed symmetry of a site on its electronic structure.

The deviations of symmetry in the sites of rubredoxin and desulforedoxin affect the electronic structure differently, depending on whether the site is occupied by high-spin Co^{2+} ($3d^7$ configuration) or high-spin Fe^{3+} ($3d^5$ configuration). These differences arise because the former has a 4F ground state, while the latter has a 6S ground state. The in-state orbital angular momentum of the high-spin Co^{2+} may be quenched by the low symmetry of the site, but is easily restored by mixing of the ground state with nearby excited states and a g -anisotropy and large ZFS are expected. [84] On the other hand, for high-spin Fe^{3+} no in-state orbital angular momentum and no ligand field excited states of the same multiplicity are present. The origin of the observed ZFS, which is much smaller than for high-spin Co^{2+} , lies mainly in anisotropy in the covalency, which even reverses the sign of D . [71, 72, 98]

3.5 Conclusion

High-frequency EPR spectroscopy provides valuable information on the electronic structure of high-spin transition-metal sites in biological systems. At the same time, the observation and analysis of the spectra is not straightforward, particularly in the case of high-spin Co^{2+} . Attempts to interpret the ZFS tensors and g -anisotropy observed for high-spin Fe^{3+} and high-spin Co^{2+} in the active sites of desulforedoxin and rubredoxin illustrate the necessity of further development of advanced quantum-chemical calculations, which can interrelate the geometric structure and electronic structure of these active sites.

3. Multi-frequency EPR study of Fe^{3+} and Co^{2+} in the active site of desulforedoxin

Chapter 4

A W-band pulsed EPR/ENDOR study of Co(II)S₄ coordination in the Co[(SPh₂)(SPⁱPr₂)N]₂ complex

Spin-echo detection at 95 GHz enables an electron-paramagnetic-resonance study of a cobalt complex with a bio-mimetic coordination of the transition metal by four sulfur atoms. A magnetically diluted single crystal of the complex has been investigated in great detail. Electron-nuclear double-resonance signals were observed of ligand nuclei and complete hyperfine tensors of the distinct phosphorus nuclei were derived, assigned and discussed.

Silvia Sottini, Guinevere Mathies, Peter Gast, Dimitrios Maganas, Panayotis Kyritsis and Edgar J. J. Groenen, *Phys. Chem. Chem. Phys.*, 11 (2009) 6727-6732.

4. A W-band pulsed EPR/ENDOR study of Co(II)S₄ coordination in the Co[(SPh₂)(SPⁱPr₂)N]₂ complex

4.1 Introduction

Transition-metal ions with a sulfur-rich coordination sphere are abundant active sites in proteins and enzymes. [99] Bonding between metal ions and sulfur-containing ligands shows up in various coordination geometries and a correspondingly large flexibility exists with respect to electronic structure. [100] Among the biologically important redox-active transition-metal ions, manganese, iron and copper are most easily accessible and therefore usually constitute the catalytically active sites of redox metalloenzymes. [99] However, cobalt-based active sites have also been found in a number of enzymes. [101, 102] In addition to these native sites, cobalt sites have been created by substitution of Co²⁺ for Fe²⁺ or Cu²⁺, [96, 103] and mostly for spectroscopically silent and diamagnetic metal ions like Zn²⁺ or Cd²⁺. [104, 105] In the latter case, the reason for the substitution is that Co²⁺ sites are amenable to biophysical characterization by optical spectroscopy, magnetic susceptibility and magnetic resonance methods. In this context, cobalt analogue complexes have been synthesized to mimic the active sites in proteins and enzymes. [106] Here we consider such a complex in which cobalt is coordinated by four sulfurs.

The paramagnetic nature of the Co²⁺ 3d⁷ configuration enables the application of electron paramagnetic resonance (EPR) in the study of the electronic structure of the metal site. However, the high spin ($S = 3/2$) configuration in the typically encountered Co²⁺ sites complicates the use and interpretation of EPR because of the rather large zero-field splitting (ZFS) between the $\pm 1/2$ and $\pm 3/2$ Kramers doublets. Studies on Co(II)S₄ coordination by continuous-wave EPR at X band have been reported by Fukui *et al.* [75–77] In recent years, developments have taken place in EPR technology, which have largely enhanced the possibilities to investigate such paramagnetic centers. [107] In particular, this includes the development of spectrometers working at high magnetic fields and high microwave frequencies, i.e., much higher than the commonly used 9 GHz.

Recently we have studied two complexes with Co(II)S₄ coordination by EPR spectroscopy, namely Co[(SPh₂)₂N]₂ and Co[(SPh₂)(SPⁱPr₂)N]₂, which will be denoted as Co^{Ph,Ph}L₂ and Co^{iPr,Ph}L₂, respectively. [5] Powders and single crystals of these compounds have been investigated by continuous-wave EPR spectroscopy at 9, 95 and 275 GHz. The ZFS, close to axial for Co^{Ph,Ph}L₂ and rhombic for Co^{iPr,Ph}L₂, has a magnitude of 23.8 and 29.6 cm⁻¹, respectively. For the corresponding diamagnetically diluted samples, 1% CoL₂ in the analogous ZnL₂ complex, the cobalt-hyperfine splitting was resolved and could be analyzed. Interpretation of the data in terms of the electronic structure, and in particular the characteristics of the cobalt-sulfur bonds, requires a study of the spin delocalization over the ligands. The present paper represents a first step in that direction.

In this work, we report on the Co^{iPr,Ph}L₂ complex [108] (Figure 4.1), which we investigated by pulsed EPR spectroscopy at 95 GHz (W band). Electron spin echoes (ESEs) have been detected for diamagnetically diluted Co^{iPr,Ph}L₂/Zn^{iPr,Ph}L₂

single crystals. Stimulated echoes were observed and pulsed electron-nuclear double-resonance (ENDOR) experiments were performed. The spectra show ENDOR signals from the ligand phosphorus, nitrogen and hydrogen atoms. The complete hyperfine tensors for the phosphorus atoms are derived, assigned and discussed.

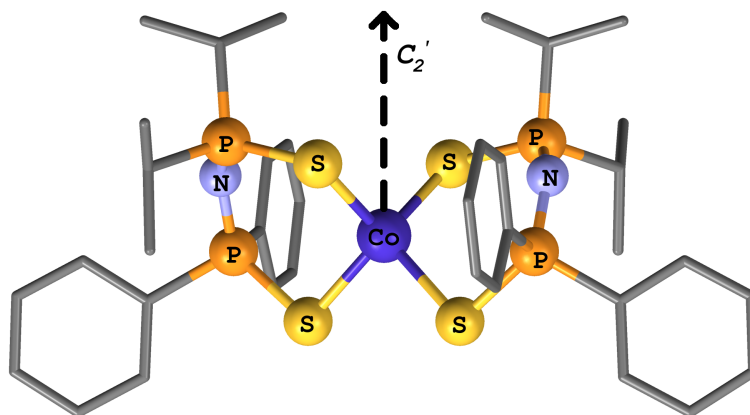


Figure 4.1: The molecular structure of $\text{Co}[(\text{SPPPh}_2)(\text{SP}^{\text{iPr}}_2)\text{N}]_2$.

4.2 Materials and methods

Magnetically diluted single crystals of 1% $\text{Co}^{\text{iPr,Ph}}\text{L}_2$ in $\text{Zn}^{\text{iPr,Ph}}\text{L}_2$ have been investigated. A typical size of these co-crystals was $0.3 \times 0.5 \times 0.7$ mm, and the synthesis of the complex is described in reference 108. The crystal was mounted in a quartz tube of inner diameter 0.60 mm and outer diameter 0.84 mm, which was placed into the cylindrical cavity of our homebuilt W-band spectrometer, [82] which was upgraded recently. The sample tube and the magnet can be rotated around independent axes thus enabling experiments at every possible orientation of the magnetic field with respect to the crystal, without remounting the crystal. The sample was kept for one week under helium atmosphere before measuring, because otherwise a background signal was present in the EPR spectra.

All the experiments were carried out at 1.6 K and at a microwave frequency of 94.9 GHz. For the EPR experiments, a two-pulse Hahn-echo sequence was employed using microwave pulses of 80 and 160 ns separated by 140 ns at a repetition rate of 10 kHz. For the ENDOR experiments, a Mims type three-pulse sequence was used. The three microwave pulses had a length of 100 ns. The time between the first and the second microwave pulse was 220 ns, the time between the second and the third microwave pulse had a variable length. The length of the radio-wave pulse varied with the orientation between 20 and 60 ms, because the relaxation times change with

4. A W-band pulsed EPR/ENDOR study of Co(II)S₄ coordination in the Co[(SPPPh₂)(SPⁱPr₂)N]₂ complex

the orientation of the magnetic field with respect to the crystal. The repetition rate was 1 kHz. Data analysis was performed using a Matlab version of the optimization package Minuit (CERN).

4.3 Theoretical background

The description of the EPR and ENDOR spectra of the high-spin Co²⁺ complex ($S = 3/2$) starts from an electron spin Hamiltonian, which includes the zero-field splitting (ZFS) and the electron Zeeman interaction

$$H_e = \vec{S} \cdot \vec{D} \cdot \vec{S} + \mu_B \vec{B} \cdot \vec{g} \cdot \vec{S} \quad (4.1)$$

where \vec{S} represents the electron-spin angular momentum operator and the D and g tensors represent the interactions. A full description of the $S = 3/2$ case can be found in textbooks. [109]

The ZFS gives rise to two Kramers doublets and, although m_s is not a good quantum number, we will refer to these as $\pm 1/2$ and $\pm 3/2$. In a small magnetic field, such that the electron Zeeman interaction is much smaller than the zero-field interaction, the energy of the four levels may be obtained by considering the doublets separately. In this effective spin 1/2 picture, the energies for both the $\pm 1/2$ and $\pm 3/2$ doublet may be written as

$$E = \pm \frac{1}{2} \mu_B B \sqrt{\sum_{\beta} \left(\sum_{\alpha} \ell_{\alpha} g'_{\alpha\beta} \right)^2} \quad (4.2)$$

Here $\alpha, \beta = x, y, z$ and $\vec{\ell}$ represents a unit vector in the direction of \vec{B} in the reference axes system x, y, z . The effective g' matrix is defined by

$$g'_{\alpha\beta} = g_{\alpha\beta} \omega_{\beta} \quad (4.3)$$

with

$$\begin{aligned} \omega_x &= 2\sqrt{3} \cos \theta \sin \theta + 2 \sin^2 \theta \\ \omega_y &= 2\sqrt{3} \cos \theta \sin \theta - 2 \sin^2 \theta \\ \omega_z &= 3 \cos^2 \theta - \sin^2 \theta \end{aligned} \quad (4.4)$$

for the $\pm 3/2$ doublet. The corresponding expressions for the $\pm 1/2$ doublet are obtained by replacing $\cos \theta$ by $-\sin \theta$ and $\sin \theta$ by $\cos \theta$. The angle θ is related to the ZFS parameters by $\tan 2\theta = \sqrt{3}E/D$.

For Co^{iPr,Ph}L₂ the splitting between the doublets in zero field amounts to about 900 GHz as compared to the microwave quantum of 94.9 GHz. The EPR transition

in the low-temperature W-band spectrum corresponds to the transition within the Kramers doublet of lowest energy. From the cw EPR study on $\text{Co}^{\text{iPr,Ph}}\text{L}_2$ at X band, we found $E/D = -0.33$. [5] The ZFS is maximum rhombic, which implies that the difference in the expressions in Equation 4.4 for the $\pm 1/2$ and $\pm 3/2$ doublets corresponds to an interchange of the x and z labels. The ω values are the same. Consequently, whether the $\pm 1/2$ and $\pm 3/2$ doublet is the lowest, cannot be concluded. From here on, we will consider D to be negative, which corresponds to the assumption that $\pm 3/2$ is the lowest Kramers doublet. Our results are not dependent upon this choice, because of the rhombicity of the ZFS tensor.

The principal axes of the g' tensor at W band are parallel to those of the ZFS tensor owing to the negligible contribution of the off-diagonal terms of the g tensor to the g' tensor. This allows us to translate the experimental data into the reference system in which the ZFS tensor is diagonal.

In order to describe the phosphorus ($I = 1/2$) ENDOR spectra, we have to consider the nuclear Zeeman interaction and the hyperfine interaction. In case the mixing of the electron-spin states by the hyperfine interaction is negligible, the nuclear spin Hamiltonian may be written as

$$H_n = -g_P \mu_n \vec{I} \cdot \vec{B} + \langle \vec{S} \rangle \cdot \vec{A} \cdot \vec{I} \quad (4.5)$$

where $\langle \vec{S} \rangle$ represents the expectation value of the electron-spin angular momentum. This expectation value can be calculated from the electron-spin eigenstates obtained through the exact diagonalization of the electron spin Hamiltonian.

For each phosphorus nuclear spin interacting with the electron spin, two transitions may show up in the ENDOR spectrum, symmetrically shifted with respect to the phosphorus nuclear Zeeman frequency.

4.4 Results

ESE-detected EPR spectra of a single crystal of 1% $\text{Co}^{\text{iPr,Ph}}\text{L}_2/\text{Zn}^{\text{iPr,Ph}}\text{L}_2$ have been obtained for many orientations of the magnetic field with respect to the crystal. The measurements were carried out in the $x'y'$, $y'z'$ and $z'x'$ planes, where x', y', z' refers to the principal axes system of the effective g' tensor. In Figure 4.2, spectra for orientations of the field in the $y'z'$ and $x'y'$ planes are shown. For each orientation we observe a single line. For orientations close to z' , the line reveals sub-structure owing to the resolved cobalt hyperfine interaction. The system shows a marked anisotropy in T_2 , which affects the intensity of the resonant line for different orientations of the field, and in T_1 . Both become faster on going towards z' . The effective g' tensor was extracted from the data using Equation 4.2 and its principal values at W band are 1.61, 2.34 and 6.42.

The ENDOR spectrum measured on the same crystal in the frequency range up to 150 MHz and for an orientation of the magnetic field along y' is shown in Figure 4.3.

4. A W-band pulsed EPR/ENDOR study of Co(II)S_4 coordination in the $\text{Co}[(\text{SPh}_2)(\text{SP}^i\text{Pr}_2)\text{N}]_2$ complex

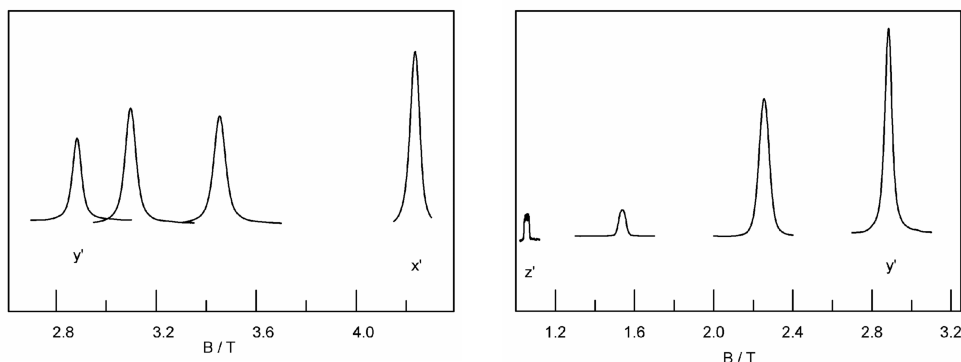


Figure 4.2: W-Band ESE-detected EPR spectra of a crystal of 1% $\text{Co}^{i\text{Pr,Ph}}\text{L}_2/\text{Zn}^{i\text{Pr,Ph}}\text{L}_2$ at different orientations of the magnetic field with respect to the crystal. The spectra in the upper figure correspond to orientations in the $x'y'$ plane, in the lower figure in the $z'y'$ plane. At z' the cobalt hyperfine splitting of the line is resolved.

Signals around the nuclear Zeeman frequency of nitrogen, phosphorus and hydrogen are easily recognizable. There is a fourth, broader signal in the spectrum, which might derive from cobalt.

Zooming into the phosphorus region of the spectrum, Figure 4.4 shows the ENDOR spectrum for an orientation of the magnetic field in the $x'y'$ plane. Four ENDOR transitions are seen between 58 and 62 MHz, one of which shows a line width different from the others. The ENDOR frequencies are not symmetrically displaced around the nuclear Zeeman frequency of phosphorus, i.e., 59.586 MHz for a magnetic field of 3.454 T. The ENDOR spectra were obtained for many other orientations of the magnetic field with respect to the crystal, adjusting the field strength to remain in resonance with the EPR transition. Orientations were chosen in five planes, three of which concerned the principal planes of the effective g' tensor. For none of the orientations more than four ENDOR lines were found in the phosphorus region. The repetition rate was varied between 1 kHz and 1 Hz in order to check for saturation of nuclear transitions, but no extra lines showed up. In addition, experiments were performed varying the length of the rf pulse during the mixing period, the power of the rf pulse and the duration of the mixing period. Also in these experiments no other lines were detected. For certain orientations of the field in the $x'y'$ plane, lines with deviating width and shape were observed. These were not taken into account for the subsequent analysis.

Resonances belonging to four distinct phosphorus nuclei can be followed through the planes. The A tensors were derived from the data using Equation 4.5, in which we assumed that the observed ENDOR lines correspond to the electron-spin β manifold.

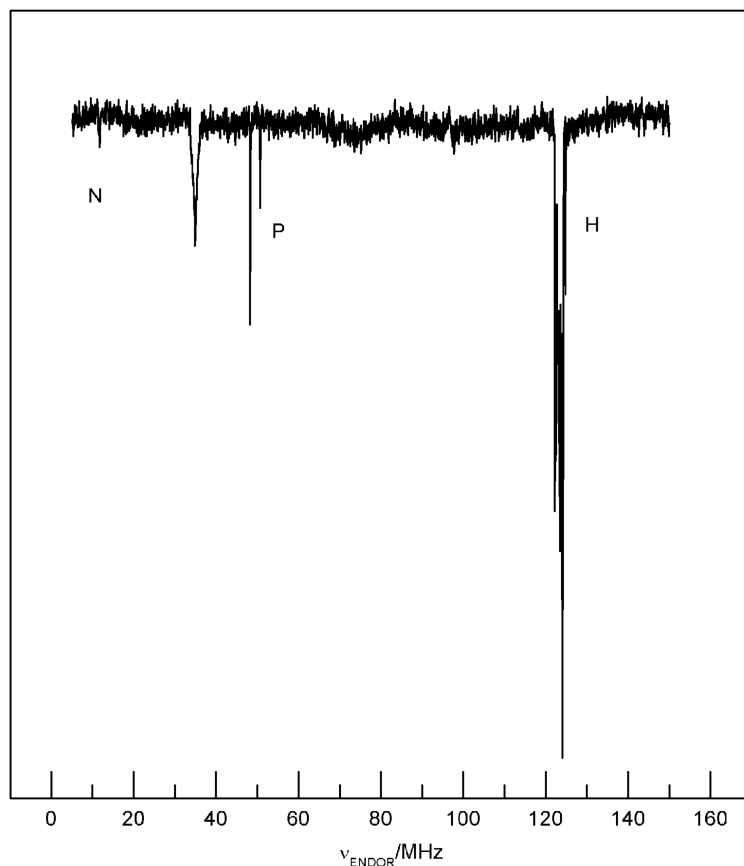


Figure 4.3: The pulsed ENDOR spectrum of a single crystal of 1% $\text{Co}^{\text{iPr,Ph}}\text{L}_2/\text{Zn}^{\text{iPr,Ph}}\text{L}_2$ with the magnetic field parallel to the y' axis of the g' tensor and $B = 2.884$ T. In the spectrum, resonances due to hydrogen, phosphorus and nitrogen nuclei are observed.

Under the assumption that the principal axes system of the g tensor coincides with that of the ZFS tensor, i.e., that the off-diagonal terms of the g tensor are negligible, the g values were derived from the ESE-detected EPR data using Equation 4.1 and the ZFS parameters D and E of -387 and 126 GHz, as known from the cw EPR study on $\text{Co}^{\text{iPr,Ph}}\text{L}_2$. [5] Subsequently, the electron spin Hamiltonian was diagonalized and the expectation value $\langle \vec{S} \rangle$ calculated. Finally, a fit of the observed ENDOR frequencies using Equation 4.5 was performed. Figure 4.5 shows the quality of the fits for all the planes investigated. Most of the frequencies not taken into account in the fit (the open dots in Figure 4.5) also are on the lines that result from the fit. Some of these frequencies in the $x'y'$ plane slightly deviate, but the deviations are within the line widths of the corresponding ENDOR lines.¹ The resulting four A

¹After publication of this work it was realized that these deviations arise from what Abragam

4. A W-band pulsed EPR/ENDOR study of Co(II)S_4 coordination in the $\text{Co}[(\text{SPPH}_2)(\text{SP}^i\text{Pr}_2)\text{N}]_2$ complex

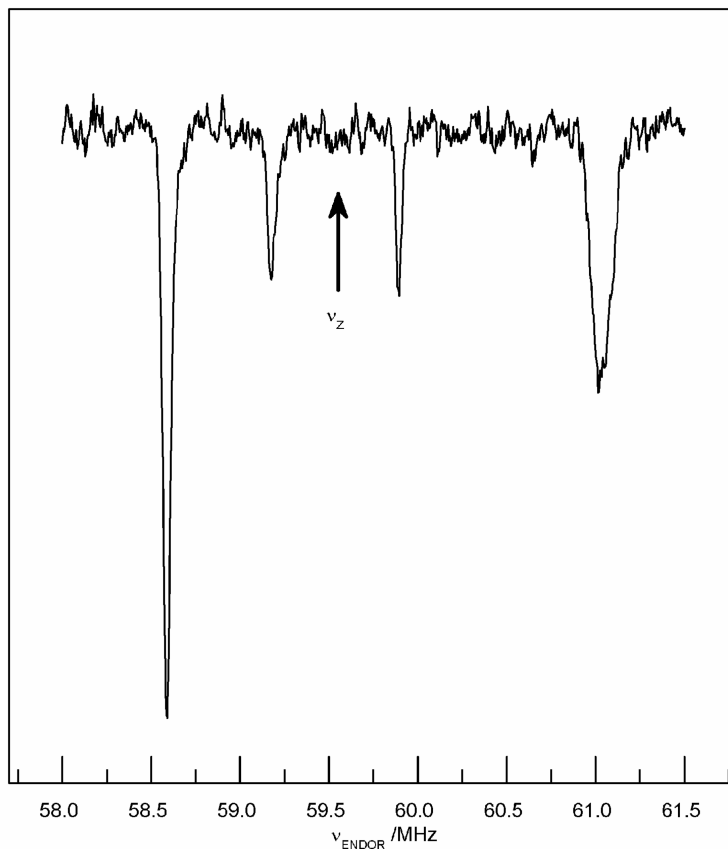


Figure 4.4: The pulsed ENDOR spectrum of a single crystal of 1% $\text{Co}^{\text{iPr,Ph}}\text{L}_2/\text{Zn}^{\text{iPr,Ph}}\text{L}_2$ taken at 40 degrees from x' in the $x'y'$ plane of the g' tensor at a field strength of 3.454 T. The spectrum shows four ENDOR lines in the region around the nuclear Zeeman frequency (ν_Z) of phosphorus.

tensors are presented in Table 4.1. The tensors A_1 and A_2 are similar, as well as the tensors A_3 and A_4 .

The analysis relies on the assumption that the principal axes of the ZFS and g tensors coincide and on the values of D and E . In order to estimate the uncertainty in the A tensors that results from these assumptions, we varied the ratio E/D in the range $(-0.3, -0.333)$ and the values of D and E by 10%, while their ratio was kept the same. In all cases, variations in the elements of the A tensors were limited to 1 to 2%. We also considered off-diagonal terms in the g tensor of the order of 0.025, which led to variations between 1 and 7% in the elements of the A tensors.

and Bleaney call the pseudo-nuclear Zeeman effect. [3] Recently Sottini and Groenen [110] revisited the perturbation approach followed by Abragam and Bleaney and showed that the name pseudo-nuclear Zeeman effect does not do justice to its physical nature.

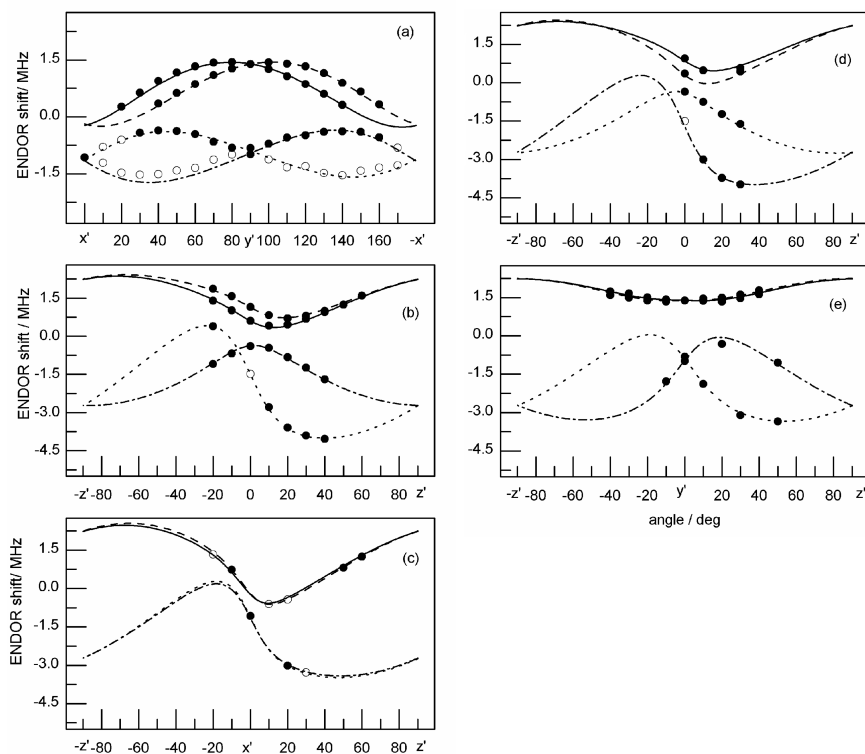


Figure 4.5: The phosphorus ENDOR resonances as a function of the orientation of the magnetic field in the following planes: $x'y'$ (a), -50 degrees from x' in the $x'y'$ plane towards z' (b), $z'x'$ (c), 40 degrees from x' in the $x'y'$ plane towards z' (d) and $z'y'$ (e). The dots represent the data points, the lines are the fits based on Equation 4.5. The ENDOR shift is defined as $\nu_Z - \nu_{ENDOR}$. The open dots represent the points with deviating width and shape that have been omitted in the fitting procedure.

In any case, the above analysis was found superior to the alternative approach of working in the effective spin 1/2 picture. In that case, no assumptions as regards the g tensor are necessary. At W band, the treatment of the Zeeman term as a first order perturbation with respect to the ZFS term in Equation 4.1 leads to energies that still provide an adequate description of the EPR spectra. However, for the interpretation of the ENDOR spectra we need the eigenstates and the effective spin 1/2 treatment was found to introduce appreciable errors in the expectation value $\langle \vec{S} \rangle$. Too low expectation values were found, with deviations up to 40% for some orientations. In spite of this, the directions of the principal axes of the A tensors came out the same in both treatments.

4. A W-band pulsed EPR/ENDOR study of Co(II)S₄ coordination in the Co[(SPh₂)(SPⁱPr₂)N]₂ complex

A_1/h			A_2/h		
0.38	-0.45	-0.71	0.30	0.51	-0.80
-0.45	-2.06	0.02	0.51	-2.05	-0.01
-0.71	0.02	-1.65	-0.80	-0.01	-1.66
A_3/h			A_4/h		
2.49	-1.00	-1.42	2.63	1.16	-1.35
-1.00	1.20	1.19	1.16	1.28	-1.11
-1.42	1.19	1.83	-1.35	-1.11	1.84

Table 4.1: Hyperfine tensors of the four phosphorus nuclei as obtained from the fit of the ENDOR frequencies using Equation 4.5. The hyperfine values are expressed in MHz. The tensors are represented in the reference frame of the g' tensor (x' , y' , z'). The sign of the tensor elements corresponds to the assumption that the ENDOR signals derive from the β manifold.

4.5 Discussion

The coordination of Co²⁺ to sulfur containing ligands in Co(II)S₄ chemical or biological sites is difficult to study by EPR because of the large ZFS of the $S = 3/2$ high-spin configuration. At W band, ESE-detected EPR and ENDOR experiments have been found feasible for a 1% Co^{iPr,Ph}L₂/Zn^{iPr,Ph}L₂ single crystal. The EPR and ENDOR spectra were studied as a function of the orientation of the magnetic field with respect to the crystal. In the ENDOR spectra, signals were identified from phosphorus, nitrogen and hydrogen atoms of the coordinated ligand and they present the possibility of a quantitative analysis of the delocalization of the electron-spin density beyond the Co(II)S₄ core. Interactions between a Co²⁺ site and distant phosphorus atoms have been investigated in the cobalt-substituted zinc finger 3 of transcription factor III A. [79]

In our system we have been able to fully analyze the phosphorus ENDOR data and the complete hyperfine tensors are given in Table 4.1. In order to discuss these results, we first describe the crystal structure of the Co^{iPr,Ph}L₂ complex.

The Co^{iPr,Ph}L₂ complex crystallizes in the C2/c space group with four magnetically indistinguishable molecules in the unit cell. [108] The CoS₄ core has D_{2d} symmetry, but the symmetry of the complex is lower because the two phosphorus atoms in each CoSPNPS ring (Figure 4.1) carry different peripheral groups (ⁱPr and Ph). Only one two-fold rotation axis is left, which is indicated by C'_2 as it is perpendicular to the S₄ axis of the core. The C'_2 axis bisects the exo S–Co–S angles and is parallel to the crystallographic b axis. The complex adopts the so-called “bird-

arrangement". In view of the near equivalence observed for the structures of the analogous CoL_2 and ZnL_2 complexes, we assume that the description of the structure of the $\text{Co}^{\text{iPr,Ph}}\text{L}_2$ complex as derived from the crystal structure also applies to the structure of the complex in the mixed 1% $\text{Co}^{\text{iPr,Ph}}\text{L}_2/\text{Zn}^{\text{iPr,Ph}}\text{L}_2$ crystal.

Recently we have performed a continuous-wave EPR study of $\text{Co}^{\text{iPr,Ph}}\text{L}_2$ at 9, 95 and 275 GHz. [5] At X band, the continuous-wave EPR spectrum of a mixed crystal, similar to the crystal investigated here, shows fully resolved cobalt ($I = 7/2$) hyperfine structure. An orientation study of this hyperfine structure revealed the coincidence of the principal axes of the effective g' tensor and the effective cobalt hyperfine tensor, although this is only enforced by symmetry for one of the axes, the one parallel to the C'_2 axis. The principal axes of the g' tensor follow those of the ZFS tensor because of the negligible contribution of the off-diagonal elements of the g tensor to the g' tensor. Owing to the symmetry of the complex, one of the principal axis of the g tensor must also be parallel to the C'_2 axis, and only one of the off-diagonal terms (g_{xz} , as we will see below) might be non-zero. The principal values of the g' tensor at X band are 1.62, 2.38 and 6.44. [5]

The ESE-detected EPR spectra at W band are consistent with the interpretation of the continuous-wave spectra at X band. The four molecules in the unit cell are magnetically indistinguishable and, for each orientation of the magnetic field with respect to the crystal, a single line is observed. As expected, the principal values of the g' tensor, 1.61, 2.34 and 6.42, slightly differ from the ones obtained at X band. The description in terms of an effective $S = 1/2$ spin is less applicable at W band than at X band, because the intra-doublet splitting (the microwave quantum) is about 10% of the inter-doublet splitting. The limits of such a description at W band are found to concern much more the eigenstates than the eigenvalues. The cobalt hyperfine structure, resolved at X band for all orientations of the magnetic field, is largely anisotropic and biggest for the magnetic field parallel to z' . Only along this direction the cobalt hyperfine structure is resolved in the ESE detected EPR spectra at W band.

For the interaction of the electron spin and a phosphorus nuclear spin $I = 1/2$, the ENDOR spectrum is expected to consist of two lines symmetrically displaced with respect to the phosphorus nuclear Zeeman frequency. The $\text{Co}^{\text{iPr,Ph}}\text{L}_2$ complex contains four phosphorus nuclei and eight lines are expected. For none of the orientations of the magnetic field with respect to the crystal are more than four lines observed in the ENDOR spectrum, and no more than two on either side of the nuclear Zeeman frequency. Moreover, the ENDOR shift of the lines above and below the nuclear Zeeman frequency is not identical. We conclude that the lines derive from the four phosphorus nuclei and that for each nucleus only one ENDOR line shows up, either above or below the nuclear Zeeman frequency. A difference in the intensity of the ENDOR lines on either side of the nuclear Zeeman frequency has been observed before in experiments at large thermal polarization. [111, 112] It is related to relaxation in the spin system. The systematic absence of one of the

4. A W-band pulsed EPR/ENDOR study of Co(II)S₄ coordination in the Co[(SPPH₂)(SPⁱPr₂)N]₂ complex

ENDOR lines in our case deserves further attention. The deviating width and shape of some of the ENDOR lines, like the one to the right in Figure 4.4, most probably results from a slight magnetic inequivalence of the four molecules in the unit cell, which shows up at the ENDOR level (100 kHz).

Each of the phosphorus hyperfine tensors A_1, A_2, A_3, A_4 in Table 4.1 corresponds to one of the phosphorus nuclei in the Co^{iPr,Ph}L₂ complex. The tensor elements of A_1 and A_2 have approximately equal magnitudes, while the $x'y'$ and $y'z'$ elements have opposite sign and the same holds for A_3 and A_4 . We conclude that the A_1 and A_2 tensors belong to two phosphorus atoms that carry the same peripheral group (either ⁱPr or Ph) and are related by a two-fold rotation around y' . The principal y' axis of the g' tensor is consequently parallel to the C'_2 axis of Co^{iPr,Ph}L₂. The same applies to A_3 and A_4 . The fact that the magnitude of the tensor elements is similar, but not identical implies that the symmetry of the complex is only approximately C_2 .

After diagonalization of the A tensors of the four phosphorus nuclei in Table 4.1, we arrive at the principal values, which carry an isotropic and an anisotropic part. The tensors A_1 and A_2 are similar, and the same holds for A_3 and A_4 . In Table 4.2 we present the average diagonalized tensor for both types of phosphorus nuclei, one that belongs to the phosphorus that carry two Ph groups and one that belongs to the phosphorus that carry two ⁱPr groups.

	$A_{x''x''}/h$	$A_{y''y''}/h$	$A_{z''z''}/h$	A_{iso}/h
P _{1,2}	-1.07	-0.72	1.79	-1.13
P _{3,4}	-1.53	-0.99	2.52	1.88

Table 4.2: Hyperfine tensors of the two types of phosphorus nuclei. The principal values of the anisotropic hyperfine tensors and the isotropic hyperfine values are expressed in MHz. The principal axes systems of the hyperfine tensors are indicated by (x'' , y'' , z''). The sign of the tensor elements corresponds to the assumption that the ENDOR signals derive from the β manifold.

To which phosphorus do the hyperfine tensors belong? A significant part of the spin density will be on cobalt. For spin density one on cobalt, at a distance of 0.33 nm from phosphorus, the dipolar contribution to the anisotropic hyperfine tensor of the phosphorus would be -0.8 MHz, -0.8 MHz, 1.6 MHz. The ratio of these principal values amounts to -1, -1, 2. The correspondence of the signs of the dipolar contribution with the signs of the principal values of the anisotropic tensors in Table 4.2 corroborates our assumption that the observed ENDOR lines belong to the nuclear-spin transition in the electron-spin β manifold. Comparison with the tensors in Table 4.2 further shows that the principal values do not quantitatively

adhere to the dipolar ratio. This is not surprising because not only the spin density on cobalt contributes to the anisotropic part of the phosphorus hyperfine tensor. Nevertheless, if we calculate the angle between the direction of the principal z'' axes of the corresponding tensors A_1 and A_2 , we find an angle of 161 degrees. From the crystal structure [108] we calculate an angle of 170 degrees between the vectors connecting the cobalt with the two phosphorus atoms that carry the Ph groups. The near equivalence of these angles leads to the conclusion that the tensors A_1 and A_2 most probably belong to the phosphorus atoms that carry the Ph groups ($P_{1,2}$ in Figure 4.1 and Table 4.2). Similarly, the principal z'' axes corresponding to the tensors A_3 and A_4 make an angle of 128 degrees, and the vectors connecting the cobalt with the two phosphorus atoms that carry the ^1Pr groups an angle of 119 degrees. [108] The tensors A_3 and A_4 most probably belong to the phosphorus atoms that carry the ^1Pr groups ($P_{3,4}$ in Figure 4.1 and Table 4.2). It should be noted that ^{31}P NMR studies of $\text{Co}^{\text{iPr,Ph}}\text{L}_2$ also made it possible to distinguish the two different types of phosphorus atoms. [108]

Finally a remark about the isotropic part of the phosphorus hyperfine tensors. The isotropic hyperfine interaction has different sign for the two types of phosphorus, negative for $P_{1,2}$ and positive for $P_{3,4}$. The small s -spin density is negative on the phosphorus that carry the Ph groups and positive on the phosphorus that carry the ^1Pr groups.

4.6 Conclusion

Pulsed EPR/ENDOR experiments at 95 GHz have been shown feasible for a bidentate high-spin ($S = 3/2$) Co^{2+} complex in which the cobalt is coordinated by four sulfur atoms. From the study of the ESE-detected EPR spectra of a diamagnetically diluted 1% $\text{Co}^{\text{iPr,Ph}}\text{L}_2/\text{Zn}^{\text{iPr,Ph}}\text{L}_2$ crystal as a function of the orientation of the magnetic field with respect to the crystal, the orientation of the principal axes of the effective g' tensor could be determined. This in turn enabled the study of the pulsed ENDOR spectra as a function of the orientation of the magnetic field in this molecule-fixed axes system.

The ENDOR spectra revealed signals from ligand phosphorus nuclei, which were analyzed in detail and complete hyperfine tensors were obtained for all four phosphorus atoms in the complex. On the basis of the anisotropic parts, the tensors could be assigned to the two types of phosphorus present, the phosphorus that carry two Ph groups and the phosphorus that carry two ^1Pr groups. The isotropic hyperfine interactions of the differently substituted phosphorus have opposite sign. The phosphorus hyperfine tensors reveal the asymmetry in the delocalization of the spin density from cobalt over the ligand. This implies that the Co–S bonds are non-equivalent as a result of a subtle difference far away from the $\text{Co(II)}\text{S}_4$ core.

4. A W-band pulsed EPR/ENDOR study of Co(II)S₄ coordination in the Co[(SPh₂)(SⁱPr₂)N]₂ complex

Chapter 5

High-frequency EPR study of the pseudo-tetrahedral high-spin Fe^{2+} complex $\text{Fe}[(\text{SPh})_2\text{N}]_2$

We report continuous-wave (cw) EPR spectra of a powder of the high-spin Fe^{2+} complex $\text{Fe}[(\text{SPh})_2\text{N}]_2$ at 275.7 GHz (J band) and 94.1 GHz (W band). These spectra show that the complex occurs in two different conformations, which have a slightly different electronic structure near the iron ion. At J band also crystals of the complex were studied, which made it possible to assign the signals observed in the powder spectra to the two slightly different iron sites and determine their spin-Hamiltonian parameters with high accuracy.

Guinevere Mathies, Spyros Chatziefthimiou, Dimitrios Maganas, Yiannis Sanakis, Silvia Sottini, Panayotis Kyritsis and Edgar J. J. Groenen, *in preparation*.

5. High-frequency EPR study of the pseudo-tetrahedral high-spin Fe^{2+} complex $\text{Fe}[(\text{SPPh}_2)_2\text{N}]_2$

5.1 Introduction

Pursuit of experimental data on the electronic structure of high-spin Fe^{2+} sites is of great relevance for bioinorganic chemistry. [98, 113] High-spin Fe^{2+} occurs in the active sites of many metalloproteins, but the understanding of their electronic structure is still developing. [8] Electron-paramagnetic-resonance (EPR) spectroscopy is a suitable and sensitive method to investigate the electronic structure of paramagnetic transition-metal sites. However, high-spin Fe^{2+} systems, $S = 2$, tend to be EPR silent at the standard microwave frequency of 9.5 GHz (X band) or, if a spectrum is observed, it is little informative. [114–117]

The degeneracy of the five magnetic sublevels of the $S = 2$ spin system, a non-Kramers system, may be completely lifted at zero field. This zero-field splitting (ZFS) is often much larger than the X-band microwave quantum. Therefore the quantitative study of high-spin Fe^{2+} systems by EPR had to await the technical development of high-frequency/high-field EPR (HF EPR). [118] In recent literature a handful of studies of high-spin Fe^{2+} complexes by HF EPR can be found, [119–125] and one study of a frozen solution of the protein rubredoxin, which contains in the reduced form high-spin Fe^{2+} in its active site. [59]

Here we study the high-spin Fe^{2+} complex $\text{Fe}[(\text{SPPh}_2)_2\text{N}]_2$, abbreviated as $\text{Fe}^{\text{Ph,Ph}}\text{L}_2$, by high-frequency EPR. In this complex two bidentate disulfidoimidodiphosphinato ligands constitute a compressed, approximately tetrahedral sulfur coordination of the iron, see Figure 5.1.

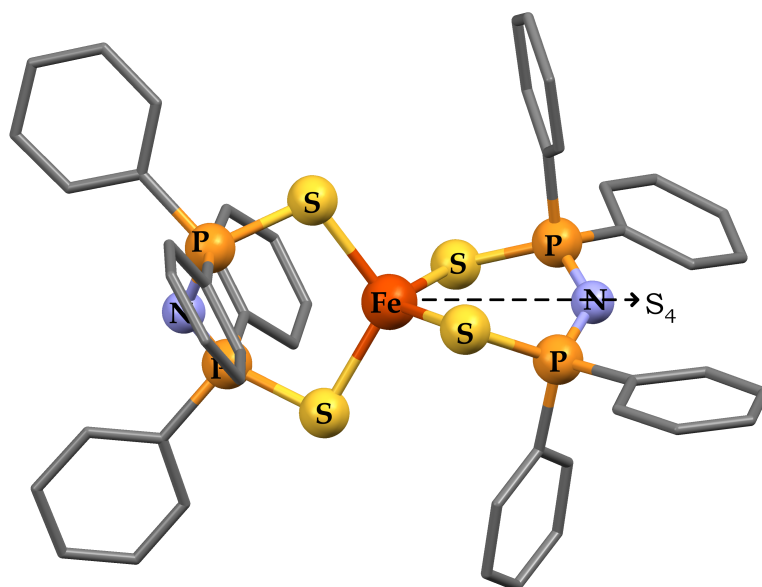


Figure 5.1: The molecular structure of $\text{Fe}[(\text{SPPh}_2)_2\text{N}]_2$.

We report continuous-wave (cw) EPR spectra of $\text{Fe}^{\text{Ph,Ph}}\text{L}_2$ powder at 275.7 GHz (J band) and 94.1 GHz (W band). These spectra show that the complex occurs in two different conformations, which have a slightly different electronic structure near the iron ion. At J band also crystals of the complex were studied, which made it possible to assign the signals observed in the powder spectra to the two slightly different iron sites and determine their spin-Hamiltonian parameters with high accuracy.

5.2 Materials and methods

5.2.1 Sample preparation

$\text{Fe}^{\text{Ph,Ph}}\text{L}_2$ was prepared as described by Davison et al. [126] Grain/crystal size was determined by the ratio $\text{CH}_2\text{-Cl}_2/\text{hexane}$ from which the material was recrystallized, which determined the precipitation speed. The $\text{Fe}^{\text{Ph,Ph}}\text{L}_2$ crystals show variation in color. Some are brownish, others are colorless to the eye. The brownish crystals are suspected to contain a Fe^{3+} species. The quality of the crystals varies. Many, particularly the larger ones, consist of multiple crystals grown together. For the J-band crystal measurements high-quality, colorless crystals were selected. The crystals had a parallelepiped shape of which the length of two edges was similar and the third edge was considerably longer. The size of the crystals studied at J band was estimated to be $0.3 \times 0.08 \times 0.08$ mm. For the J-band experiments a suprasil sample tube of inner diameter 0.15 mm was used (VitroCom Inc.). The effective sample volume, determined by the microwave cavity, is approximately 20 nl. [64] The sample tube was filled with silicon grease to fix the crystal at low temperatures. To align the long edge of the crystal with the sample tube axis a crystal was stuck to a suprasil rod with silicon grease and inserted into the sample tube, which was filled with grease.

5.2.2 EPR experiments

The cw J-band EPR spectra were recorded on an in-house developed spectrometer, [9] using a probe head specialized for operation in cw mode as described in Chapter 2. [64] A single-mode cavity was used for detection of the EPR signal. A sample tube can be inserted from one end of the cavity and rotated by 360 degrees around its axis. The magnetic field is applied perpendicular to this axis. The cw W-band spectra were recorded on a Bruker Elexsys E680 spectrometer using a W-band “ENDOR” probe head with a cylindrical TE_{011} cavity in a CF935W flow cryostat (Oxford Instruments). During the low-temperature experiments the waveguide was heated just outside the cryostat to avoid condensation inside the waveguide. The cw X-band spectra were also recorded on a Bruker Elexsys E680 spectrometer, using a TE_{102} rectangular cavity equipped with an ESR 900 Cryostat (Oxford Instruments).

5. High-frequency EPR study of the pseudo-tetrahedral high-spin Fe^{2+} complex $\text{Fe}[(\text{SPh}_2)_2\text{N}]_2$

5.3 Results

Figure 5.2 shows the cw J-band spectra of a powder of $\text{Fe}^{\text{Ph,Ph}}\text{L}_2$ at 10, 25 and 50 K. The spectra are rich in signals and cover a magnetic field range of 10 T. A group of signals between 0.8 and 3.5 T loses intensity relative to a second group of four signals between 5.5 and 9 T as the temperature increases. As the magnetic field sweep starts from zero the EPR signal decreases, which suggests an absorption of microwaves at zero field, and reaches a minimum approximately at 700 mT at 10 K and approximately at 200 mT at 25 and 50 K. The fine structure, most pronounced in the 10 K spectrum around 2 T, which seems to be noise, reproduces in consecutive scans, but changes if the sample tube is rotated between scans.

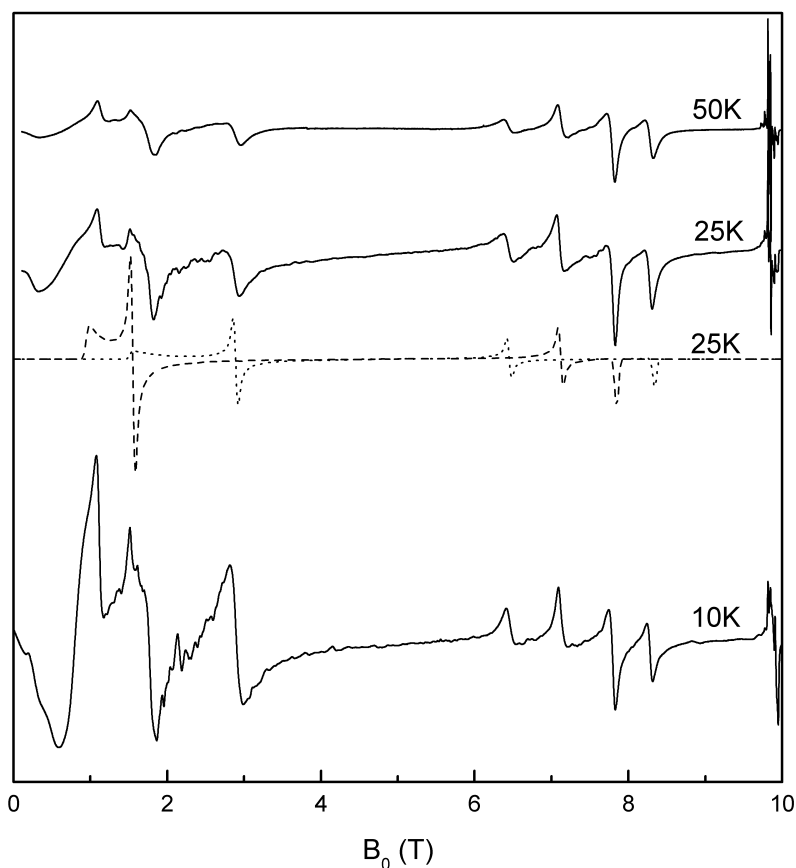


Figure 5.2: J-band powder spectra of $\text{Fe}^{\text{Ph,Ph}}\text{L}_2$ at 10, 25 and 50 K. Solid lines: experimental spectra, dashed line: simulation molecule 1, dotted line: simulation molecule 2. Experimental conditions: microwave frequency 275.7 GHz, microwave power 1 μW , modulation amplitude 3 mT, modulation frequency 1.8 kHz. Around $g = 2$ (9.84 T) signals from a Mn^{2+} impurity are observed.

In Figure 5.3 the J-band spectrum of a crystal of $\text{Fe}^{\text{Ph,Ph}}\text{L}_2$ shows a low-field group of signals and a high-field group of four signals. This crystal was placed in the sample tube such that its long edge was parallel to the axis of the sample tube, around which it can be rotated. The magnetic field is applied perpendicular to this axis of rotation. Figure 5.4 shows the behavior of the high-field signals as the sample is rotated. The four signals belong together two by two, as indicated in Figure 5.4 by the dashed and dotted lines. The dashed lines intersect at an orientation of 0 (and 90) degrees, while the dotted lines intersect at an orientation of 15 (and 105) degrees. Apart from a number of “extra” signals, marked in Figure 5.4, the high-field part of the J-band crystal spectrum is invariant under a rotation by 90 degrees. Spectra recorded on this crystal at 10 and 5 K showed no significant changes in the relative intensities of the four high-field signals, but the “extra” signals became relatively strong at 5 K.

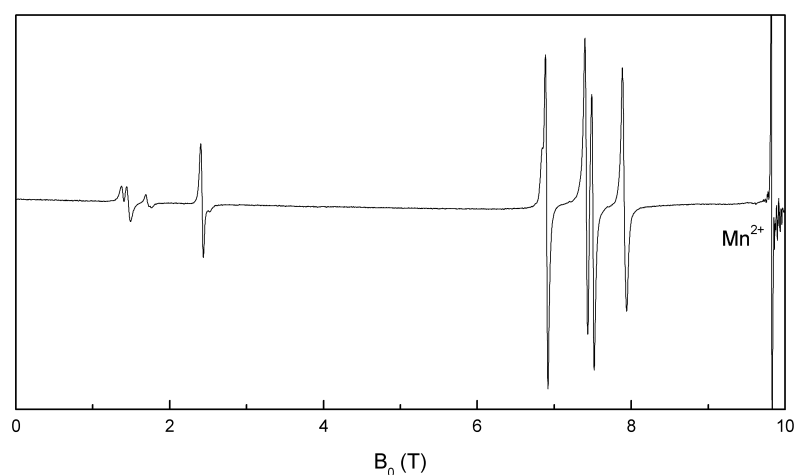


Figure 5.3: J-band spectrum at 25 K of a crystal of $\text{Fe}^{\text{Ph,Ph}}\text{L}_2$ aligned such that B_0 is approximately perpendicular to the long edge of the crystal. The relative orientation of the crystal in the plane perpendicular to the long crystal edge is 90 degrees, see Figure 5.4. Around $g = 2$ (9.84 T) signals from a Mn^{2+} impurity are observed.

Crystal spectra were also recorded at J band for two other crystals, one oriented arbitrarily and one aligned with its long edge perpendicular to the axis of the sample tube. Spectra of both crystals showed the low-field and high-field groups of signals, and the dependence on the orientation of the crystal with respect to the applied magnetic field in line with the spectra shown in Figure 5.3 and Figure 5.4. For the orientation of the long edge of the crystal parallel to the applied magnetic field the latter crystal showed a signal at 250 mT.

Spectra recorded at W band in cw mode for $\text{Fe}^{\text{Ph,Ph}}\text{L}_2$ powder show three signals, at 0.9, 1.4 and 2.9 T, see Figure 5.5. Also a very broad signal is observed, stretching

5. High-frequency EPR study of the pseudo-tetrahedral high-spin Fe^{2+} complex $\text{Fe}[(\text{SPh}_2)_2\text{N}]_2$

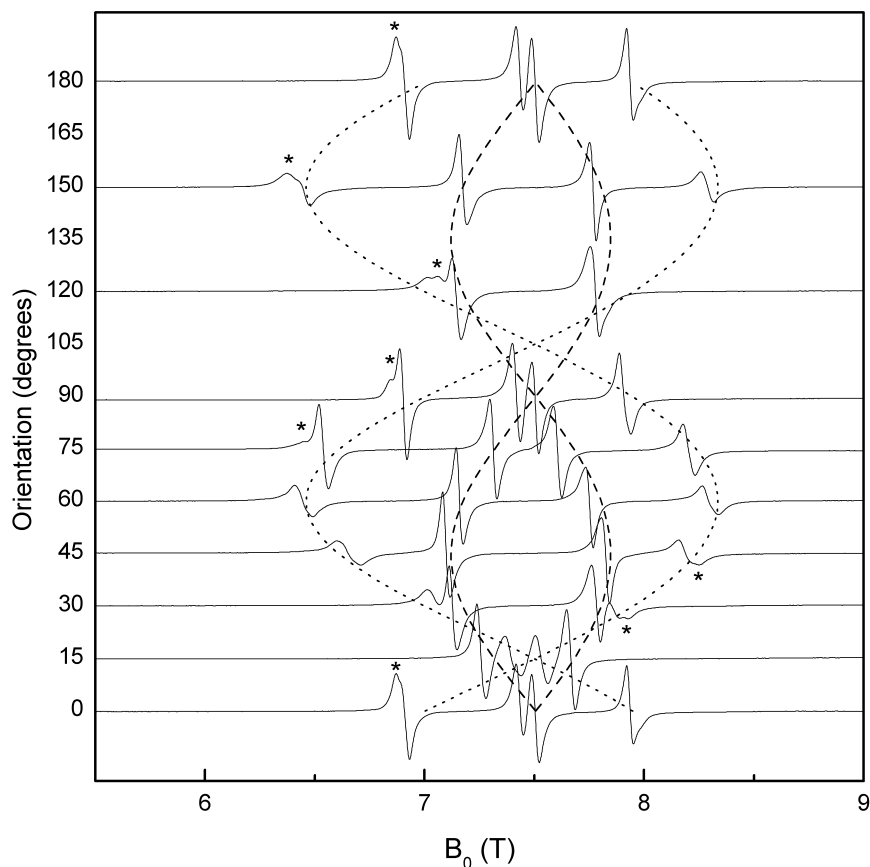


Figure 5.4: High-field region of J-band spectra at 25 K of a $\text{Fe}^{\text{Ph,Ph}}\text{L}_2$ crystal aligned such that B_0 is approximately perpendicular to the long edge of the crystal. The angles shown in the graph represent the relative orientation around the long crystal edge, the orientation of 0 degrees is chosen arbitrarily. The dashed and dotted lines show the behavior of the resonance fields calculated using EasySpin for molecule 1 and molecule 2, respectively, under the assumption that the z -axis of the spin system is perfectly perpendicular to B_0 . The “extra” signals are marked with a \star .

from approximately 0.5 to 3.5 T, of which the exact shape is difficult to resolve due to baseline drift during the scan, and a sharp peak at 1.6 T. All signals become stronger if the temperature is lowered from 20 to 12.5 K.

Figure 5.6 shows X-band spectra of a powder of $\text{Fe}^{\text{Ph,Ph}}\text{L}_2$. A broad peak is observed, which shifts to lower field and broadens as the temperature increases. The maximum of the peak is observed at 67, 65.6, 62.2, 53.4 mT at 5, 20, 40, 60 K respectively.

J-band spectra were also measured on a diamagnetically diluted powder containing 5% $\text{Fe}^{\text{Ph,Ph}}\text{L}_2$ and 95% $\text{Zn}^{\text{Ph,Ph}}\text{L}_2$ and on a mixed crystal containing 1% $\text{Fe}^{\text{Ph,Ph}}\text{L}_2$

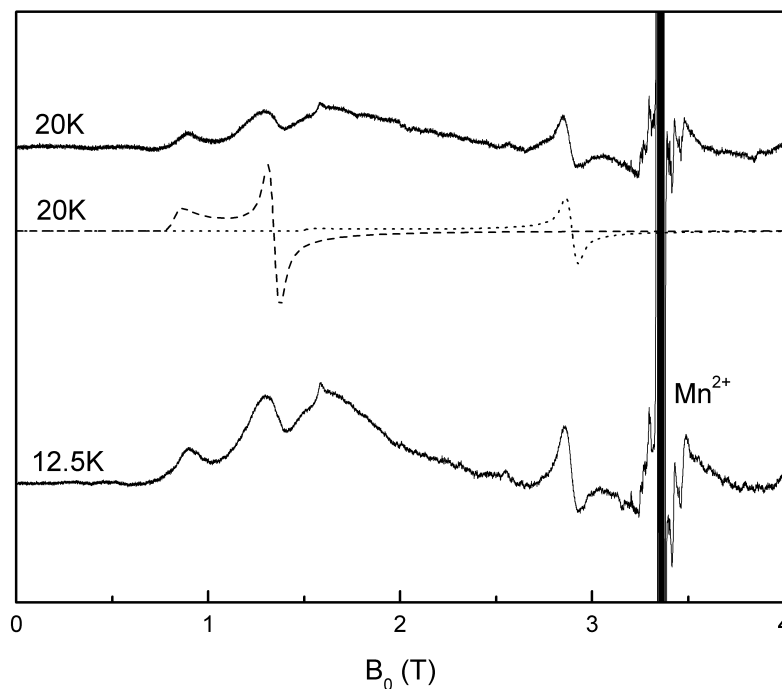


Figure 5.5: W-band powder spectra of $\text{Fe}^{\text{Ph,Ph}}\text{L}_2$ at 12.5 and 20 K. Solid lines: experimental spectra, dashed line: simulation molecule 1, dotted line: simulation molecule 2. Experimental conditions: microwave frequency 94.1 GHz, microwave power 0.02 mW, modulation amplitude 1.5 mT, modulation frequency 90 kHz. A strong Mn^{2+} impurity is observed at $g = 2$ (3.36 T). A baseline was subtracted.

and 99% $\text{Zn}^{\text{Ph,Ph}}\text{L}_2$. These spectra were in agreement with the 100% $\text{Fe}^{\text{Ph,Ph}}\text{L}_2$ spectra, and were of low intensity, according to the diamagnetic dilution. Attempts to detect an electron spin echo of 100% $\text{Fe}^{\text{Ph,Ph}}\text{L}_2$ powder at J band and W band were not successful, not even at 1.7 K.

5.4 Analysis

The EPR spectra of high-spin Fe^{2+} , $S = 2$, are interpreted using the following spin Hamiltonian. [3]

$$H = \mu_B \vec{B}_0 \cdot \vec{g} \cdot \vec{S} + \vec{S} \cdot \vec{D} \cdot \vec{S} \quad (5.1)$$

The g tensor in the first term describes the anisotropy of the Zeeman interaction. The second term is a field independent fine-structure term, the zero-field splitting (ZFS). The ZFS tensor, \vec{D} , is symmetric, can be taken traceless, and is characterized

5. High-frequency EPR study of the pseudo-tetrahedral high-spin Fe²⁺ complex Fe[(SPh₂)₂N]₂

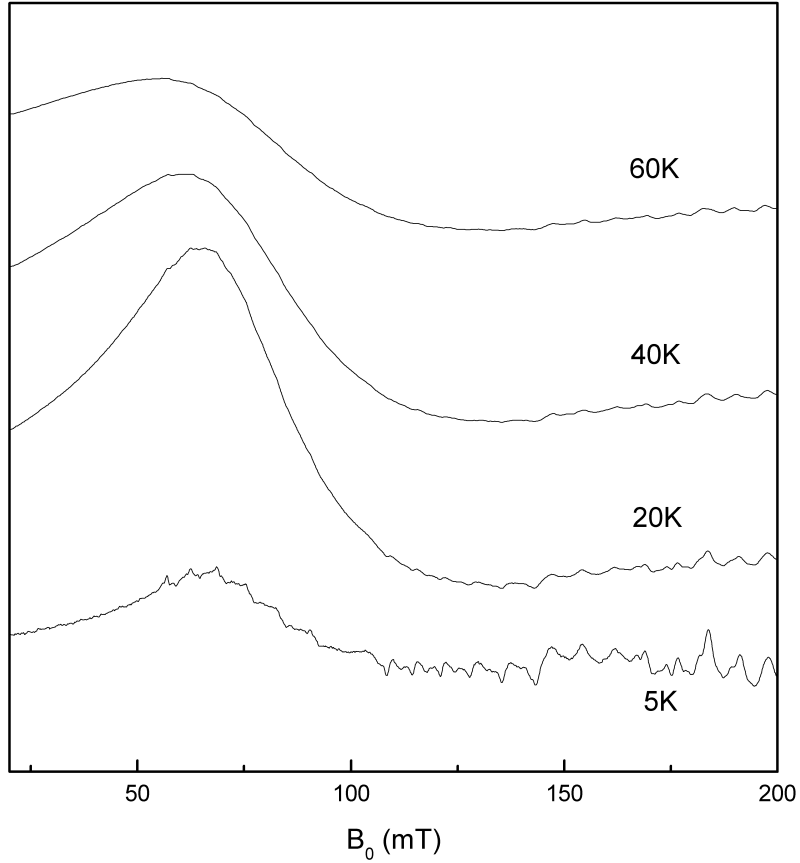


Figure 5.6: X-band powder spectra of Fe^{Ph,Ph}L₂ at 5, 20, 40 and 60 K. Experimental conditions: microwave frequency 9.488 GHz, microwave power 100 mW, modulation amplitude 0.5 mT, modulation frequency 100 kHz. The wiggles showing up in the 5 K spectrum most prominently are forbidden transitions of a Mn²⁺ impurity.

by two parameters, D and E .

$$D = 3/2D_z, E = 1/2(D_x - D_y) \quad (5.2)$$

The rhombicity of \vec{D} is given by the ratio $\lambda = E/D$. The principal axes are chosen such that $|D_z| > |D_y| > |D_x|$ and thus $0 < \lambda < 1/3$.

In zero field the eigenfunctions and eigenvalues of this spin Hamiltonian are [116]

$$\begin{aligned}
 |2^{s'}\rangle &= \sqrt{\frac{1}{2} \left(1 + \frac{D}{\sqrt{D^2 + 3E^2}} \right)} \frac{|+2\rangle + |-2\rangle}{\sqrt{2}} \\
 &+ \sqrt{\frac{1}{2} \left(1 - \frac{D}{\sqrt{D^2 + 3E^2}} \right)} |0\rangle \\
 |2^a\rangle &= \frac{1}{\sqrt{2}} (|+2\rangle - |-2\rangle) \\
 |1^s\rangle &= \frac{1}{\sqrt{2}} (|+1\rangle + |-1\rangle) \\
 |1^a\rangle &= \frac{1}{\sqrt{2}} (|+1\rangle - |-1\rangle) \\
 |0'\rangle &= \sqrt{\frac{1}{2} \left(1 - \frac{D}{\sqrt{D^2 + 3E^2}} \right)} \frac{|+2\rangle + |-2\rangle}{\sqrt{2}} \\
 &+ \sqrt{\frac{1}{2} \left(1 + \frac{D}{\sqrt{D^2 + 3E^2}} \right)} |0\rangle
 \end{aligned} \tag{5.3}$$

$$\begin{aligned}
 E_{2^{s'}} &= 2\sqrt{D^2 + 3E^2} \\
 E_{2^a} &= 2D \\
 E_{1^s} &= -D + 3E \\
 E_{1^a} &= -D - 3E \\
 E_{0'} &= -2\sqrt{D^2 + 3E^2}
 \end{aligned} \tag{5.4}$$

The size of $|D|$ is typically between 150 and 600 GHz. If the ZFS tensor is axial, $\lambda = 0$, the quintet splits into two doublets, $|2^{s'}\rangle$, $|2^a\rangle$ and $|1^s\rangle$, $|1^a\rangle$, and a singlet, $|0'\rangle$. A non-zero value of λ lifts the degeneracy completely and introduces an $m_s = 0$ component in the $|2^{s'}\rangle$ state and $m_s = \pm 2$ components in the $|0'\rangle$ state, as shown by the accent in the names of the states. For $D > 0$ the state $|0'\rangle$ is the lowest in energy.

Figure 5.7 shows the behavior of the five magnetic sublevels as a function of B_0 applied along the principal directions x , y and z for a positive D of 266 GHz and $\lambda = 0.052$, assuming that the principal axes of the D and g tensor are collinear. These ZFS parameters describe one of the two molecules present in the $\text{Fe}^{\text{Ph,Ph}}\text{L}_2$ samples we investigated, as will become clear in this section. J-band transitions are shown in Figure 5.7 by vertical lines. From the temperature dependence of their intensity we conclude that the low-field signals observed in the J-band spectra arise from transitions from the ground state $|0'\rangle$ to the states $|1^s\rangle$, $|1^a\rangle$, while the high-field

5. High-frequency EPR study of the pseudo-tetrahedral high-spin Fe^{2+} complex $\text{Fe}[(\text{SPPh}_2)_2\text{N}]_2$

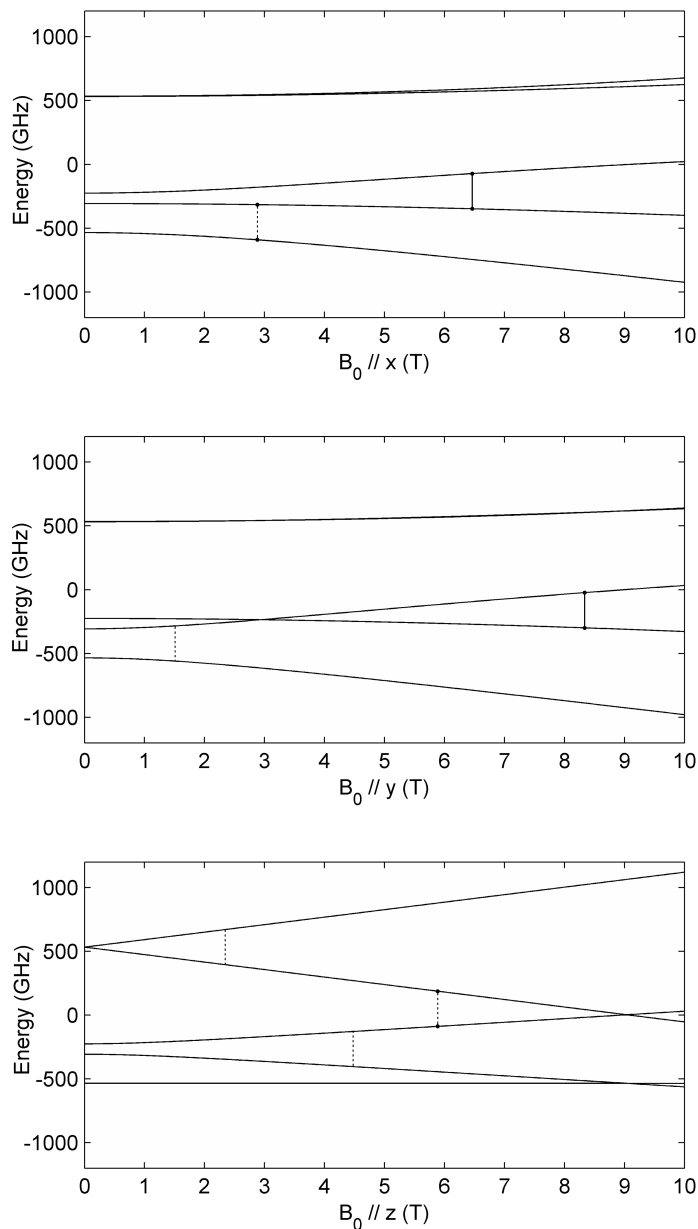


Figure 5.7: The dependence of the energy of the five magnetic sublevels of the $S = 2$ spin system on the magnitude of the magnetic field applied along the x , y and z direction for molecule 2. The vertical lines show 275.7 GHz resonances. The dashed resonances have a low transition probability.

signals arise from transitions between the states $|1^s\rangle$ and $|1^a\rangle$. We will start with the interpretation of the high-field signals.

At high magnetic fields the states $|1^s\rangle$ and $|1^a\rangle$ start to behave almost as a doublet. The powder spectrum of an anisotropically split doublet reflects the principal values of the g tensor. In this case a 275.7 GHz transition within the “ $|1^s\rangle$, $|1^a\rangle$ doublet” is almost forbidden if B_0 is parallel to the z -axis of the system and the powder spectrum is expected to show only the transitions drawn in the energy level plots for $B_0 \parallel x$ at 6.4 T and $B_0 \parallel y$ at 8.3 T. However, the J-band spectra of $\text{Fe}^{\text{Ph,Ph}}\text{L}_2$ show four signals in the range 5.5 – 9 T, not two. There are no signs of an exchange interaction between the iron sites, which could additionally split the energy levels, since the spectra on the diamagnetically diluted material match the 100% $\text{Fe}^{\text{Ph,Ph}}\text{L}_2$ spectra. This suggests that there are two $\text{Fe}^{\text{Ph,Ph}}\text{L}_2$ molecules with slightly different spin-Hamiltonian parameters contributing to the powder spectra.

The crystal spectra recorded at J band help to separate the signals contributing to the powder spectra. The behavior of the high-field signals as the crystal is rotated around an axis parallel to its long edge and perpendicular to B_0 is shown in Figure 5.4. Clearly the inner signals, see the dashed lines in Figure 5.4, and the outer signals, see the dotted lines, belong together. The extreme resonance fields of the two outer signals, as in the spectra of relative orientation 60 and 150 degrees, correspond to the two outer high-field signals in the powder spectrum shown in Figure 5.2. Thus, the long edge of the crystal must be parallel to the z -axis of the spin system, of which the behavior of the magnetic sublevels is plotted in Figure 5.7. Rotation around the axis of the sample tube corresponds to a rotation in the x, y -plane. The inner signals arise from what we call molecule 1 and the outer signals arise from molecule 2. The x, y -axes of molecule 1 are rotated around the common z -axis by approximately 15 degrees with respect to the x, y -axes of molecule 2.

Each crystal spectrum in Figure 5.4 shows four high-field signals, which is remarkable, since two signals, one from each molecule, are expected. Also, a rotation by 90 degrees returns the same spectrum. This can only be explained if both molecules occupy two magnetically distinguishable sites, which are rotated with respect to each other by 90 degrees around the z -axis.

To determine the spin-Hamiltonian parameters that describe the electronic structure of the iron sites of the two molecules, the experimental J-band spectra were compared to spectra calculated by numerical diagonalization of the spin-Hamiltonian using EasySpin. [6] Starting values for the ZFS parameters D and E were determined from the J-band powder spectra, using the information we obtained from the crystal spectra, namely that the two inner high-field signals arise from molecule 1 and the two outer high-field signals arise from molecule 2. These two parameter sets would give rise to W-band transitions between the states $|1^s\rangle$ and $|1^a\rangle$. The exact resonance fields of these transitions are very sensitive to the value of E and therefore the signals observed at 0.9, 1.4 and 2.9 T in the W-band powder spectra were used to establish the value of E for both parameter sets. Further fine tuning was performed from the J-band powder spectra, which are very sensitive to D and the principal values of the g tensor.

5. High-frequency EPR study of the pseudo-tetrahedral high-spin Fe²⁺ complex Fe[(SPPPh₂)₂N]₂

The spin-Hamiltonian parameters that describe the iron sites of the two molecules best are

- (1) $D = 275$ GHz, $\lambda = 0.021$
 $g_x = 2.11$, $g_y = 2.14$, $g_z = 2.1$
- (2) $D = 266$ GHz, $\lambda = 0.052$
 $g_x = 2.10$, $g_y = 2.12$, $g_z = 2.1$

Powder spectra calculated with these parameters are shown in Figure 5.2 and Figure 5.5, taking into account an isotropic line width of 50 mT. In Figure 5.4 the calculated behavior of the high-field resonances in the x, y -plane is shown for both parameter sets. From the dependence of the J- and W-band resonances on a change in the parameters, as calculated using EasySpin, we estimate the uncertainties in the spin-Hamiltonian parameters: ± 2 GHz for D , ± 0.002 for λ , ± 0.01 for g_x, g_y , and ± 0.05 for g_z .

The X-band Fe^{Ph,Ph}L₂ powder spectra show a peak that shifts to lower field as the temperature is increased, starting at 67 mT at 5 K. This resonance is incompatible with the parameter sets 1 and 2. In an X-band spectrum molecule 2 is expected to show a weak positive peak at 90 mT resulting from a transition between the states $|2^{s'}\rangle$ and $|2^a\rangle$. Molecule 1 has an almost axial ZFS tensor, which makes a transition between $|2^{s'}\rangle$ and $|2^a\rangle$ forbidden, and is not expected to give any signal at X-band. We conclude that the observed X-band spectra do not arise from molecules 1 and 2, which gave rise to the dominant features in the J- and W-band spectra. Moreover, the two parameter sets do not cover the microwave absorption at zero field in the J-band powder spectrum and the broad signal between 0.5 and 3.5 T and the sharp peak at 1.6 T in the W-band powder spectra. In the crystal spectra shown in Figure 5.4 we observed “extra” resonances and in the J-band spectrum of the crystal aligned with its long edge parallel to B_0 we observed a signal at 250 mT. These observations point to the presence of a third component with a conformation that is not well defined in the powder. For this component the spin-Hamiltonian parameters are distinctly different from those for molecules 1 and 2, and we estimate $D \approx 210$ GHz and $\lambda \approx 0.1$.

5.5 Discussion

The low-field and high-field groups of signals observed in the J-band spectra of Fe^{Ph,Ph}L₂ powder, see Figure 5.2, and also the signals observed in the W-band powder spectra at 0.9, 1.4, 2.9 T, see Figure 5.5, can be understood with the parameter sets 1 and 2. The signals observed in the crystal spectra at J band and their dependence on the relative orientation of B_0 are covered, see Figure 5.4. Small deviations in the calculated resonance fields and, for some orientations, small, unexpected splittings

of the resonances are observed, because we did not attempt to align the principal x and y axes of the spin system exactly with B_0 .

The resonance fields of a J-band spectrum of a typical high-spin Fe^{2+} system are sensitive to a small change in the spin-Hamiltonian parameters, as is clear from the error estimates in these parameters. For our system the W-band resonances were sensitive to a change in E , but rather insensitive to a change in the other parameters, which made it possible to use these spectra as a starting point in the fine tuning of the parameters. The spectra of the crystal were necessary to distinguish between the two components present in the powder spectra.

The shapes of the resonances are not as well reproduced by the simulations as the resonance fields. For instance, the line width of the low-field signals in the J-band powder spectra can not be properly reproduced. More importantly, the shape of the four high-field signals in the J-band powder spectra is not properly calculated. In fact, for unknown reasons, already in the simulations of the crystal spectra the intensity of the high-field transitions, which arise if B_0 is parallel, or nearly parallel, to the y -axis, is underestimated. This mismatch between experiment and simulation deserves further attention.

The signals in the experimental spectra that are not covered by the parameter sets 1 and 2 arise from a third component, which is distinctly different from molecule 1 and 2. The width of the zero-field resonance in the J-band powder spectra and the extremely broad peak in the W-band powder spectra suggest that there is a distribution of conformations this component can take up in the powder. The presence of such a distribution can explain the shift of the positive peak in the X-band spectra to lower field as the temperature is increased. As the values of D and E change, both the resonance field of the transition between the states $|2^{s'}\rangle$ and $|2^a\rangle$ and the temperature at which its intensity is highest shift.

Figure 5.1 shows the structure of $\text{Fe}^{\text{Ph,Ph}}\text{L}_2$ as determined by X-ray diffraction on a crystal at room temperature (S. Chatziefthimiou, private communication). The FeS_4 core assumes an approximately compressed tetrahedral geometry (two larger angles, 115° , and four smaller ones, 107°). [95] The bidentate $(\text{SPPH}_2)_2\text{N}$ ligands form two twisted rings with the iron atom. The complex as a whole has approximately S_4 symmetry.

The complex $\text{Fe}^{\text{Ph,Ph}}\text{L}_2$ crystallizes in the P_{-1} space group. The edges of the unit cell are 14.364(7), 13.823(6) and 13.337(6) Å, the angles α , β and γ are 110.203(16), 114.032(17) and 82.425(13) degrees, respectively. The unit cell contains two molecules, which are connected by an inversion center and therefore can not be distinguished by EPR. The J-band and W-band EPR spectra of $\text{Fe}^{\text{Ph,Ph}}\text{L}_2$ powder, however, can only be explained by, at least, two sets of spin-Hamiltonian parameters, which undoubtedly arise from, at least, two molecules, which differ in structure. Moreover, in the crystal these two molecules are found to occur at two magnetically distinguishable sites, which are rotated with respect to each other by 90 degrees around the z -axis. Thus, the EPR spectra of $\text{Fe}^{\text{Ph,Ph}}\text{L}_2$ are incompatible

5. High-frequency EPR study of the pseudo-tetrahedral high-spin Fe^{2+} complex $\text{Fe}[(\text{SPh})_2\text{N}]_2$

with the information obtained on the crystal structure by X-ray diffraction.

X-ray diffraction on a crystal of the analogous $\text{Co}^{\text{Ph,Ph}}\text{L}_2$ complex revealed a unit cell, space group P_{-1} , that contains in total four molecules. [127] Molecule 1a and 2a are crystallographically independent and are connected to molecule 1b and 2b by an inversion center. Two molecules with different spin-Hamiltonian parameters are thus expected to be observed by EPR spectroscopy. However, only one set of spin-Hamiltonian parameters was observed experimentally. [5] X-ray diffraction on crystals of the analogous $\text{Zn}^{\text{Ph,Ph}}\text{L}_2$ complex revealed two crystal structures, i.e. two different unit cells: one unit cell similar to the unit cell described above for $\text{Fe}^{\text{Ph,Ph}}\text{L}_2$ and another unit cell similar to the unit cell described above for $\text{Co}^{\text{Ph,Ph}}\text{L}_2$ (S. Kyritsis, private communication).

To assure that the unit cell of the crystal studied by J-band EPR is the unit cell described above for $\text{Fe}^{\text{Ph,Ph}}\text{L}_2$ and to exclude that the crystal we studied is a twin, X-ray diffraction was performed, at room temperature, on one of the crystals we studied at J band. This crystal was found to be a single crystal and, moreover, the unit cell is indeed the unit cell described above for $\text{Fe}^{\text{Ph,Ph}}\text{L}_2$. Thus, a remarkable incompatibility between the X-ray diffraction data and the EPR data on this material stands. Possibly the temperature at which the data are acquired plays a role: room temperature for X-ray diffraction versus 50 K or less for the EPR spectroscopy. Small temperature dependent variations in structure for high-spin Fe^{2+} complexes have been observed by others. [124, 125] We are currently investigating this possibility.

5.6 Conclusion

While X-band EPR spectra of high-spin Fe^{2+} systems are notoriously poor in information, the W-band and particularly the J-band EPR spectra of $\text{Fe}^{\text{Ph,Ph}}\text{L}_2$ are very rich and sensitive to small changes in the electronic structure of the iron sites. The combination of J-band and W-band EPR on this complex both in the form of a powder and of a crystal made it possible to determine with high accuracy the spin-Hamiltonian parameters of both conformations in which the complex occurs.

Chapter 6

The two Fe^{3+} binding sites in human serum transferrin distinguished by high-frequency EPR

Continuous-wave electron-paramagnetic-resonance (EPR) spectra at 275.7 GHz of human serum transferrin allow to distinguish the signals of the high-spin Fe^{3+} ions bound by the two homologous lobes of the protein. This observation is confirmed by the 275.7 GHz spectra of two authentic monoferric human serum transferrins in which the iron binding by either the N-lobe or the C-lobe has been disabled by a site-directed mutation. The spectra of the monoferric mutants as well as the wild-type spectra are well reproduced by simulations and quantitatively analyzed in terms of their spin-Hamiltonian parameters.

Guinevere Mathies, Ashley N. Steere, N. Dennis Chasteen, Anne B. Mason and Edgar J. J. Groenen, *in preparation*.

6. The two Fe^{3+} binding sites in human serum transferrin distinguished by high-frequency EPR

6.1 Introduction

The transferrin family of proteins plays a central role in the iron metabolism of vertebrates, and some invertebrates. [16] Human serum transferrin (hTF) transports iron to cells and assures that no free iron ions are present in the blood. The protein consists of two homologous lobes, termed the N- and C-lobe, each capable of binding strongly (binding constant in excess of 10^{20}) and reversibly an Fe^{3+} ion. Each lobe is comprised of two domains that open and close with a hinge motion. The iron is bound deeply in this cleft in a distorted octahedral coordination. Four ligands to the iron are provided by the conserved amino acid residues aspartic acid, histidine and two tyrosines. The two other ligands are constituted by a bound anion, the synergistic anion, which is naturally carbonate, CO_3^{2-} .

All modern, bilobal transferrins are thought to have resulted from the same early gene duplication of an ancestral, monolobal transferrin, [128] for which a candidate has been found in the ascidian *Ciona intestinalis*. [129] Evidence exists of differences in the iron-binding properties between the N- and C-lobe and of cooperativity between the lobes, [130–136] but no consensus in literature exists on what is the major driving force behind the evolution of bilobal transferrins.

Electron-paramagnetic-resonance (EPR) spectroscopy is a suitable and sensitive technique to investigate the electronic structure of paramagnetic transition-metal sites. The Fe^{3+} bound to transferrin is in a high-spin state with a spin angular momentum of $S = 5/2$. The first X-band (9.5 GHz) EPR spectrum of hTF was reported as early as 1963. [137] Since then X-band EPR spectra have been reported of other members of the transferrin family of proteins, [138–141] of transferrin in different environments, [142, 143], bound to the transferrin receptor, [133] or containing a synergistic anion other than carbonate. [144, 145] Moreover, spectra have been recorded at S-band (2.73 GHz), Q-band (34.05 GHz), W-band (94.1 GHz) and even at 285 GHz. [44, 55, 146] However, all of these spectra have withstood complete understanding, even if two or more components were assumed to contribute to the spectra. [86, 146]

Monoferric hTFs, which have iron bound only by the C-lobe or by the N-lobe, can be obtained by adding iron to apo-hTF in the form of ferric nitrilotriacetate (C-lobe) or ferric oxalate (N-lobe). [131, 147] Also, isolated recombinant C-lobe or N-lobe has been prepared, [133, 143] which made it possible to study the effects of site-directed mutations on the iron-binding through spectroscopic techniques. [148–151] The X-band EPR spectra acquired on the monoferric forms of transferrin have the same characteristics as the X-band spectra of the biferric forms. Subtle differences are observed between the N- and C-lobe, but the two lobes cannot be distinguished in the biferric spectra, nor can the differences be interpreted. The lack of an interpretation of the EPR spectra of transferrin constitutes a considerable barrier in the study of the iron binding by transferrin.

The higher the microwave frequency used, the more sensitive the EPR spectrum

of high-spin Fe^{3+} is to small variations in the electronic structure. The last decades have shown a strong increase in the possibilities of EPR at higher microwave frequencies. However, it remained a challenge to achieve the sensitivity to record spectra of frozen solutions of proteins that contain a transition-metal site in a high-spin state, like transferrin. [44, 146] The concentration and available amount of the protein are usually limited, and the spectra are hard to detect, because they cover large field ranges and the observed EPR signals are broad. Recently we have demonstrated that, using a single-mode cavity, it is possible to record high-quality EPR spectra in continuous-wave (cw) mode at 275.7 GHz (J band) of millimolar frozen solutions of the protein rubredoxin, whose active site in the oxidized state contains high-spin Fe^{3+} , see Chapter 2 of this thesis. [64]

Here we report the high-quality cw J-band spectra of hTF. In these spectra the signals due to the two iron-binding sites of hTF are clearly resolved. This observation is confirmed by the cw J-band spectra of two monoferric hTFs in which the iron binding by either the N-lobe or the C-lobe has been disabled by a site-directed mutation. [152] The spectra of the iron bound in the N- and C-lobe are well reproduced using the EPR simulation package EasySpin, [6] taking into account the effect of large conformational strain, and are quantitatively analyzed in terms of their spin-Hamiltonian parameters.

6.2 Materials and methods

Human serum transferrin (hTF) was expressed in baby hamster kidney cells as described in reference 152 and the references therein. The recombinant hTF is non-glycosylated and contains an N-terminal hexa-histidine tag. It is functionally indistinguishable from hTF isolated from serum and containing two Asn-linked glycosylation sites. Monoferric hTF was realized by disabling one of the binding sites by local mutations: monoferric C (Fe_C): N-His Y95F/Y188F hTF-NG, and monoferric N (Fe_N): N-His Y426F/Y517F hTF-NG. The proteins were kept in 100 mM HEPES buffer at pH 7.4.

The cw J-band EPR spectra were recorded on an in-house developed spectrometer, [9] using a probe head specialized for operation in cw mode as described in Chapter 2. [64] The effective sample volume, limited by the microwave cavity, is approximately 20 nl.

6.3 Results

The two upper spectra in Figure 6.1 are the cw J-band EPR spectra of frozen solutions of two hTF mutants, in which either only the C-lobe (Fe_C) or only the N-lobe (Fe_N) is able to bind iron. The Fe_C spectrum shows a broad, positive EPR signal at 8.68 T, and another, less broad, positive signal at 9.24 T, which occurs roughly

6. The two Fe³⁺ binding sites in human serum transferrin distinguished by high-frequency EPR

halfway between the 8.68 T signal and the signals around $g = 2$ (at 9.838 T). The spectrum also shows a broad, negative signal at 11.11 T, and another, less broad, negative signal at 10.48 T, which again occurs roughly halfway between the 11.11 T signal and the signals around $g = 2$. The same pattern is found in the Fe_N spectrum, with positive signals at 8.47 and 9.12 T and negative signals at 10.66 and around 11.5 T.

The lowest spectrum in Figure 6.1 is the cw J-band EPR spectrum of a frozen solution of wild-type hTF, which has an Fe³⁺ ion bound in both lobes. The Fe₂ spectrum clearly shows both the two positive signals observed in the Fe_N spectrum and the two positive signals observed in the Fe_C spectrum. Both negative signals of the Fe_C spectrum and the negative signal observed at 10.66 T in the Fe_N spectrum are present in the Fe₂ spectrum. The shallow 11.5 T signal in the Fe_N spectrum cannot be detected with certainty in the Fe₂ spectrum.

Figure 6.2 shows the $g = 2$ region of the Fe_N, Fe_C and Fe₂ hTF spectra in detail. The positive signals below $g = 2$ and negative signals above $g = 2$ form a complex pattern, which is of much stronger intensity in the Fe_C spectrum than in the Fe_N spectrum. The Fe₂ hTF spectrum is dominated by the signals that also show up in the Fe_C spectrum, but a contribution from the Fe_N spectrum is clear from the weak signals at 9.779 T and around 9.930 T, and a change in shape of the central signal around 9.820 T compared to the Fe_C spectrum.

Apart from the signals already discussed, all spectra in Figure 6.1 show a positive signal just below the $g = 2$ region. The shape of this signal could not be accurately determined, because it is distorted by a negative signal due to an unknown impurity at 9.6 T.

6.4 Analysis

The EPR spectra of high-spin Fe³⁺, $S = 5/2$, are interpreted using the following spin Hamiltonian [3]

$$H = \mu_B \vec{B}_0 \cdot \vec{g} \cdot \vec{S} + \vec{S} \cdot \vec{D} \cdot \vec{S} \quad (6.1)$$

The first term describes the electron Zeeman interaction. The g tensor gives the anisotropy of the Zeeman splitting, which is small for high-spin Fe³⁺. The second term describes the zero-field splitting (ZFS) of the six magnetic sublevels into three Kramers doublets, $|m_s \pm 1/2\rangle$, $|\pm 3/2\rangle$, and $|\pm 5/2\rangle$. The ZFS tensor, \vec{D} , is symmetric, can be taken traceless, and is characterized by two parameters, D and E .

$$D = 3/2D_z, \quad E = 1/2(D_x - D_y) \quad (6.2)$$

The rhombicity of \vec{D} is given by the ratio $\lambda = E/D$. The principal axes are chosen such that $|D_z| > |D_y| > |D_x|$ and $0 < \lambda < 1/3$.

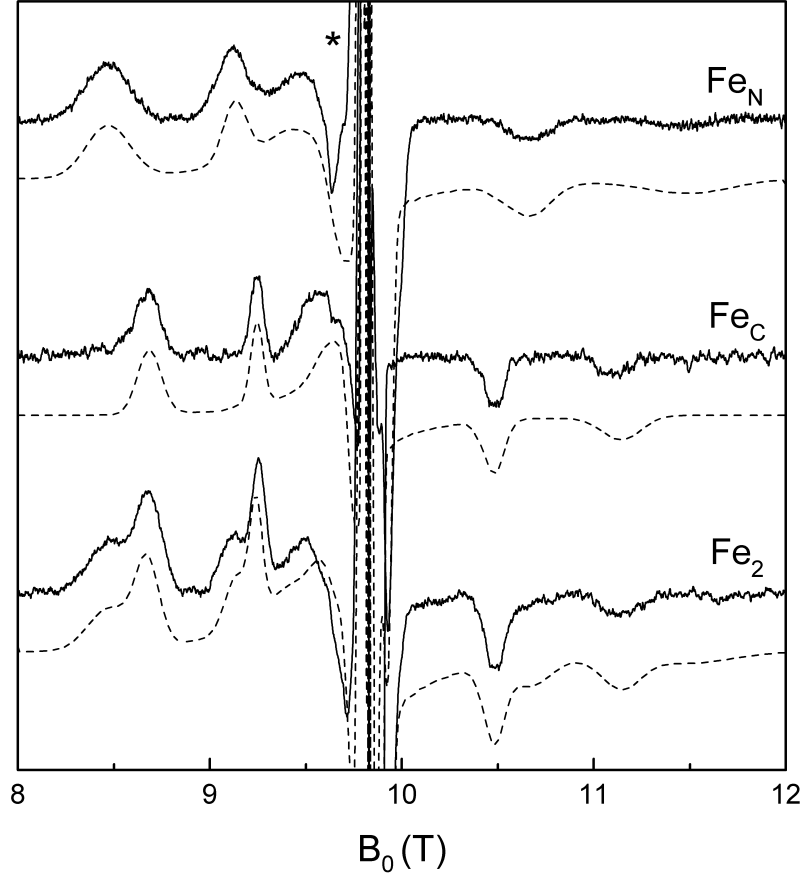


Figure 6.1: J-band cw EPR spectra of 1 mM frozen solutions of Fe_N , Fe_C and Fe_2 human serum transferrin at 10 K. Experimental conditions: modulation amplitude: 3 mT, microwave power: 1 μW , microwave frequency: 275.7 GHz. Solid lines: experimental spectra, dashed lines: spectra calculated using EasySpin and the spin-Hamiltonian parameters given in the text. The scale of the graph is set to optimally show the broad signals outside the $g = 2$ (at 9.838 T) region. The $g = 2$ region is shown in detail in Figure 6.2. The experimental spectra are baseline corrected. An unknown impurity gives a negative signal at 9.6 T, marked with \star .

In the high-field limit, $\vec{S} \cdot \vec{D} \cdot \vec{S} \ll \mu_B \vec{B}_0 \cdot \vec{g} \cdot \vec{S}$, the ZFS term may be treated as a perturbation. [45] [64] As a result the magnetic sublevels split linearly with the applied magnetic field and only allowed transitions ($\Delta m_s = \pm 1$) occur. In a frozen solution spectrum this leads to equidistant transitions with their spacing determined by D_i , the principal values of the ZFS tensor, according to

$$\Delta B_0 = \frac{3D_i}{\mu_B g_i} \quad (6.3)$$

6. The two Fe^{3+} binding sites in human serum transferrin distinguished by high-frequency EPR

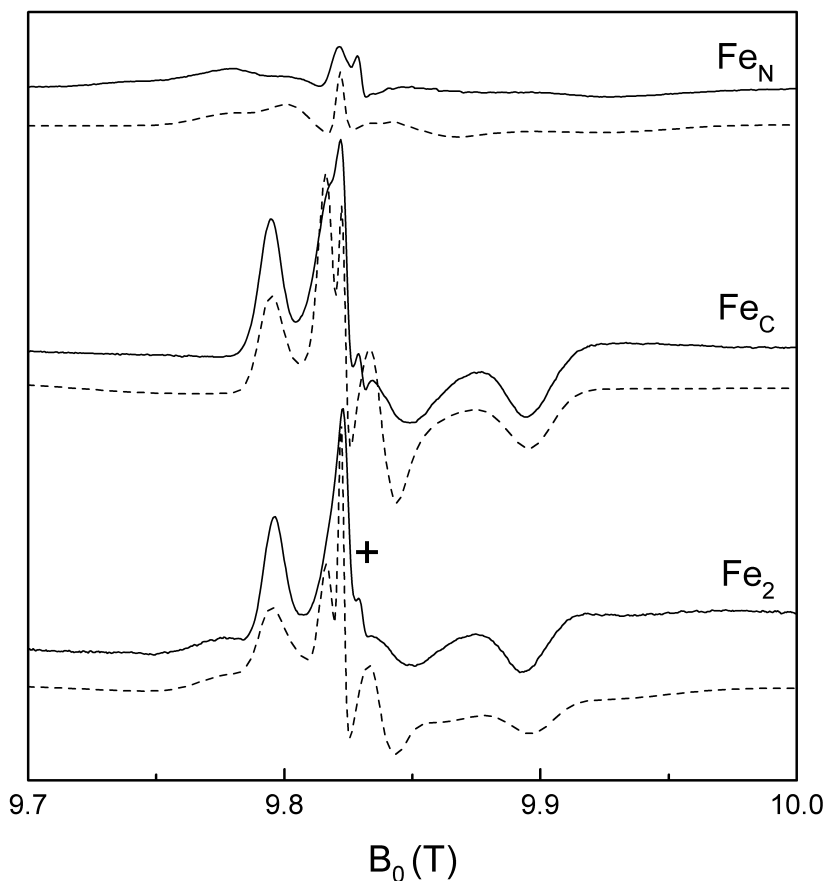


Figure 6.2: The $g = 2$ region of the J-band cw EPR spectra of 1 mM frozen solutions of Fe_N , Fe_C and Fe_2 human serum transferrin at 10 K. Experimental conditions were the same as for the spectra shown in Figure 6.1, except for the modulation amplitude, which was set to 0.8 mT. Solid lines: experimental spectra, dashed lines: spectra calculated using EasySpin and the spin-Hamiltonian parameters given in the text. The signal observed in all spectra at 9.830 T, marked with +, is due to an impurity in the frozen solution.

At the lowest temperatures transitions will show up above or below $g = 2$ depending on whether D_i is positive or negative, respectively, because the magnetic sublevels are populated according to Boltzmann.

From Equation 6.3 we estimate the values of D_z and D_y of the iron bound in the N- and the C-lobe from the two upper spectra in Figure 6.1. For both lobes the distance between the negative signals above $g = 2$ is larger than the distance between the positive signals below $g = 2$, which means that the negative signals yield a positive D_z and the positive signals yield a negative D_y . D_x follows from

$D_x + D_y + D_z = 0$. We estimate for the N-lobe $D = 11.7$ GHz and $\lambda = 0.21$ and for the C-lobe $D = 9.0$ GHz and $\lambda = 0.27$.

Fine tuning of the spin-Hamiltonian parameters was done by comparing the experimental spectra to spectra calculated by numerical diagonalization of the spin Hamiltonian using the EPR simulation package EasySpin. [6] The ZFS parameters that describe the electronic structure of the bound high-spin Fe^{3+} ion best are

$$\text{N-lobe: } D = 12.0 \text{ GHz, } \lambda = 0.20$$

$$\text{C-lobe: } D = 9.3 \text{ GHz, } \lambda = 0.25$$

We estimate the uncertainties to be ± 0.3 GHz for D and ± 0.01 for λ from the changes the J-band spectra induced by a change in these parameters as calculated using EasySpin. An increase of the g values from the free-electron value to $g_x = 2.004 \pm 0.0005$, $g_y = 2.0042 \pm 0.0002$, $g_z = 2.0042 \pm 0.0002$ was found to improve the match with the experimental spectra, particularly in the $g = 2$ region. These spin-Hamiltonian parameters were used for the simulated spectra shown in Figure 6.1 and Figure 6.2. In order to reproduce the width and shape of the resonances, the spectra were simulated taking into account a strain in D and E , using a first-order approximation.¹ For the Fe_C spectra a strain of 20 % was used in both D and E , for the Fe_N spectra a strain of 20 % was used in E and of 30 % in D .

The Fe_2 spectrum is clearly a sum of the Fe_C spectrum and the Fe_N spectrum. For the simulation of the Fe_2 spectrum, shown in Figure 6.1 and 6.2, equal contributions of the N- and C-lobe are assumed.

6.5 Discussion

The cw J-band spectra of wild-type hTF show the signals of the high-spin Fe^{3+} ions bound to the two lobes of hTF clearly resolved. This allows in principle quantitative analysis of the electronic structure of the iron bound in the individual lobes, although, particularly concerning the shallow negative peaks, doubts may arise as to which signals belong together. The spectra of the monoferric mutants of hTF erase those doubts and, moreover, show that the Fe_2 spectrum is a sum of the Fe_C spectrum and the Fe_N spectrum. We conclude that, as far as we can resolve with cw EPR at 275.7 GHz, the presence of an Fe^{3+} ion in one lobe does not alter the electronic structure of the iron-binding site in the other lobe.

The ZFS parameters of the bound Fe^{3+} ion differ considerably for the two lobes. To interpret these differences these parameters have to be translated into electronic structure using advanced quantum-chemical methods. Considerable progress has

¹See the online documentation on EasySpin. A Gaussian is added to the spectrum of a width proportional to the derivative of the resonance field with respect to, for instance, D of a given transition.

6. The two Fe^{3+} binding sites in human serum transferrin distinguished by high-frequency EPR

been made with such calculations in recent years, in particular based on density-functional theory. [8] The calculation of the ZFS for transition-metal ions is, however, still in an exploratory stage and interpretation of the spin-Hamiltonian parameters of the high-spin Fe^{3+} bound to transferrin in terms of the electronic structure and the relation between geometry and function is not yet within reach.

In 1972 Aasa *et al.* concluded that the characteristic spectrum of hTF at X band had to derive from at least two components, one with an almost rhombic ZFS tensor, $\lambda = 0.325$, and one with a ZFS tensor of lower rhombicity, between 0.2 and 0.27. [140] Their logical guess was that these two components correspond to the two lobes of hTF. In their paper from 1987 Yang and Gaffney even invoke three components to explain the X-band hTF spectrum. [86] The remarkable fact is that the X-band spectra of the monoferric forms of transferrin show the same characteristics, [131, 133, 143, 147] which removes the basis for an interpretation of these spectra in terms of multiple components.

Neither our J-band spectra of the two monoferric hTFs nor our J-band spectra of wild-type hTF show a sign of the presence of high-spin Fe^{3+} sites with another electronic structure than those described by the parameter sets we obtained for the N-lobe and the C-lobe. Moreover, the rhombicity of the ZFS-tensors we found for both iron-binding sites, $\lambda = 0.20$ and 0.25 for the N- and the C-lobe respectively, is not compatible with the rhombicity found from X-band spectra by Aasa *et al.* We have attempted to simulate the X-band spectra of hTF with the parameter sets established from the J-band spectra using EasySpin, but were not successful. Thus, the cw J-band spectra of hTF have provided us with essential, new information on the electronic structure of the two iron-binding sites of hTF, but more information is still hidden in the X-band spectra.

6.6 Conclusion

The high frequency and the high sensitivity with which the EPR spectra of hTF are recorded make it possible to distinguish in the wild-type spectrum the high-spin Fe^{3+} ions bound in the N-lobe and in the C-lobe. The EPR signals of the iron bound by the N-lobe or the C-lobe are quantitatively analyzed in terms of their spin-Hamiltonian parameters. The quantitative understanding of the high-frequency transferrin EPR spectra has brought us in a good starting position to finally understand the X-band spectrum of transferrin. Moreover, the sensitivity of the high-frequency spectra to small changes in the electronic structure of the high-spin Fe^{3+} binding sites opens up the way to deepen our understanding of the iron binding and the iron-binding mechanism by transferrin through a combination of biochemistry and EPR spectroscopy.

Chapter 7

Configuration of spheroidene in the photosynthetic reaction center of *Rb. sphaeroides*: A comparison of wild type and reconstituted R26

We compare the resonance Raman spectra acquired at two excitation wavelengths, 496.5 and 514.5 nm, of spheroidene in the wild-type reaction center of *Rhodobacter sphaeroides* and reconstituted into the reaction center of the *Rhodobacter sphaeroides* mutant R26. Our earlier work showed that the reconstituted R26 reaction center holds spheroidene in two configurations: 15,15'-*cis* and another configuration. Here we show that in the wild-type reaction center only 15,15'-*cis* spheroidene is present. In the resonance Raman spectra of the reconstituted R26 reaction centers a transition is identified that arises exclusively from the second configuration. According to density-functional-theory calculations this transition is specific for the 13,14-*cis* configuration.

Guinevere Mathies, Marc C. van Hemert, Peter Gast, Karthick B. Sai Sankar Gupta, Harry A. Frank, Johan Lugtenburg, and Edgar J. J. Groenen, *J. Phys. Chem. A*, 115:34 (2011) 9552-9556.

7. Configuration of spheroidene in the photosynthetic reaction center of *Rb. sphaeroides*: A comparison of wild type and reconstituted R26

7.1 Introduction

The primary process of bacterial photosynthesis is a transmembrane charge separation. The minimum structural unit capable of producing the charge separation is an integral membrane complex termed the reaction center (RC), which was first isolated from the purple photosynthetic bacterium *Rhodobacter (Rb.) sphaeroides*. [153] Like all bacterial RCs the RC of *Rb. sphaeroides* contains a carotenoid. If excess light is supplied to the RC, a triplet state of the primary donor is generated, which can result in the formation of singlet oxygen. The carotenoid quenches this triplet state through energy transfer, which produces a triplet carotenoid. [154–156] To understand this photoprotective mechanism, it is important to know the structure of the carotenoid in the RC.

The carotenoid present in anaerobically grown *Rb. sphaeroides* RCs is spheroidene (see Figure 7.1). Early spectroscopic studies suggested that spheroidene assumes a *cis* configuration in the RC. [157, 158] Comparison of the resonance Raman spectra of spheroidene in RCs with resonance Raman spectra of *cis* isomers of β -carotene shows a strong resemblance between spheroidene in the RC and 15,15'-*cis* β -carotene. [159, 160] Both spectra display a clear band around 1240 cm^{-1} , which is not observed in the resonance Raman spectra of other *cis* isomers of β -carotene.

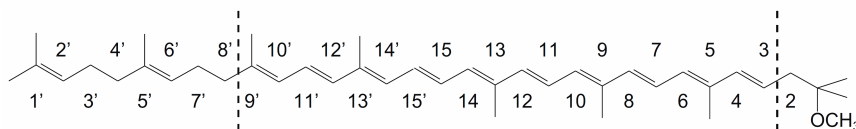


Figure 7.1: Schematic representation of spheroidene and the labeling of the carbon atoms. The molecule is shown in the all-*trans* form. The dashed lines indicate the conjugated region.

The structures of the RCs from three wild-type strains are known from X-ray diffraction. [161–163] The presence of spheroidene in a 15,15'-*cis* configuration is consistent with the electron density map, but the resolution of these structures is insufficient to position a *cis* bond uniquely. In 2000, the electron density map of the RC from the mutant AM260W of *Rb. sphaeroides*, which contains spheroidenone, was determined by X-ray diffraction and clearly favored a 15,15'-*cis* configuration above a 13,14-*cis* configuration. [164, 165]

In a long-term project, we have contributed to the study of the configuration of spheroidene in the RC of *Rb. sphaeroides* by combining resonance Raman spectroscopy with density-functional-theory (DFT) calculations. [17, 18, 166, 167] RCs from the carotenoidless mutant *Rb. sphaeroides* R26 were reconstituted with isotopically labeled spheroidenes. The use of specific ^{13}C and ^2H labeled spheroidenes

enabled the assignment of normal modes to transitions observed in the resonance Raman spectra. The normal mode underlying the transition around 1240 cm^{-1} was identified and found to uniquely refer to the *cis* nature of the 15,15' carbon-carbon double bond. [18]

Detailed comparison of resonance Raman spectra and results of DFT calculations also revealed that besides the 15,15'-*cis* configuration another configuration of spheroidene occurs in significant proportion in the reconstituted R26 RC. [18] The DFT calculations for many structures of spheroidene consistently show that two transitions have appreciable intensity in the region between 1500 and 1570 cm^{-1} of the resonance Raman spectrum, where C=C stretch vibrations typically occur. However, the experimental spectra of several isotopically labeled spheroidenes that were reconstituted into the R26 RC clearly display three or four transitions in this region. This observation can be understood if a second configuration is present. The trend in the shift of the third and fourth transition with the position of the isotope in spheroidene identified the 13,14-*cis* configuration as a likely candidate.

The question remained whether the wild-type RC of *Rb. sphaeroides* contains a second configuration as well, besides the 15,15'-*cis*. The answer to this question is relevant, because the structure and thereby the energy of the triplet state determine the rate of excitation transfer by which spheroidene fulfills its photoprotective function. [154–156] In addition, it is important to know whether conclusions drawn from studies on the reconstituted R26 RC of *Rb. sphaeroides* apply to wild type as well, as is suggested by several observations. The structures determined by X-ray diffraction of the reconstituted R26 RC and of the wild-type RC show very similar binding of the carotenoid. [156, 164, 165] Also, the electron paramagnetic resonance spectra of the triplet excited spheroidene in wild-type and reconstituted in R26 RC are indistinguishable. [168] However, the resonance Raman spectra recorded with excitation wavelength 496.5 nm of the wild-type RC and the reconstituted R26 RC show minor differences. [169]

We compare the resonance Raman spectra acquired at two excitation wavelengths, 496.5 and 514.5 nm , of the wild-type RC and the reconstituted R26 RC. We find that, while spheroidene is present in the reconstituted R26 RC in the 15,15'-*cis* configuration and in another configuration, the wild-type RC contains only 15,15'-*cis* spheroidene. In the resonance Raman spectra of the reconstituted R26 reaction centers a transition is identified that arises exclusively from the second configuration. Mode composition analysis shows that this transition corresponds to a mode that is specific for the 13,14-*cis* configuration.

7.2 Methods

The wild-type RCs were obtained from *Rb. sphaeroides* strain 2.4.1 as described in Shochat *et al.* [170] RCs from *Rb. sphaeroides* R26 were obtained as described

7. Configuration of spheroidene in the photosynthetic reaction center of *Rb. sphaeroides*: A comparison of wild type and reconstituted R26

in Feher and Okamura. [171] To reconstitute spheroidene into the R26 RCs the following procedure was followed. A spheroidene solution in hexane was dispersed in a 1% Triton X-100 solution. To evaporate the hexane, this solution was heated to about 80 °C and stirred until it became clear. The solution was then cooled to room temperature. Solutions of spheroidene prepared in this way remained transparent for several hours at room temperature. Reconstitution was performed by adding the Triton/spheroidene solution to the R26 RCs in TL buffer (10 mM Tris pH 8, 0.1% LDAO, 1 mM EDTA) such that the Triton solution was < 0.1% and the spheroidene-RC ratio was ten, and stirring for six hours. The excess spheroidene was removed by washing the RCs on a DEAE column.

To obtain a glass-like sample at cryogenic temperatures, the samples consisted of one part reaction centers in TL buffer and one part glycerol. This mixture had an optical density of about 0.5 at 496.5 nm. For the resonance Raman experiments a sample volume of 150 μl in a glass tube of 3 mm diameter was used.

Resonance Raman scattering was induced by the 496.5 and 514.5 nm lines of a Spectra Physics model Stabilite 2017 Ar⁺ laser. The scattered light was collected at an angle of 90° and imaged on the entrance slit of an Acton Research SpectraPro-500i spectrograph, which contained a grating of 1200 g mm⁻¹. A notch filter (496.5 nm: Omega Optical Inc., 514.5 nm: Iridian Spectral Technologies) was used to remove light of the excitation wavelength and eliminate “ghost” lines which result from irregularities in the grating. Spectra are collected using a CCD camera (Princeton Instruments Spec-10 system). The dispersion was approximately 1 cm⁻¹ per pixel. Calibration was performed using a set of calibration lamps.

Spectra were recorded at a temperature of 77 K. Illumination power was about 100 mW for the spectra recorded at 496.5 nm and about 25 mW for the spectra recorded at 514.5 nm. The illumination time was 10 min.

The vibrational modes of 15,15'-*cis* and 13,14-*cis* and their resonance Raman activity were calculated as described in references 17 and 18. In short, the Gaussian 03 package, Revision E.01, was used for geometry optimization and subsequent calculation of the Hessian. [172] The DFT calculations were performed with the B3LYP functional and the densities were expressed in a 6-31G* basis. The normal modes and corresponding frequencies were calculated using the Wilson GF formalism using the expressions for the transformation between Cartesian and internal coordinates given by Califano. [173] The internal coordinates were used to estimate the resonance Raman intensities according to

$$I_{\alpha} \propto \nu_{\alpha} \left(\sum_i A_{\alpha i} \delta_i \right)^2. \quad (7.1)$$

In this formula ν_{α} is the frequency of the normal mode α , A represents the coordinate transformation matrix and δ_i is the change in internal coordinate i as a result of the (near-)resonant electronic $\pi^* \leftarrow \pi$ transition. [174] The strength of the method

has been shown by the complete description of the resonance Raman spectra of isotopically labeled all-*trans*-spheroidene in solution. [17]

7.3 Results and discussion

Figure 7.2 shows the resonance Raman spectra of reconstituted R26 and wild-type RCs recorded at an excitation wavelength of 496.5 nm. In both spectra the resonance Raman transition that is characteristic of the 15,15'-*cis* configuration is observed at 1239 cm^{-1} [18]. To compare the R26 spectra and the wild-type spectra, the spectra were normalized to the integrated intensity of the 1239 cm^{-1} transition, which was determined by fitting a Gaussian function to the transition and taking its surface area. Normalization to this band assures that in both spectra the contribution from the 15,15'-*cis* configuration is the same.

Several differences between the reconstituted R26 and the wild-type spectra are observed: (i) the shape of the broad band around 1535 cm^{-1} differs; (ii) upon normalization to the 1239 cm^{-1} transition, the intensity of all other bands is less in the wild-type spectrum than in the R26 spectrum; (iii) the ratio of the intensities of the bands at 1158 and at 1170 cm^{-1} is slightly different; and (iv) the wild-type spectrum shows a weak band at 1139 cm^{-1} , while the reconstituted R26 spectrum shows a band at 1142 cm^{-1} of a five times higher intensity. The last three of these differences were already reported by Agalidis *et al.*, [169] but not yet explained.

The upper panel of Figure 7.3 shows the broad band around 1535 cm^{-1} observed upon excitation at 496.5 nm for both wild type and reconstituted R26 RCs in detail. At cryogenic temperatures, a single resonance Raman transition typically has a width (FWHM) of about 8 cm^{-1} . The band observed at 1535 cm^{-1} for the reconstituted R26 RC appears to arise from more than two transitions. In contrast, the band in the wild-type spectrum may well derive from two transitions.

Resonance Raman spectra of both reconstituted R26 RCs and wild-type RCs were also recorded at the excitation wavelength 514.5 nm (see Appendix D). The differences between wild-type and reconstituted R26 that were observed at 496.5 nm are also observed in these spectra. The upper panel of Figure 7.4 shows the broad band around 1535 cm^{-1} at excitation wavelength 514.5 nm in detail. In the wild-type spectrum two transitions are resolved, while the band observed for the reconstituted R26 RCs is again considerably broader.

According to DFT calculations the resonance Raman spectra of spheroidene will contain two resonance-enhanced Raman transitions in the C=C stretch region between 1500 and 1570 cm^{-1} , independent of the configuration of the carbon chain. [17, 18] The observation of two transitions in this region in the wild-type spectra means that the wild-type RC contains spheroidene in one configuration. The presence of the transition at 1239 cm^{-1} assures that this is the 15,15'-*cis* configuration.

The lower panels of Figure 7.3 and 7.4 display spectra that result from subtraction

7. Configuration of spheroidene in the photosynthetic reaction center of *Rb. sphaeroides*: A comparison of wild type and reconstituted R26

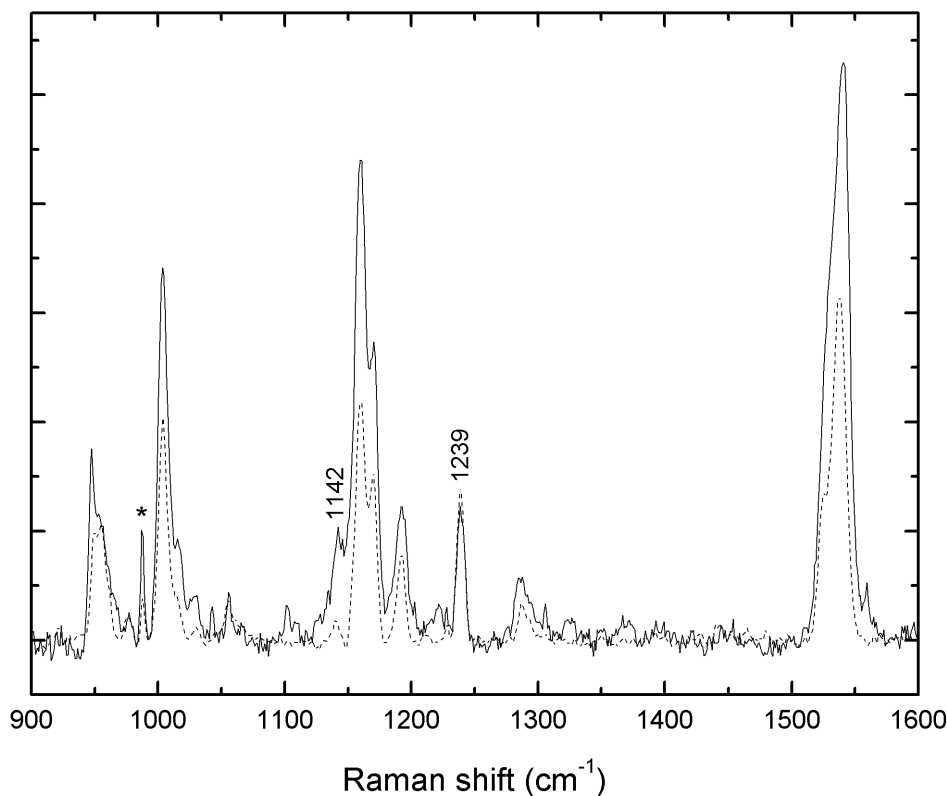


Figure 7.2: Resonance Raman spectra of reconstituted R26 and wild-type RCs with excitation at 496.5 nm: solid line: R26, dashed line: wild type. The spectra are normalized to the intensity of the 1239 cm⁻¹ transition, which is characteristic for the 15,15'-*cis* configuration. The peak denoted with an asterisk is an argon plasma line. A fluorescence background was subtracted.

of the wild-type spectra from the R26 spectra after normalization to the 1239 cm⁻¹ transition. These difference spectra also show two transitions, again better resolved for excitation at 514.5 nm.

It is possible to fit two Gaussian functions to the two wild-type spectra and to the two difference spectra. The results of these fits are summarized in Table 7.1. The centers of the two transitions observed in the wild-type spectra are the same, within the experimental error, at both excitation wavelengths. The same holds for the difference spectra.

From the analysis of the resonance Raman spectra of specific isotope-labeled spheroidenes reconstituted into the R26 RC, Wirtz *et al.* [18] concluded that besides the 15,15'-*cis* configuration a second configuration of spheroidene is present in the

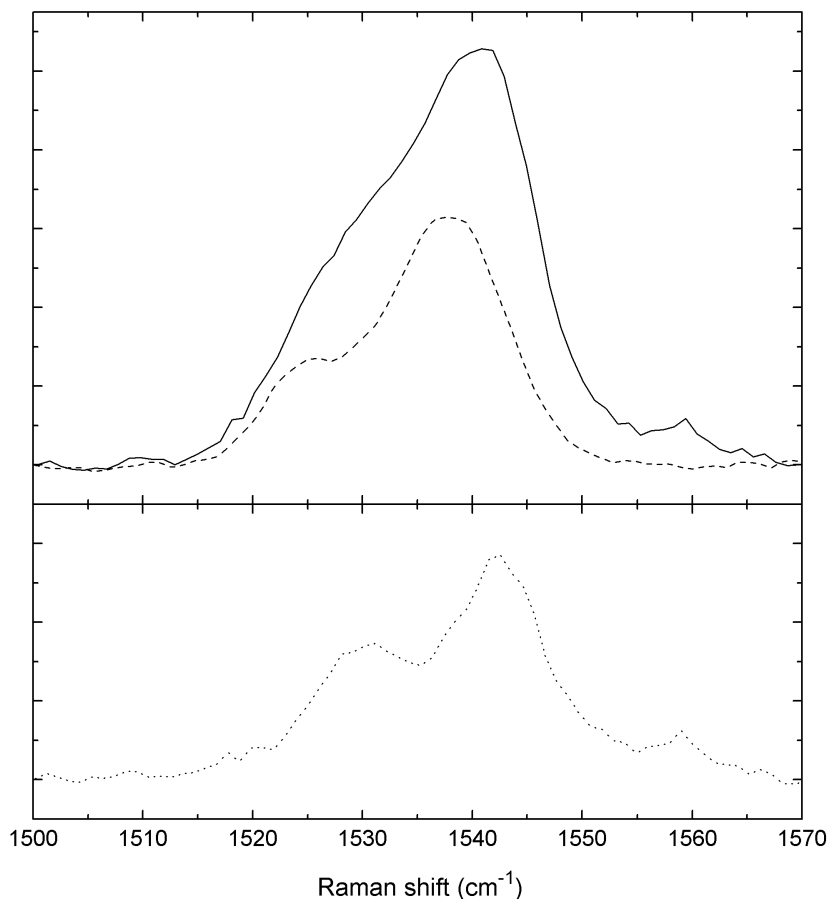


Figure 7.3: Upper panel: Detail of the resonance Raman spectra of reconstituted R26 (solid line) and wild-type (dashed line) reaction centers. Excitation wavelength: 496.5 nm. The two spectra are normalized to the integrated intensity of the 1239 cm^{-1} transition. Lower panel: Difference of the two spectra shown in the upper panel (R26 – wild type).

R26 RC. This is confirmed by the presence of two C=C modes in the difference spectra.

The presence of an additional configuration of spheroidene in the R26 RC offers an explanation for the differences between the resonance Raman spectra of wild-type and reconstituted R26 RCs (see Figure 7.2 and Appendix D). First, the different shape of the broad band around 1535 cm^{-1} results from the fact that this band derives from two C=C stretch modes for the wild-type RC and from four for the reconstituted R26 RC. Second, the additional configuration is responsible for the “extra” intensity in the R26 spectra as compared to the wild-type spectra after

7. Configuration of spheroidene in the photosynthetic reaction center of *Rb. sphaeroides*: A comparison of wild type and reconstituted R26

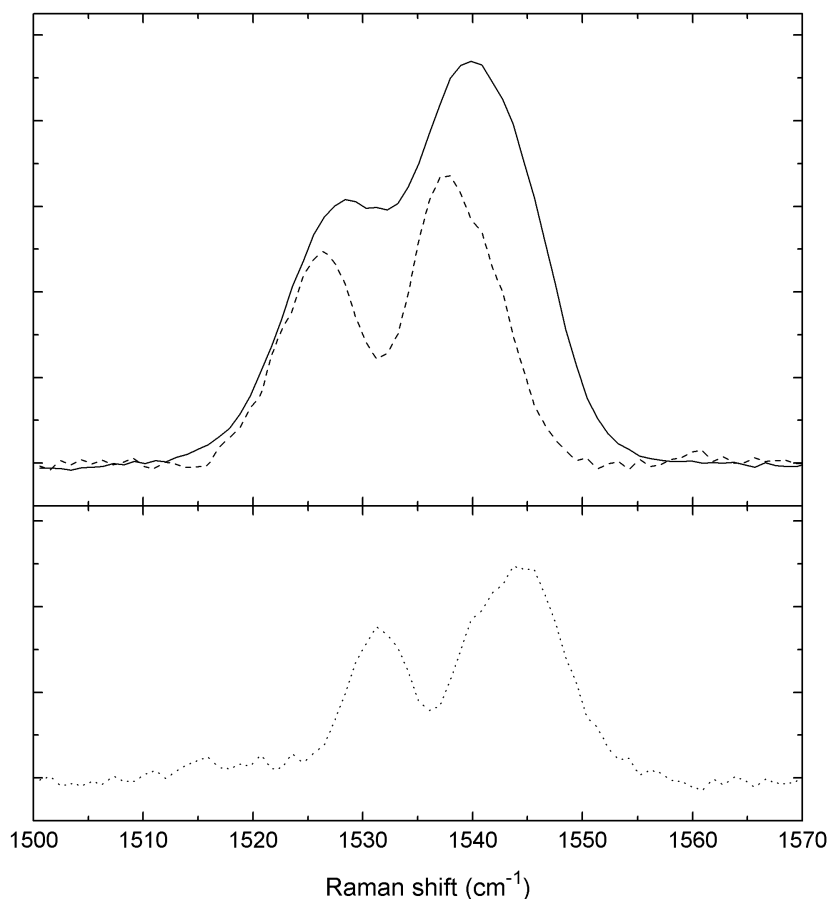


Figure 7.4: Upper panel: Detail of the resonance Raman spectra of reconstituted R26 (solid line) and wild-type (dashed line) reaction centers. Excitation wavelength: 514.5 nm. The two spectra are normalized to the integrated intensity of the 1239 cm^{-1} transition. Lower panel: Difference of the two spectra shown in the upper panel (R26 – wild type).

normalization at 1239 cm^{-1} . Third, the shape of the spectrum in the fingerprint region around 1160 cm^{-1} is expected to be different for the two configurations, which explains the difference between the wild-type and reconstituted R26 spectra in this region. Finally, the absence of the transition at 1142 cm^{-1} in the wild-type spectra suggests that this transition corresponds to a mode that is characteristic for the second configuration in the R26 RC.

Wirtz *et al.* [18] concluded that the isotope-induced shifts of the transitions in the C=C stretch region of the R26 spectra that do not belong to the 15,15'-*cis* configuration, were qualitatively consistent with a 13,14-*cis* configuration. Koyama

7.3. Results and discussion

	peak center 1 (cm^{-1})	line width 1 (cm^{-1})	peak center 2 (cm^{-1})	line width 2 (cm^{-1})
WT 514.5	1525.8	8.1	1538.4	9.6
WT 496.5	1524.9	9.3	1537.8	9.3
R26 – WT 514.5	1531.2	6.6	1543.9	10.4
R26 – WT 496.5	1529.2	10.9	1542.5	11.7

Table 7.1: Peak center positions and line widths of the bands in the 1500 - 1570 cm^{-1} region. The spectra of wild-type RCs and the spectra resulting from subtraction of the spectrum of the wild-type RC from the spectrum of the reconstituted R26 RC as shown in Figure 7.3 and 7.4 were fitted with two Gaussian functions. The error in the distance between two peak center positions within one spectrum as determined by Gaussian fitting is estimated to be at most 2 cm^{-1} .

et al. [159, 160] report on a transition that is typically observed in the 1120 - 1140 cm^{-1} region of the resonance Raman spectra of isomers of β -carotene that have a 13,14-*cis* bond. We calculated the compositions of the normal modes of spheroidene in the 13,14-*cis* configuration assuming a structure in which the C-atoms of the methyl groups of spheroidene were at the coordinates found from X-ray diffraction by McAuley *et al.* [164] A mode at 1128 cm^{-1} that is characteristic for the 13,14-*cis* configuration and comparable in composition to the 1239 cm^{-1} mode of the 15,15'-*cis* configuration is calculated to gain intensity in a resonance Raman experiment. Both modes consist mainly of two in-phase stretch vibrations of the two single carbon-carbon bonds adjacent to the *cis* bond (see Figure 7.5 and 7.6). In the case of the 13,14-*cis* configuration one of the C-atoms that participates in the *cis* bond has a methyl group attached. Together with a stronger delocalization this increased mass is responsible for the lower wavenumber of this mode for the 13,14-*cis* configuration (1142 compared to 1239 cm^{-1}).

Depending on the preparation of the reconstituted R26 RCs, the ratio of the intensities of the 1158 and 1170 cm^{-1} bands and the shape of the broad band around 1535 cm^{-1} are found to vary (see Appendix D). The first of these variations was also described in reference 169. The resonance Raman spectra invariably show the presence of both 15,15'-*cis* and 13,14-*cis* spheroidene, as is clear from the presence of the 1239 and the 1142 cm^{-1} bands. The variations in the spectra can not be fully explained by a change in the relative contributions of the 15,15'-*cis* and the 13,14-*cis* configuration. Instead, they point to a slight variation in the structure of the carotenoid in the RC.

Transient absorption and EPR experiments performed on reconstituted R26 RCs give qualitatively identical results to wild-type RCs. [168, 175, 176] A quantitative comparison of the yields of triplet formation is yet to be performed. This could give

7. Configuration of spheroidene in the photosynthetic reaction center of *Rb. sphaeroides*: A comparison of wild type and reconstituted R26

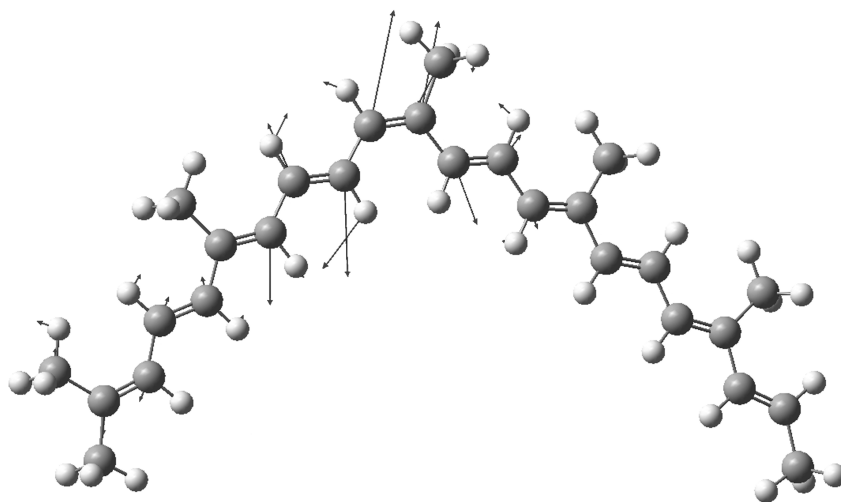


Figure 7.5: Composition of the normal mode characteristic of the 13,14-*cis* configuration of spheroidene. It is observed in the resonance Raman spectrum of spheroidene in the RC of *Rb. sphaeroides* at 1142 cm^{-1} . The mode consists mainly of single carbon-carbon bond stretches in the region close to the *cis* bond. Arrows indicate relative displacement, but are not drawn to scale. Displacement for hydrogen atoms has been scaled down.

information on how critical the 15,15'-*cis* configuration of spheroidene is and thereby on the triplet quenching mechanism.

7.4 Conclusion

Wild-type reaction centers of *Rb. sphaeroides* contain spheroidene in one configuration, namely 15,15'-*cis*. Reconstituted R26 reaction centers of *Rb. sphaeroides*, on the other hand, contain spheroidene in the 15,15'-*cis* and the 13,14-*cis* configuration. Hence, one must be careful in extrapolating results obtained for the reconstituted R26 reaction center to the wild-type reaction center.

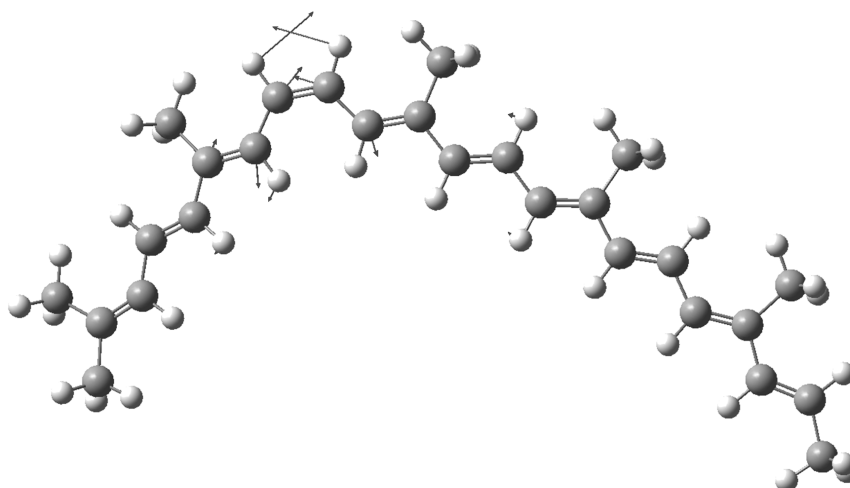


Figure 7.6: Composition of the normal mode characteristic of the 15,15'-*cis* configuration of spheroidene. It is observed in the resonance Raman spectrum of spheroidene in the RC of *Rb. sphaeroides* at 1239 cm^{-1} . The mode consists almost exclusively of the carbon 14'-15' and 15-14 stretches and the C-H bend vibrations at the 15 and 15' positions. Arrows indicate relative displacement, but are not drawn to scale. Displacement for hydrogen atoms has been scaled down.

7. Configuration of spheroidene in the photosynthetic reaction center of *Rb. sphaeroides*: A comparison of wild type and reconstituted R26

Appendix A

Continuous-wave 275.7 GHz EPR spectra of rubredoxin from *Pyrococcus furiosus* and *Megasphaera elsdenii*

Figure A.1 and A.2 show the 275.7 GHz cw EPR spectra of frozen solutions of rubredoxin originating from *P. furiosus* and *M. elsdenii*.

A. Continuous-wave 275.7 GHz EPR spectra of rubredoxin from *Pyrococcus furiosus* and *Megasphaera elsdenii*

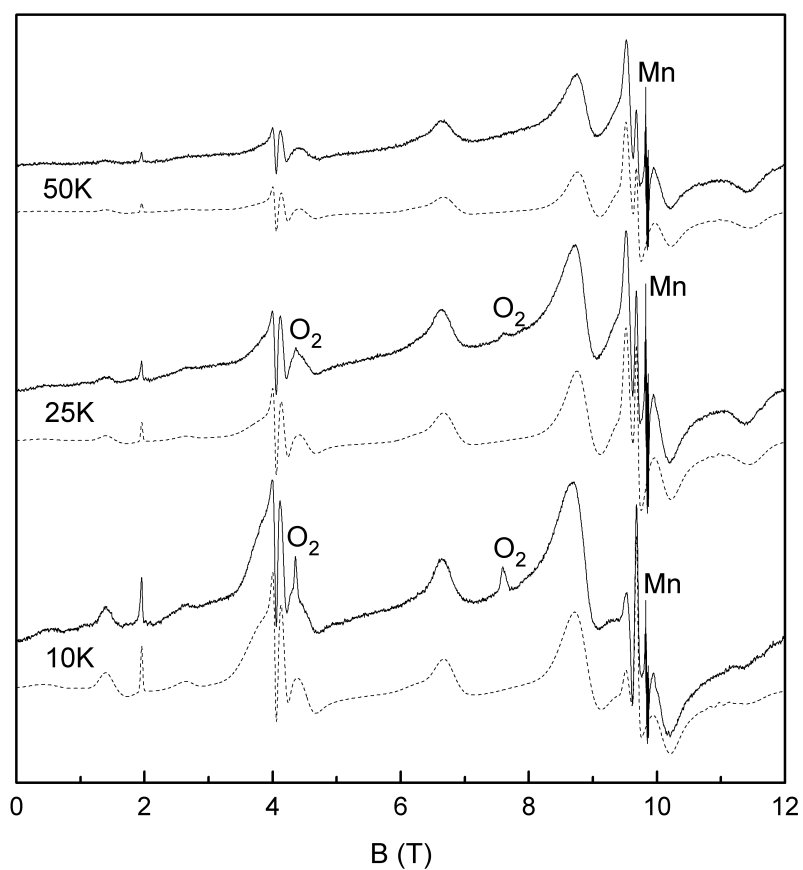


Figure A.1: The 275.7 GHz cw EPR spectra of a 10 mM frozen solution of the protein rubredoxin from *P. furiosus* at three temperatures. Experimental conditions: modulation amplitude: 3 mT, time constant: 1 s, scan rate: 2 mT/s, microwave power: 1 μ W. The solid lines are the experimentally observed spectra and the dashed lines are the spectra calculated by EasySpin with the parameters given in Table 2.1.

A. Continuous-wave 275.7 GHz EPR spectra of rubredoxin from *Pyrococcus furiosus* and *Megasphaera elsdenii*

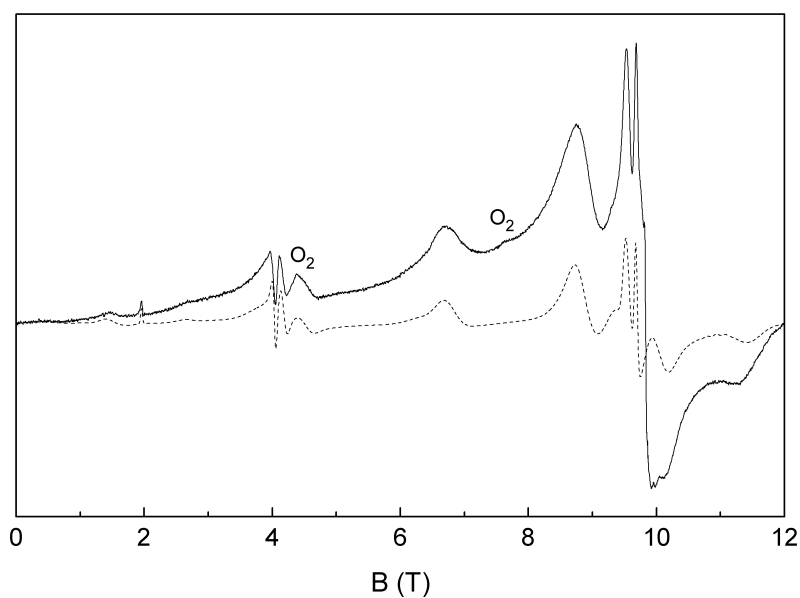


Figure A.2: The 275.7 GHz cw EPR spectrum of a 10 mM frozen solution of the protein rubredoxin from *M. elsdenii* at 25 K. Experimental conditions: modulation amplitude: 3 mT, time constant: 1 s, scan rate: 2 mT/s, microwave power: 1 μ W. The solid line is the experimentally observed spectrum and the dashed line is the spectrum calculated by EasySpin with the parameters given in Table 2.1.

A. Continuous-wave 275.7 GHz EPR spectra of rubredoxin from
Pyrococcus furiosus and *Megasphaera elsdenii*

Appendix B

The revised mount of the modulation coil of the 275.7 GHz continuous-wave probe head

After repeated use of the continuous-wave probe head of the 275.7 GHz spectrometer, the quality of the spectra would deteriorate. Particularly at temperatures below 10 K the stability of the EPR signal became poor. Upon inspection of the probe head it was found that the rexolite part of the modulation coil mount was cracked. Therefore the modulation coil mount described in Chapter 2 was replaced by the mount shown in Figure B.1.

B. The revised mount of the modulation coil of the 275.7 GHz continuous-wave probe head

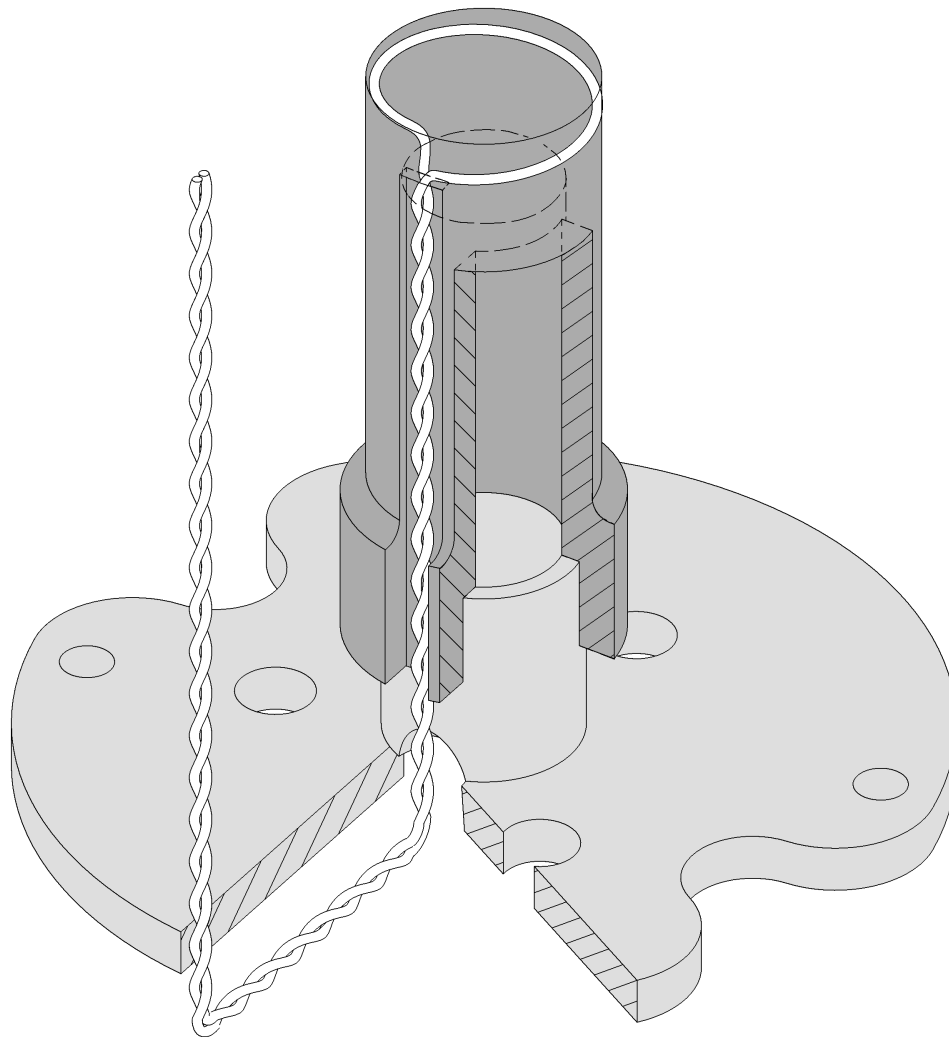


Figure B.1: Technical drawing of the revised modulation coil mount. Light gray: Bronze. The bottom plate is attached to the end of the probe head. Dark gray: Stycast. The modulation coil is encased in Stycast. For clarity only one turn is depicted.

Appendix C

EPR spectroscopy on Co(II)-rubredoxin

C.1 Introduction

In Chapter 3 of this thesis the effect is investigated of the subtle differences in geometry between the active sites of rubredoxin and desulfuredoxin on the electronic structure of these sites, which contain in their oxidized state a high-spin Fe^{3+} ion. EPR spectra at J band (275.7 GHz) were recorded on frozen solutions of rubredoxin, see Chapter 2, and desulfuredoxin, see Chapter 3, and from these spectra an accurate set of spin-Hamiltonian parameters describing the active site of each protein could be determined. Particularly the difference in the rhombicity of the zero-field splitting tensor, λ , is remarkable: 0.26 for rubredoxin, and 0.074 for desulfuredoxin.

In Chapter 3 X-band (9.5 GHz) spectra are reported on a frozen solution of Co(II)-substituted desulfuredoxin. From these spectra the value of λ of the Co(II)-substituted active site of desulfuredoxin was estimated to be 0.26. In order to quantify also the effect of the geometry differences between rubredoxin and desulfuredoxin on the electronic structure of the high-spin Co^{2+} containing active sites, it would be desirable to have data on the electronic structure of the Co(II)-substituted active site of rubredoxin. Unfortunately we were not successful in detecting an EPR signal of a frozen solution of Co(II)-substituted rubredoxin. Here we report our attempts and discuss possible explanations for the absence of an EPR signal.

C.2 Materials and methods

Rubredoxin from *Desulfovibrio gigas* was purified according to a previously reported method. [47] Reconstitution with Co^{2+} was performed as described in reference [81]. The protein was kept in Tris buffer at pH 7.6. Samples for X-band EPR contained 20% glycerol.

C. EPR spectroscopy on Co(II)-rubredoxin

Continuous-wave (cw) and pulsed X-band spectra were recorded on the Bruker Elexsys E680 spectrometer using the TE₁₀₂ rectangular cavity equipped with the ESR 900 Cryostat (Oxford Instruments) and the FlexLine probe head with the ER4118 X-MD5 resonator with a CF935W flow cryostat, respectively. Pulsed W-band (94.9 GHz) spectra were recorded on an in-house developed spectrometer. [82] The cw J-band EPR spectra were recorded on an in-house developed spectrometer [9] using a probe head, specialized for operation in cw mode [64].

C.3 Results

Figure C.1 shows the cw X-band EPR spectra of a 400 μM frozen solution (from batch 1) of Co(II)-substituted rubredoxin at 5 and 40 K. The spectra show a broad, positive signal from 0 to about 100 mT. Figure C.2 shows the cw X-band EPR spectra of a 1.6 mM frozen solution (from batch 2) of Co(II)-substituted rubredoxin at 10 and 20 K. These spectra also show a broad, positive signal from 0 to about 100 mT, but its shape differs from the signal observed on the 400 μM frozen solution.

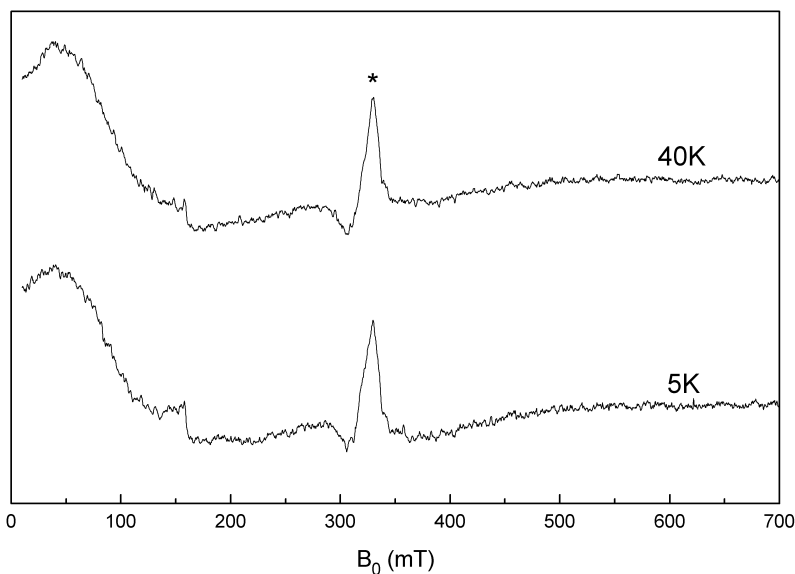


Figure C.1: X-band cw EPR spectra of a 400 μM frozen solution (batch 1) of Co(II)-rubredoxin from *D. gigas* at 5 and 40 K. Experimental conditions: modulation amplitude: 1.5 mT, microwave power: 200 mW, microwave frequency: 9.495 GHz. The spectra are baseline corrected. The signal marked with a \star around $g = 2$ is due to an impurity in the cavity/cryostat.

All four spectra show a signal around $g = 2$ (339 mT). This signal is due to an impurity in the cavity/cryostat. The spectra for batch 1 show a signal around

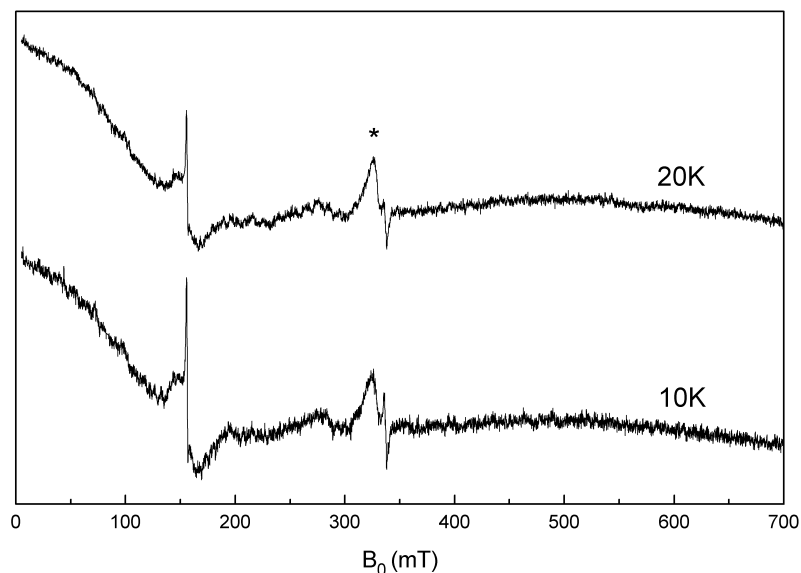


Figure C.2: X-band cw EPR spectra of a 1.6 mM frozen solution of Co(II)-rubredoxin from *D. gigas* at 10 and 20 K. Experimental conditions: modulation amplitude: 1 mT, microwave power: 20 mW, microwave frequency: 9.495 GHz. The spectra are baseline corrected. The signal marked with a \star around $g = 2$ is due to an impurity in the cavity/cryostat.

$g = 4.3$ (158 mT), which looks like a jump down in the EPR signal. The spectra for batch 2 also show a signal around $g = 4.3$, but this signal shows a clear structure. In the spectra for batch 2 two weak positive peaks show up at 190 and 275 mT.

Figure C.3 shows the cw X-band EPR spectra of a 400 μM frozen solution (batch 1) of Co(II)-substituted rubredoxin at 6, 20, 25 and 40 K to which NaNO_3 was added up to a concentration of 100 mM to increase the ionic strength of the solvent and hamper aggregation of the protein. These spectra do not show the broad signal at low field, but they do show the cavity impurity at $g = 2$, the signal at $g = 4.3$ and at 20 and 25 K the two weak positive peaks at 190 and 275 mT.

Attempts to detect a cw EPR spectrum at 5 and 25 K on a concentrated 10 mM solution of Co(II)-rubredoxin (batch 1) at J band were unsuccessful, as were attempts to detect a spin echo on a 1.6 mM frozen solution (batch 2) at 1.7 K at W band and at temperatures varying from 6 to 15 K at X band. The UV/VIS optical absorption spectrum of the batch 1 solution was measured and found to be similar to spectra reported in literature. [177] [81]

C. EPR spectroscopy on Co(II)-rubredoxin

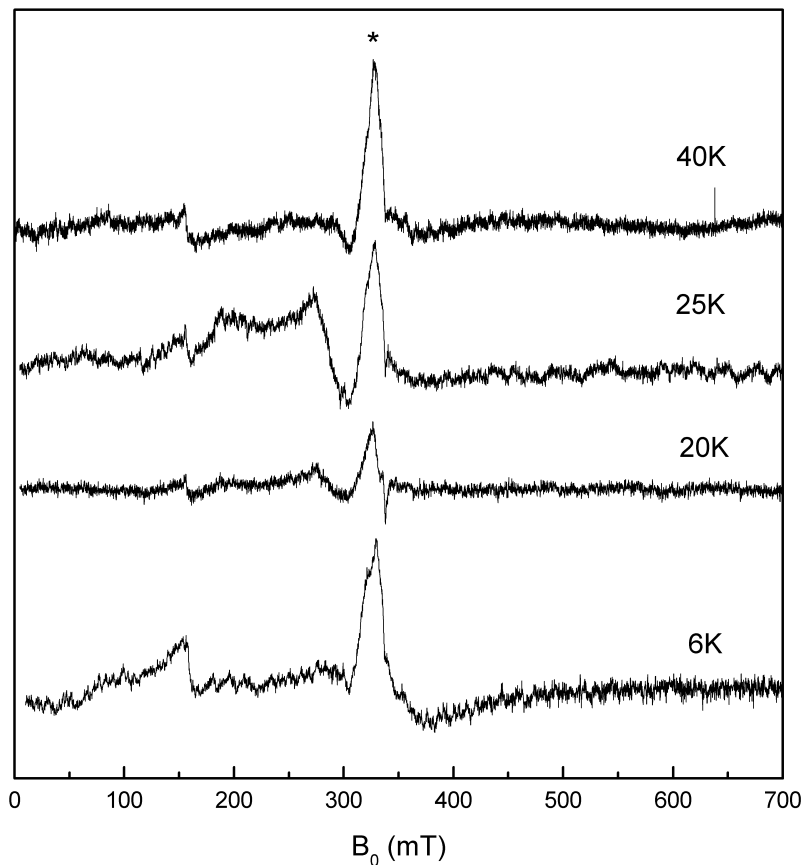


Figure C.3: X-band cw EPR spectra of a 400 μM frozen solution of Co(II)-rubredoxin from *D. gigas* in 100 mM NaNO₃ at 6, 20, 25 and 40 K. Experimental conditions spectra 6 and 40 K: modulation amplitude: 1.5 mT, microwave power: 200 mW, microwave frequency: 9.495 GHz. Experimental conditions spectra 20 and 25 K: modulation amplitude: 1 mT, microwave power: 20 mW, microwave frequency: 9.495 GHz. The spectra are baseline corrected. The signal marked with a \star around $g = 2$ is due to an impurity in the cavity/cryostat.

C.4 Discussion

The observed broad, positive signal from 0 to about 100 mT can not arise from a high-spin Co²⁺, $S = 3/2$, system. A transition at $B_0 = 0$ mT can not result from a transition within a Kramers doublet. The signal can not be due to an inter-doublet transition, since the zero-field splitting between the two doublets is expected to be much larger than 9.5 GHz for Co²⁺. The shape of the low-field signal is slightly different for the two batches/concentrations. The signal is no longer observed if the ionic strength of the solution is increased, which may prevent aggregation of the

protein. Possibly it is due to interacting Co^{2+} sites. An $S = 3$ could give a signal starting at zero field in X band.

The EPR spectra of biological materials often show a small signal around $g = 4.3$ of the shape found in the spectra in Figure C.1 and C.3, which is thought to be due to a rhombic high-spin Fe^{3+} contaminant, sometimes referred to as “garbage” iron. [178] The shape of the $g = 4.3$ signal in the spectra in Figure C.2, however, is characteristic of Fe(III)-rubredoxin. [58] In spite of the reconstitution with Co^{2+} , batch 2 still contains a fraction of Fe(III)-rubredoxin. This observation is remarkable, since May and Kuo state in reference [177] that the apoenzyme binds cobalt preferentially over iron. If the ZFS-tensor is close to axial and $D > 0$, a signal at $g = 4.3$ could arise at low temperatures due to high-spin Co^{2+} . However, the shape of this signal, taking into account broadening by conformational strain, will be considerably different from the $g = 4.3$ signal we observed.

The appearance of the two weak signals at 190 and 275 mT in the spectra is inconsistent. They likely arise from an impurity.

A possible explanation of the absence of an EPR signal from the Co(II)-substituted active site of rubredoxin is the following. If the ZFS-tensor of the site is close to axial, $\lambda \approx 0$, and $D < 0$, the transition within the lowest $\pm 3/2$ doublet is forbidden. A transition within the $\pm 1/2$ is allowed, but this doublet becomes only populated at elevated temperatures, at which the notoriously short relaxation times of high-spin Co^{2+} may have broadened the transition beyond detection.

Observation of an EPR spectrum at X band from Co(II)-rubredoxin was reported by Moura *et al.* [81], but the spectrum was not shown in this paper. Instead the reader is referred to a paper by Good and Vařák [179] in which an X-band EPR spectrum of Co(II)-metallothionein is shown. According to Moura *et al.* the spectrum of Co(II)-rubredoxin is similar.

C. EPR spectroscopy on Co(II)-rubredoxin

Appendix D

Supporting information on Chapter 7

Figure D.1 shows the resonance Raman spectra recorded on wild-type and reconstituted reaction centers of *Rhodobacter sphaeroides* R26 at excitation wavelength 514.5 nm. The differences between wild-type and reconstituted R26 are similar as observed at 496.5 nm.

Figure D.2 shows two resonance Raman spectra recorded at excitation wavelength 496.5 nm on reconstituted R26 reaction centers, which were prepared following different methods. The spectra invariably show the presence of both 15,15'-*cis* and 13,14-*cis* spheroidene, as is clear from the presence of the 1239 and the 1142 cm^{-1} bands. However, the ratio of the intensities of the 1158 and 1170 cm^{-1} bands and the shape of the broad band around 1535 cm^{-1} vary.

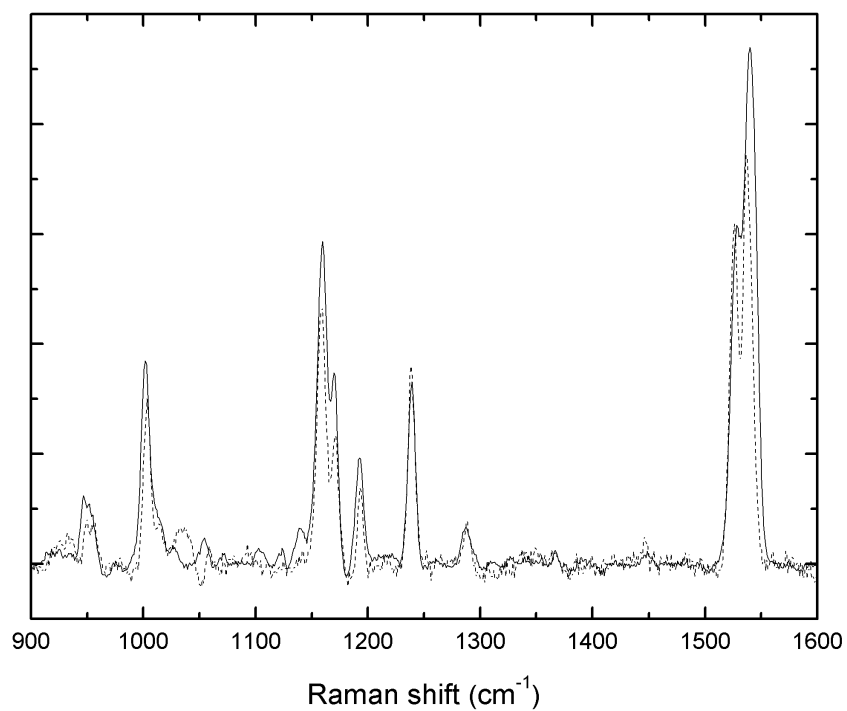


Figure D.1: Resonance Raman spectra of reconstituted R26 and wild-type *Rb. sphaeroides* reaction centers. Excitation wavelength: 514.5 nm. Solid line: R26, dashed line: wild-type. The two spectra are normalized to the integrated intensity of the 1239 cm⁻¹ transition. A fluorescence background, which, particularly for the wild-type sample, displays more structure than at excitation wavelength 496.5 nm, was subtracted.

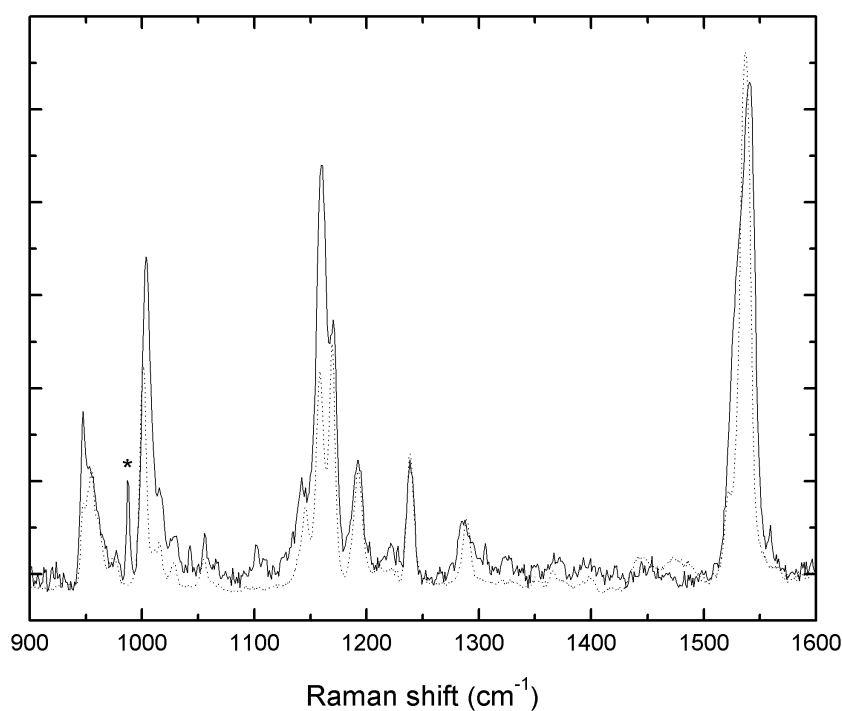


Figure D.2: Comparison of resonance Raman spectra of R26 reaction centers from two different batches in which spheroidene was reconstituted by two different methods. Excitation wavelength: 496.5 nm. Solid line: reconstitution as described in the Methods section of this paper, dotted line: reconstitution was performed using incubation in 1% LDAO and 400 mM NaCl as described by De Groot *et al.* [180] This last mentioned method was used for reconstitution in our previous work. [166] [167] [18] In order to compare the two spectra they are normalized to the integrated intensity of the 1239 cm⁻¹ line. The peak denoted with an asterisk is an argon plasma line. A fluorescence background was subtracted.

D. Supporting information on Chapter 7

Bibliography

- [1] ARTHUR SCHWEIGER AND GUNNAR JESCHKE. *Principles of pulsed electron paramagnetic resonance*. Oxford University Press, 2001.
- [2] M. H. L. PRYCE. **A Modified Perturbation Procedure for a Problem in Paramagnetism**. *Proc. Phys. Soc. A*, **63**:25–29, 1950.
- [3] A. ABRAGAM AND B. BLEANEY. *Electron Paramagnetic Resonance of Transition Ions*. Dover Publications, New York, 1986.
- [4] HENDRIK ANTHONY KRAMERS. *Quantum Mechanics*. North Holland Publishing Company, Amsterdam, 1957.
- [5] DIMITRIOS MAGANAS, SERGEY MILKISYANTS, JORRIT M. A. RIJN-BEEK, SILVIA SOTTINI, NIKOLAOS LEVESANOS, PANAYOTIS KYRITIS, AND EDGAR J. J. GROENEN. **A Multifrequency High-Field Electron Paramagnetic Resonance Study of Co^{II}S_4 Coordination**. *Inorg. Chem.*, **49**:595–605, 2010.
- [6] S. STOLL AND A. SCHWEIGER. **EasySpin, a comprehensive software package for spectral simulation and analysis in EPR**. *J. Magn. Reson.*, **178**:42–55, 2006.
- [7] J. R. PILBROW. **Effective g Values for $S = 3/2$ and $S = 5/2$** . *J. Magn. Reson.*, **31**:479–490, 1978.
- [8] MARTIN KAUPP, MICHAEL BÜHL, AND VLADIMIR G. MALKIN. *Calculation of NMR and EPR Parameters*. Wiley-VCH Verlag GmbH & Co. KGaA, Weinheim, 2004.
- [9] H. BLOK, J. A. J. M. DISSELHORST, S. B. ORLINSKII, AND J. SCHMIDT. **A continuous-wave and pulsed electron spin resonance spectrometer operating at 275 GHz**. *J. Magn. Reson.*, **166**:92–99, 2004.
- [10] JACQUES MEYER AND JEAN-MARC MOULIS. *Handbook of Metalloproteins*, chapter Rubredoxin, pages 505–517. Wiley & Sons, 2001.
- [11] JEAN LE GALL. **A new species of desulfovibrio**. *J. Bacteriol.*, **86**:1120, 1963.
- [12] GERHARD FIALA AND KARL O. STETTER. ***Pyrococcus furiosus* sp. nov. represents a novel genus of marine heterotrophic archaeobacteria growing optimally**. *Arch. Microbiol.*, **145**:56–61, 1986.
- [13] S.R. ELSDEN, B.E. VOLCANI, F.M.C. GILCHRIST, AND D. LEWIS. **Properties of a fatty acid forming organism isolated from the rumen of sheep**. *J. Bacteriol.*, **72**:681–689:72:681–689, 1956.
- [14] C.-J. CHEN, Y.-H. LIN, Y.-C. HUANG, AND M.-Y. LIU. **Crystal structure of rubredoxin from *Desulfovibrio gigas* to ultra-high 0.68 Å resolution**. *Biochem. Biophys. Res. Commun.*, **349**:79–90, 2006.
- [15] R. BAU, D. C. REES, D. M. KURTZ, R. A. SCOTT, H. HUANG, M. W. W. ADAMS, AND M. K. EIDSSNESS. **Crystal Structure of rubredoxin from *Pyrococcus furiosus* at 0.95 Å resolution, and the structures of N-terminal methionine and formylmethionine variants of Pf Rd. Contributions of N-terminal interactions to thermostability**. *J. Biol. Inorg. Chem.*, **3**:484–493, 1998.
- [16] PETER F. LINDLEY. *Handbook of Metalloproteins*, chapter Transferrins, pages 793–811. Wiley & Sons, 2001.
- [17] A. M. DOKTER, M. C. VAN HEMERT, C. M. IN 'T VELT, K. VAN DER HOEF, J. LUGTENBURG, H. A. FRANK, AND E. J. J. GROENEN. **Resonance Raman spectrum of all-trans spheroidene. DFT analysis and isotope labeling**. *J. Phys. Chem. A*, **106**:9463–9469, 2002.
- [18] A. C. WIRTZ, M. C. VAN HEMERT, J. LUGTENBURG, H.A. FRANK, AND E. J. J. GROENEN. **Two stereoisomers of spheroidene in the *Rhodobacter sphaeroides* R26 reaction center: A DFT analysis of resonance Raman spectra**. *Biophys. J.*, **93**:981–991, 2007.
- [19] O. Y. GRINBERG, A. A. DUBINSKII, V. F. SHUVALOV, L. G. ORANSKII, V. I. KUROCHKIN, AND Y. S. LEBEDEV. **Submillimeter EPR spectroscopy of free-radical**. *Dokl. Akad. Nauk*, **230**(4):884–887, 1976.
- [20] A. A. GALKIN, O. Y. GRINBERG, A. A. DUBINSKII, N. N. KABDIN, V. N. KRYMOV, V. I. KUROCHKIN, Y. S. LEBEDEV, L. G. ORANSKII, AND V. F. SHUVALOV. **EPR spectrometer in 2-mm range for chemical research**. *Instrum. Exp. Tech.*, **20**(4):1229–1233, 1977.
- [21] OLEG Y. GRINBERG AND ALEXANDER A. DUBINSKII. *Biological Magnetic Resonance 22 - Very high frequency (VHF) ESR/EPR*, chapter 1. The early years, pages 1–18. Kluwer Academic/Plenum Publishers, 2004.
- [22] W. BRYAN LYNCH, KEITH A. EARLE, AND JACK H. FREED. **1-mm wave ESR spectrometer**. *Rev. Sci. Instrum.*, **59**(8):1345–1351, 1988.
- [23] KEITH A. EARLE, DMITRY S. TИPIKIN, AND JACK H. FREED. **Far-infrared electron-paramagnetic-resonance spectrometer utilizing a quasioptical reflection bridge**. *Rev. Sci. Instrum.*, **67**(7):2502–2513, 1996.
- [24] F. MULLER, M.A. HOPKINS, N. CORON, M. GRYNBERG, L. C. BRUNEL, AND G. MARTINEZ. **A high magnetic field EPR spectrometer**. *Rev. Sci. Instrum.*, **60**(12):3681–3684, 1989.
- [25] A. L. BARRA, L. C. BRUNEL, AND J. B. ROBERT. **EPR spectroscopy at very high field**. *Chem. Phys. Lett.*, **165**(1):107–109, 1990.
- [26] PETR NEUGEBAUER AND ANNE-LAURE BARRA. **New cavity design for broad-band quasi-optical HF-EPR spectroscopy**. *Appl. Magn. Reson.*, **37**:833–843, 2010.
- [27] G. M. SMITH, J. C. G. LESURF, R. H. MITCHELL, AND P. C. RIEDI. **Quasi-optical cw mm-wave electron spin resonance spectrometer**. *Rev. Sci. Instrum.*, **69**(11):3924–3937, 1998.
- [28] MARTIN R. FUCHS, THOMAS F. PRISNER, AND KLAUS MÖBIUS. **A high-field/high-frequency heterodyne induction-mode electron paramagnetic resonance spectrometer operating at 360 GHz**. *Rev. Sci. Instrum.*, **70**(9):3681–3683, 1999.
- [29] M. ROHRER, J. KRZYSZYK, V. WILLIAMS, AND L.-C. BRUNEL. **Fabry-Pérot resonator for high-field multi-frequency ESR at millimetre and submillimetre wavelengths**. *Meas. Sci. Technol.*, **10**:275–284, 1999.

Bibliography

- [30] A. K. HASSAN, L. A. PARDI, J. KRZYSZEK, A. SIENKIEWICZ, P. GOY, M. ROHRER, AND L.-C. BRUNEL. **Ultrawide band multifrequency high-field EMR technique: a methodology for increasing spectroscopic information.** *J. Magn. Reson.*, **142**:300–312, 2000.
- [31] M. ROHRER, O. BRÜGMANN, B. KINZER, AND T. F. PRISNER. **High-field/high-frequency EPR spectrometer operating in pulsed and continuous-wave mode at 180 GHz.** *Appl. Magn. Reson.*, **21**:257–274, 2001.
- [32] H. BLOK, J. A. J. M. DISSELHORST, H. VAN DER MEER, S. B. ORLINSKII, AND J. SCHMIDT. **ENDOR spectroscopy at 275 GHz.** *J. Magn. Reson.*, **173**:49–53, 2005.
- [33] E. RELERSE, P. P. SCHMIDT, G. KLIHM, AND W. LUBITZ. **A cw and pulse EPR spectrometer operating at 122 and 244 GHz using a quasi-optical bridge and a cryogen-free 12 T superconducting magnet.** *Appl. Magn. Reson.*, **31**:611–626, 2007.
- [34] KLAUS MÖBIUS AND ANTON SAVITSKY. *High-field EPR spectroscopy on proteins and their model systems - Characterization of transient paramagnetic states*, chapter 3. Instrumentation, pages 124–194. The Royal Society of Chemistry, Cambridge, 2009.
- [35] E. RELERSE. **High-frequency EPR instrumentation.** *Appl. Magn. Reson.*, **37**:795–818, 2010.
- [36] G. FEHER. **Sensitivity considerations in microwave paramagnetic resonance absorption techniques.** *Bell Syst. Tech. J.*, pages 449–484, March 1957.
- [37] CHARLES P. POOLE, JR. *Electron Spin Resonance - A comprehensive treatise on experimental techniques*. John Wiley & Sons, 1983.
- [38] G. R. EATON, S. S. EATON, AND G. A. RINARD. *Spatially Resolved Magnetic Resonance*, chapter Frequency dependence of EPR Sensitivity, pages 65–74. Wiley-VCH, 1998.
- [39] GEORGE A. RINARD, RICHARD W. QUINE, JAMES R. HARBRIDGE, RUITIAN SON, GARETH R. EATON, AND SANDRA S. EATON. **Frequency dependence of EPR signal-to-noise.** *J. Magn. Reson.*, **140**:218–227, 1999.
- [40] JAMES S. HYDE. *Foundations of Modern EPR*, chapter K.1. EPR at Varian: 1954–1974, pages 695–716. World Scientific, 1997.
- [41] DAVID E. BUDIL AND KEITH A. EARLE. *Biological Magnetic Resonance 22 - Very high frequency (VHF) ESR/EPR*, chapter 11. Sample Resonators for Quasioptical EPR, pages 353–399. Kluwer Academic/Plenum Publishers, 2004.
- [42] DALE T. TEANEY, M. P. KLEIN, AND A. M. PORTIS. **Microwave Superheterodyne Induction Spectrometer.** *Rev. Sci. Instrum.*, **32**(6):721–729, 1961.
- [43] K. KRISTOFFER ANDERSSON AND ANNE-LAURE BARRA. **The use of high field/frequency EPR in studies of radical and metal sites in proteins and small inorganic models.** *Spectrochim. Acta, Part A*, **58**:1101–1112, 2002.
- [44] K. KRISTOFFER ANDERSSON, PETER P. SCHMIDT, BETTINA KATTELE, KARI R. STRAND, AMY E. PALMER, SANG-KYU LEE, EDWARD I. SOLOMON, ASTRID GRÄSLUND, AND ANNE-LAURE BARRA. **Examples of high-frequency EPR studies in bioinorganic chemistry.** *J. Biol. Inorg. Chem.*, **8**:235–247, 2003.
- [45] ANNE-LAURE BARRA, ASTRID GRÄSLUND, AND K. KRISTOFFER ANDERSSON. *Biological Magnetic Resonance 22 - Very high frequency (VHF) ESR/EPR*, chapter 5. The use of very high frequency EPR (VHF-EPR) in studies of radicals and metal sites in proteins and small inorganic models, pages 145–163. Kluwer Academic/Plenum Publishers, 2004.
- [46] MICHEL FREY, LARRY SIEKER, FRANCOISE PAYAN, RICHARD HASER, MIREILLE BRUSCHI, GERARD PEPE, AND JEAN LEGALL. **Rubredoxin from *Desulfovibrio gigas* - A molecular model of the oxidized form at 1.4 Å resolution.** *J. Mol. Biol.*, **197**:525–541, 1987.
- [47] RUI M. ALMEIDA, SOFIA R. PAULETA, ISABEL MOURA, AND JOSÉ J. G. MOURA. **Rubredoxin as a paramagnetic relaxation-inducing probe.** *J. Inorg. Biochem.*, **103**(9), 2009.
- [48] MICHAEL W. DAY, BARBARA T. HSU, LEEMOR JOSHUA-TOR, JAE-BUM PARK, ZHI HAO ZHOU, MICHAEL W. W. ADAMS, AND DOUGLAS C. REES. **X-ray crystal structures of the oxidized and reduced forms of the rubredoxin from the marine hyperthermophilic archaeobacterium *Pyrococcus furiosus*.** *Protein Sci.*, **1**:1494–1507, 1992.
- [49] P. R. BLAKE, J. B. PARK, F. O. BRYANT, S. AONO, J. K. MAGNUSON, E. ECCLESTON, J. B. HOWARD, M. F. SUMMERS, AND M. W. W. ADAMS. **Determinants of protein hyperthermostability: purification and amino acid sequence of rubredoxin from the hyperthermophilic archaeobacterium *Pyrococcus furiosus* and secondary structure of the zinc adduct by NMR.** *Biochemistry*, **30**:10885–10891, 1991.
- [50] S. G. MAYHEW AND J. L. PEEL. **Rubredoxin from *Peptostreptococcus elsdenii*.** *Biochem. J.*, **100**:80, 1966.
- [51] LUCA A. PARDI, J. KRZYSZEK, JOSHUA TELSER, AND LOUIS-CLAUDE BRUNEL. **Multifrequency EPR spectra of molecular oxygen in solid air.** *J. Magn. Reson.*, **146**:375–378, 2000.
- [52] W. E. BLUMBERG AND J. PEISACH. **The measurement of zero field splitting and the determination of ligand composition in mononuclear nonheme iron proteins.** *Ann. N. Y. Acad. Sci.*, **222**:539–560, 1973.
- [53] CHRISTOPHER BULL, GREGORY J. MCCLUNE, AND JAMES A. FEE. **The mechanism of Fe-EDTA catalyzed superoxide dismutation.** *J. Am. Chem. Soc.*, **105**:5290–5300, 1983.
- [54] SATOSHI FUJII, HIROAKI OHYA-NISHIGUCHI, AND NOBORU HIROTA. **EPR evidence of intermediate peroxo complexes formed in a SOD model system.** *Inorg. Chim. Acta*, **175**:27–30, 1990.
- [55] ROLAND AASA. **Powder line shapes in the electron paramagnetic resonance spectra of high-spin ferric complexes.** *J. Chem. Phys.*, **52**:3919–3930, 1970.
- [56] J. PEISACH, W. E. BLUMBERG, E. T. LODE, AND M. J. COON. **An analysis of the electron paramagnetic resonance spectrum of *Pseudomonas oleovorans* rubredoxin.** *J. Biol. Chem.*, **246**:5877–5881, 1971.
- [57] I. MOURA, A. V. XAVIER, R. CAMMACK, M. BRUSCHI, AND J. LE GALL. **A comparative spectroscopic study of two non-haem iron proteins lacking labile sulphur from *Desulfovibrio gigas*.** *Biochim. Biophys. Acta*, **533**(1):156–162, 1978.
- [58] BIRGIT BÖRGER AND DIETER SUTER. **Magnetic and optical anisotropy of *Clostridium pasteurianum* rubredoxin from optically detected electron paramagnetic resonance.** *J. Phys. Chem.*, **115**(21):9821–9826, 2001.
- [59] A.L. BARRA, A.K. HASSAN, A. JANOSCHKA, C. L. SCHMIDT, AND V. SCHÜNEMANN. **Broad-band quasi-optical HF-EPR spectroscopy: Application to the study of the ferrous iron center from a rubredoxin mutant.** *Appl. Magn. Reson.*, **30**:385–397, 2006.
- [60] ROLAND MEIER AND FRANK W. HEINEMANN. **Structures of the spontaneously resolved six-coordinate potassium chloro-(ethylenediaminetriacetato acetic acid) iron(III) monohydrate and the seven-coordinate potassium (ethylenediaminetetracetato) iron(III) sesquihydrate.** *Inorg. Chim. Acta*, **337**:317–327, 2002.

- [61] K. MÖBIUS, A. SAVITSKY, A. SCHNEGG, M. PLATO, AND M. FUCHS. **High-field EPR spectroscopy applied to biological systems: Characterization of molecular switches for electron and ion transfer.** *Phys. Chem. Chem. Phys.*, **7**:19–42, 2005.
- [62] EDWARD I. SOLOMON. **Preface Forum: “Functional Insight from Physical Methods on Metalloenzymes”.** *Inorg. Chem.*, **44**:723–726, 2005.
- [63] SABINE VAN DOORSLAER AND EVI VINCK. **The strength of EPR and ENDOR techniques in revealing structure-function relationships in metalloproteins.** *Phys. Chem. Chem. Phys.*, **9**:4620–4638, 2007.
- [64] G. MATHIES, H. BLOK, J.A.J.M. DISSELHORST, P. GAST, H. VAN DER MEER, D.M. MIEDEMA, R.M. ALMEIDA, J.J.G. MOURA, W.R. HAGEN, AND E.J.J. GROENEN. **Continuous-wave EPR at 275 GHz: Application to high-spin Fe^{3+} systems.** *J. Magn. Reson.*, **210**:126–132, 2011.
- [65] I. MOURA, M. BRUSCHI, J. LE GALL, J. J. G. MOURA, AND A. V. XAVIER. **Isolation and Characterization of Desulforedoxin, a New Type of Non-Heme Iron Protein from *Desulfovibrio gigas*.** *Biochem. Biophys. Res. Comm.*, **75**:1037–1044, 1977.
- [66] MARGARIDA ARCHER, ROBERT HUBER, PEDRO TAVARES, ISABEL MOURA, JOSÉ J. G. MOURA, MARIA A. CARRONDO, LARRY C. SIEKER, JEAN LE GALL, AND MARIA J. ROMAO. **Crystal Structure of Desulforedoxin from *Desulfovibrio gigas* Determined at 1.8 Å Resolution: A Novel Non-heme Iron Protein Structure.** *J. Mol. Biol.*, **251**:690–702, 1995.
- [67] M. BRUSCHI, I. MOURA, J. LE GALL, A. V. XAVIER, L. C. SIERER, G. BOVIER-LAPIERRE, J. BONICEL, AND P. COUCHOUD. **The Amino Acid Sequence Of Desulforedoxin, A New Type of Non Heme Iron Protein From *Desulfovibrio gigas*.** *Biochem. Biophys. Res. Comm.*, **90**:596–605, 1979.
- [68] RAYMOND A. BAIR AND WILLIAM A. GODDARD. **Theoretical Studies of the Ground and Excited States of a Model of the Active Site in Oxidized and Reduced Rubredoxin.** *J. Am. Chem. Soc.*, **100**:5669–5676, 1978.
- [69] NORIKAZU UYAMA, TAKASHI SUGAWARA, KAZUYUKI TATSUMI, AND AKIRA NAKAMURA. **Control of Fe-S Bond Character by the Variation of Fe-S Torsion Angles in the Iron(III) Site of Rubredoxin.** *Inorg. Chem.*, **26**:1978–1981, 1987.
- [70] VLADISLAV V. VRAJMASU, ECKARD MÜNCK, AND EMILE L. BOMINAAR. **Theoretical Analysis of the Three-Dimensional Structure of Tetrathiolato Iron Complexes.** *Inorg. Chem.*, **43**:4867–4879, 2004.
- [71] JOSEPH C. DEATON, MATTHEW S. GEBHARD, STEPHEN A. KOCH, MICHELLE MILLAR, AND EDWARD I. SOLOMON. **Ligand Field Transitions and the Origin of Zero Field Splitting in $[\text{PPh}_4][\text{FeCl}_4]$ and $[\text{NEt}_4][\text{Fe}(\text{SR})_4]$ ($\text{R} = 2,3,5,6\text{-Me}_4\text{C}_6\text{H}$): A Model for the High-Spin Fe(III) Site in Rubredoxin.** *J. Am. Chem. Soc.*, **110**:6241–6243, 1988.
- [72] JOSEPH C. DEATON, MATTHEW S. GEBHARD, AND EDWARD I. SOLOMON. **Transverse and Longitudinal Zeeman Effect on $[\text{PPh}_4][\text{FeCl}_4]$: Assignment of the Ligand Field Transitions and the Origin of the ${}^6\text{A}_1$ Ground-State Zero-Field Splitting.** *Inorg. Chem.*, **28**:877–889, 1989.
- [73] MATTHEW S. GEBHARD, JOSEPH C. DEATON, STEPHEN A. KOCH, MICHELLE MILLAR, AND EDWARD I. SOLOMON. **Single-Crystal Spectral Studies of $\text{Fe}(\text{SR})_4$ [$\text{R} = 2,3,5,6\text{-Me}_4\text{C}_6\text{H}$]: The Electronic Structure of the Ferric Tetrathiolate Active Site.** *J. Am. Chem. Soc.*, **112**:2217–2231, 1990.
- [74] MICHELLE MILLAR, JOE F. LEE, TIMOTHY O’SULLIVAN, STEPHEN A. KOCH, AND RONALD FIKAR. **Models for the iron-sulfur protein rubredoxin: the use of sterically hindered thiolate ligands to stabilize $[\text{Fe}(\text{SR})_4]^{1-}$ complexes; some considerations of the structure of the $[\text{Fe}(\text{S-Cys})_4]$ centers in oxidized rubredoxins.** *Inorg. Chim. Acta*, **243**:333–343, 1996.
- [75] KOUICHI FUKUI, HIROAKI OHYA-NISHIGUCHI, AND NOBORU HIROTA. **ESR and Magnetic Susceptibility Studies on High-Spin Tetrahedral Cobalt(II)-Thiolate Complexes: An Approach to Rubredoxin-Type Active Sites.** *Bull. Chem. Soc. Jpn.*, **64**:1205–1212, 1991.
- [76] KOUICHI FUKUI, NORIMICHI KOJIMA, HIROAKI OHYA-NISHIGUCHI, AND NOBORU HIROTA. **Metal-Thiolate Bonding Properties: Single-Crystal ESR, Susceptibility, and Polarized Absorption Evidence for a Strong π Interaction in Tetrakis (thiophenolato)cobaltate(II).** *Inorg. Chem.*, **31**:1338–1344, 1992.
- [77] KOUICHI FUKUI, HIDEKI MASUDA, HIROAKI OHYA-NISHIGUCHI, AND HITOSHI KAMADA. **Effects of Co-S torsion angle variation in a cobalt(II)-thiolate complex: X-ray crystal structure analysis, single-crystal EPR measurements and ligand-field calculations.** *Inorg. Chim. Acta*, **238**:73–81, 1995.
- [78] SILVIA SOTTINI, GUINEVERE MATHIES, PETER GAST, DIMITRIOS MAGANAS, PANAYOTIS KYRITSIS, AND EDGAR J. J. GROENEN. **A W-band pulsed EPR/ENDOR study of Co^{II}S_4 coordination in the $\text{Co}(\text{SPPH}_2)(\text{SPiPr}_2)\text{N}_2$ complex.** *Phys. Chem. Chem. Phys.*, **11**:6727–6732, 2009.
- [79] CHARLES J. WALSBY, DMITRIY KREPKIY, DAVID H. PETERING, AND BRIAN M. HOFFMAN. **Cobalt-Substituted Zinc Finger 3 of Transcription Factor IIIA: Interactions with Cognate DNA Detected by ${}^{31}\text{P}$ ENDOR Spectroscopy.** *J. Am. Chem. Soc.*, **125**:7502–7503, 2003.
- [80] ISABEL MOURA, BOI HANH HUYNH, ROBERT P. HAUSER, JEAN LE GALL, ANTONIO V. XAVIER, AND ECKARD MÜNCK. **Mossbauer and EPR Studies of Desulforedoxin from *Desulfovibrio gigas*.** *J. of Biol. Chem.*, **255**:2493–2498, 1980.
- [81] ISABEL MOURA, MIGUEL TEIXEIRA, JEAN LE GALL, AND JOSÉ J. G. MOURA. **Spectroscopic Studies of Cobalt and Nickel Substituted Rubredoxin and Desulforedoxin.** *J. of Inorg. Biochem.*, **44**:127–139, 1991.
- [82] J. A. J. M. DISSELHORST, H. VAN DER MEER, O. G. POLUEKTOV, AND J. SCHMIDT. **A Pulsed EPR and ENDOR spectrometer Operating at 95 GHz.** *J. Magn. Reson. Series A*, **115**:183–188, 1995.
- [83] PEDRO TAVARES, JOHN K. WUNDERLICH, STEVEN G. LLOYD, JEAN LE GALL, JOSE J. G. MOURA, AND ISABEL MOURA. **Total synthesis of a simple metalloprotein - Desulforedoxin.** *Biochem. Biophys. Res. Comm.*, **208**:680–687, 1995.
- [84] LUCIA BIANCI, ALESSANDRO BENCINI, CRISTIANO BENELLI, DANTE GATTESCHI, AND CLAUDIA ZANCHINI. **Spectral-Structural Correlations in High-Spin Cobalt(II) Complexes.** *Struct. Bonding*, **52**:37–86, 1982.
- [85] H. DRULIS, K. DYREK, K. P. HOFFMANN, S. K. HOFFMANN, AND A. WESELUCHA-BIRCZYNSKA. **EPR Spectra of Low-Symmetry Tetrahedral High-Spin Cobalt (II) in a Cinchoninium Tetrachlorocobaltate(II) Dihydrate Single Crystal.** *Inorg. Chem.*, **24**:4009–4012, 1985.
- [86] AN-SUEI YANG AND BETTY JEAN GAFFNEY. **Determination of relative spin concentration in some high-spin ferric proteins using E/D -distribution in electron paramagnetic resonance simulations.** *Biophys. J.*, **51**:55–67, 1987.
- [87] A. ABRAGAM AND M. H. L. PRYCE. **Theory of the nuclear hyperfine structure of paramagnetic resonance spectra in crystals.** *Proc. Roy. Soc. London*, **A205**:135–153, 1951.

Bibliography

- [88] J. P. JESSON. **Analysis of the Paramagnetic Resonance and Optical Spectra of $d^{3,7}$ Ions in Tetragonal Crystal Fields. I. Orbitally Nondegenerate Ground States.** *J. Chem. Phys.*, **48**:161–168, 1968.
- [89] M. H. L. PRYCE. **A Modified Perturbation Procedure for a Problem in Paramagnetism.** *Proc. Roy. Soc. London*, **A63**:25–29, 1950.
- [90] A. BENCINI AND D. GATTESCHI. **Electron Spin Resonance Spectra of Low-Symmetry Pseudotetrahedral High-Spin Cobalt(II) Complexes. Tetra-*n*-butylammonium Tribromo(quinoline)cobaltate(II).** *Inorg. Chem.*, **16**:2141–2142, 1977.
- [91] H. G. BELJERS, P. F. BONGERS, R. P. VAN STAPELE, AND H. ZIJLSTRA. **A direct measurement of the large zero field splitting of Co^{2+} in Cs_3CoCl_5 .** *Phys. Letters*, **12**(2):81–82, 1964.
- [92] R. P. VAN STAPELE, H. G. BELJERS, P. F. BONGERS, AND H. ZIJLSTRA. **Ground State of Divalent Co Ions in Cs_3CoCl_5 and Cs_3CoBr_5 .** *J. Chem. Phys.*, **44**(10):3719–3725, 1966.
- [93] J. KRZYSZEK, S. A. ZVYAGIN, ANDREW OZAROWSKI, ADAM T. FIEDLER, THOMAS C. BRUNOLD, AND JOSHUA TELSER. **Definitive Spectroscopic Determination of Zero-Field Splitting in High-Spin Cobalt(II).** *J. Am. Chem. Soc.*, **126**:2148–2155, 2004.
- [94] J. KRZYSZEK, DALE C. SWENSON, S. A. ZVYAGIN, DMITRY SMIRNOV, ANDREW OZAROWSKI, AND JOSHUA TELSER. **Cobalt(II) “Scorpionate” Complexes as Models for Cobalt-Substituted Zinc Enzymes: Electronic Structure Investigation by High-Frequency and -Field Electron Paramagnetic Resonance Spectroscopy.** *J. Am. Chem. Soc.*, **132**:5241–5253, 2010.
- [95] VLADISLAV V. VRAJMASU, EMILE L. BOMINAAR, JACQUES MEYER, AND ECKARD MÜNCK. **Mössbauer Study of Reduced Rubredoxin As Purified and in Whole Cells. Structural Correlation Analysis of Spin Hamiltonian Parameters.** *Inorg. Chem.*, **41**:6358–6371, 2002.
- [96] MEGAN MAHER, MADDALENA CROSS, MATTHEW C. J. WILCE, J. MITCHELL GUSS, AND ANTHONY G. WEDD. **Metal-substituted derivatives of the rubredoxin from *Clostridium pasteurianum*.** *Acta Crystallogr., Sect. D*, **60**:298–303, 2004.
- [97] DIMITRIOS MAGANAS, SILVIA SOTTINI, PANAYOTIS KYRITSIS, EDGAR J. J. GROENEN, AND FRANK NEESE. **Theoretical Analysis of the Spin Hamiltonian Parameters in $Co(II)S_4$ Complexes, Using Density Functional Theory and Correlated ab initio Methods.** *Inorg. Chem.*, **50**:8741–8754, 2011.
- [98] EDWARD I. SOLOMON, THOMAS C. BRUNOLD, MINDY I. DAVIS, JYLIAN N. KEMSLEY, SANG-KYU LEE, NICOLAI LEHNERT, FRANK NEESE, ANDREW J. SKULAN, YI-SHAN YANG, AND JING ZHOU. **Geometric and Electronic Structure/Function Correlations in Non-Heme Iron Enzymes.** *Chem. Rev.*, **100**:235–349, 2000.
- [99] J. J. R. FRAUSTO DA SILVA AND R. J. P. WILLIAMS. *The Biological Chemistry of the Elements.* Oxford University Press, 2001.
- [100] EDWARD I. SOLOMON, SERGE I. GORELSKY, AND ABISHEK DEY. **Metal-Thiolate Bonds in Bioinorganic Chemistry.** *J. Comput. Chem.*, **27**:1415–1428, 2006.
- [101] AKIMASA MIYANAGA, SHINYA FUSHINOBU, KIYOSHI ITO, AND TAKAYOSHI WAKAGI. **Crystal Structure of Cobalt-Containing Nitrile Hydratase.** *Biochem. Biophys. Res. Commun.*, **288**:1169–1174, 2001.
- [102] OLGA YU. GAVEL, SERGEY A. BURSAKOV, JUAN J. CALVETE, GRHAM N. GEORGE, JOSÉ J. G. MOURA, AND ISABEL MOURA. **ATP Sulfurylases from Sulfate-Reducing Bacteria of the Genus *Desulfovibrio*. A Novel Metalloprotein Containing Cobalt and Zinc.** *Biochemistry*, **37**:16225–16232, 1998.
- [103] CHRISTOPHER J. CARRELL, XIAOTANG WANG, LIMEI JONES, WILLIAM L. JARRETT, VICTOR L. DAVIDSON, AND F. SCOTT MATHEWS. **Crystallographic and NMR Investigation of Cobalt-Substituted Amicyanin.** *Biochemistry*, **43**:9381–9389, 2004.
- [104] AMY B. GHERING, JACOB E. SHOKES, ROBERT A. SCOTT, JAMES G. OMICHINSKI, AND HILARY A. GODWIN. **Spectroscopic Determination of the Thermodynamics of Cobalt and Zinc Binding to GATA Proteins.** *Biochemistry*, **43**:8346–8355, 2004.
- [105] ESTEVAO A. PEROZA AND EVA FREISINGER. **Metal ion binding properties of *Tricium aestivum* E_c -1 metallothionein: evidence supporting two separate metal thiolate clusters.** *J. Biol. Inorg. Chem.*, **12**:377–391, 2007.
- [106] JULIE A. KOVACS. **Synthetic Analogues of Cysteinate-Ligated Non-Heme Iron and Non-Corrinoid Cobalt Enzymes.** *Chem. Rev.*, **104**:825–848, 2004.
- [107] OLEG Y. GRINBERG AND LAWRENCE J. BERLINER EDS. *Biological Magnetic Resonance 22 - Very high frequency (VHF) ESR/EPR.*
- [108] DIMITRIOS MAGANAS, SARAH S. STANILAND, ALEXIOS GRIGORPOULOS, FRASER WHITE, SIMON PARSONS, NEIL ROBERTSON, PANAYOTIS KYRITSIS, AND GEORGIOS PNEUMATIKAKIS. **Structural, spectroscopic and magnetic properties of $M[R_2P(E)NP(E)R'_2]_2$ complexes, $M = Co, Mn, E = S, Se$ and $R, R' = Ph$ or iPr . Covalency of MS bonds from experimental data and theoretical calculations.** *Dalton Trans.*, pages 2301–2315, 2006.
- [109] N. M. ATHERTON. *Principles of Electron Spin Resonance.* Ellis Horwood PTR Prentice Hall, 1993.
- [110] SILVIA SOTTINI AND EDGAR J. J. GROENEN. **A comment on the pseudo-nuclear Zeeman effect.** *Submitted to J. Magn. Reson.*, 2012.
- [111] M. T. BENNEBROEK AND J. SCHMIDT. **Pulsed ENDOR Spectroscopy at Large Thermal Spin Polarizations and the Absolute Sign of the Hyperfine Interaction.** *J. Magn. Reson.*, **128**:199–206, 1997.
- [112] B. EPEL, A. PÖPPL, P. MANIKANDAN, S. VEGA, AND D. GOLDFARB. **The Effect of Spin Relaxation on ENDOR Spectra Recorded at High Magnetic Fields and Low Temperatures.** *J. Magn. Reson.*, **148**:388–397, 2001.
- [113] RICHARD H. HOLM, PIERRE KENNEPOHL, AND EDWARD I. SOLOMON. **Structural and Functional Aspects of Metal Sites in Biology.** *Chem. Rev.*, **96**:2239–2314, 1996.
- [114] WILFRED R. HAGEN. **EPR of non-Kramers doublets in biological systems - Characterization of an $S = 2$ system in oxidized cytochrome c oxidase.** *Biochim. Biophys. Acta*, **708**:82–98, 1982.
- [115] MICHAEL P. HENDRICH AND PETER G. DEBRUNNER. **EPR Spectra of Quintet Ferrous Myoglobin and a Model Heme Compound.** *J. Magn. Reson.*, **78**:133–141, 1988.
- [116] MICHAEL P. HENDRICH AND PETER G. DEBRUNNER. **Integer-spin electron paramagnetic resonance of iron proteins.** *Biophys. J.*, **56**:489–506, 1989.
- [117] MARK T. WERTH, JR. DONALD M. KURTZ, BARRY D. HOWES, AND BOI HANH HUYNH. **Observation of $S = 2$ EPR Signals from Ferrous Iron-Thiolate Complexes. Relevance to Rubredoxin-Type Sites in Proteins.** *Inorg. Chem.*, **28**:1357–1361, 1989.

- [118] J. KRZYSTEK, ANDREW OZAROWSKI, AND JOSHUA TELSER. **Multi-frequency, high-field EPR as a powerful tool to accurately determine zero-field splitting in high-spin transition metal coordination complexes.** *Coord. Chem. Rev.*, **250**:2308–2324, 2006.
- [119] MICHAEL J. KNAPP, J. KRZYSTEK, LOUIS-CLAUDE BRUNEL, AND DAVID N. HENDRICKSON. **High-Frequency EPR Study of the Ferrous Ion in the Reduced Rubredoxin Model [Fe(SPh)₄]²⁻.** *Inorg. Chem.*, **39**:281–288, 2000.
- [120] GRAHAM CARVER, PHILIP L. W. TREGENNA-PIGGOTT, ANNE-LAURE BARRA, ANTONIA NEELS, AND JOHN A. STRIDE. **Spectroscopic and Structural Characterization of the [Fe(imidazole)₆]²⁺ Cation.** *Inorg. Chem.*, **42**:5771–5777, 2003.
- [121] ANDREW OZAROWSKI, S. A. ZVYAGIN, WILLIAM M. REIFF, JOSHUA TELSER, LOUIS-CLAUDE BRUNEL, AND J. KRZYSTEK. **High-Frequency and -Field EPR of a Pseudo-octahedral Complex of High-Spin Fe(II): Bis(2,2'-bi-2-thiazoline)bis(isothiocyanato)iron(II).** *J. Am. Chem. Soc.*, **126**:6574–6575, 2004.
- [122] JOSHUA TELSER, JORIS VAN SLAGEREN, SURIYAKAN VONTRAGOOL, MARTIN DRESSEL, WILLIAM M. REIFF, S. A. ZVYAGIN, ANDREW OZAROWSKI, AND J. KRZYSTEK. **High-frequency/high-field EPR spectroscopy of the high-spin ferrous ion in hexaaqua complexes.** *Magn. Reson. Chem.*, **43**:S130–S139, 2005.
- [123] J. KRZYSTEK, S.A. ZVYAGIN, ANDREW OZAROWSKI, S. TROFIMENKO, AND JOSHUA TELSER. **Tunable-frequency high-field electron paramagnetic resonance.** *J. Magn. Reson.*, **178**:174–183, 2006.
- [124] GRAHAM CARVER, CHRISTOPHER DOBE, THOMAS B. JENSEN, PHILIP L. W. TREGENNA-PIGGOTT, STEFAN JANSSEN, ECKHARD BILL, GARRY J. MCINTYRE, AND ANNE-LAURE BARRA. **Spectroscopic, Magnetochemical, and Crystallographic Study of Cesium Iron Phosphate Hexahydrate: Characterization of the Electronic Structure of the Iron(II) Hexa-aqua Cation in a Quasicubic Environment.** *Inorg. Chem.*, **45**:4695–4705, 2006.
- [125] SUSHIL K. MISRA, STEFAN DIEHL, DMITRY TIPIKIN, AND JACK H. FREED. **A multi-frequency EPR study of Fe²⁺ and Mn²⁺ ions in a ZnSiF₆·6H₂O single crystal at liquid-helium temperatures.** *J. Magn. Reson.*, **205**:14–22, 2010.
- [126] A. DAVISON AND ELLEN S. SWITKES. **The stereochemistry of four-coordinate bis(imidodiphosphinato)metal(II) chelate complexes.** *Inorg. Chem.*, **10**:837–842, 1971.
- [127] LIAM M. GILBY AND BRIAN PIGGOTT. **The synthesis and X-ray structure of cobalt(II) complexes of iminobis(phosphinochalcogenides), [CoN(XPR₂)₂-X,X'₂] (X = S or Se; R = Phe or Pr¹).** *Polyhedron*, **18**:1077–1082, 1999.
- [128] JOHN WILLIAMS. **The evolution of transferrin.** *Trends Biochem. Sci.*, **7**:394–397, 1982.
- [129] ARTHUR D. TINOCO, CYNTHIA W. PETERSON, BALDO LUCCHESI, ROBERT P. DOYLE, AND ANN M. VALENTINE. **On the evolutionary significance and metal-binding characteristics of a monolobal transferrin from *Ciona intestinalis*.** *Proc. Natl. Acad. Sci.*, **105**:3268–3273, 2008.
- [130] J. V. PRINCIOOTTO AND E. J. ZAPOLSKI. **Difference between the two iron-binding sites of transferrin.** *Nature*, **255**:87–88, 1975.
- [131] PHILIP AISEN, ADELA LEIBMAN, AND JAY ZWEIER. **Stoichiometric and Site Characteristics of the Binding of Iron to Human Transferrin.** *J. Biol. Chem.*, **253**:1930–1937, 1978.
- [132] LUNG-NAN LIN, ANNE B. MASON, ROBERT C. WOODWORTH, AND JOHN F. BRANDTS. **Calorimetric Studies of Serum Transferrin and Ovotransferrin. Estimates of Domain Interactions, and Study of the Kinetic Complexities of Ferric Ion Binding.** *Biochemistry*, **33**:1881–1888, 1994.
- [133] OLGA ZAK AND PHILIP AISEN. **Iron Release from Transferrin, Its C-Lobe, and Their Complexes with Transferrin Receptor: Presence of N-Lobe Accelerates Release from C-Lobe at Endosomal pH.** *Biochemistry*, **42**:12330–12334, 2003.
- [134] DMITRY R. GUMEROV, ANNE B. MASON, AND IGOR A. KALTASHOV. **Interlobe Communication in Human Serum Transferrin: Metal Binding and Conformational Dynamics Investigated by Electrospray Ionization Mass Spectrometry.** *Biochemistry*, **42**:5421–5428, 2003.
- [135] DAVID H. HAMILTON, ISABELLE TURCOT, ALAIN STINTZI, AND KENNETH N. RAYMOND. **Large cooperativity in the removal of iron from transferrin at physiological temperature and chloride ion concentration.** *J. Biol. Inorg. Chem.*, **9**:936–944, 2004.
- [136] SHAINA L. BYRNE AND ANNE B. MASON. **Human serum transferrin: a tale of two lobes. Urea gel and steady state fluorescence analysis of recombinant transferrins as a function of pH, time, and the soluble portion of the transferrin receptor.** *J. Biol. Inorg. Chem.*, **14**:771–781, 2009.
- [137] ROLAND AASA, BO G. MALMSTRÖM, PAUL SALTMAN, AND TORE VÄNNGÅRD. **The Specific Binding of Iron(III) and Copper(II) to Transferrin and Conalbumin.** *Biochim. Biophys. Acta*, **75**:203–222, 1963.
- [138] R. D. DOWSING AND J. F. GIBSON. **Electron Spin Resonance of High-Spin d⁵ Systems.** *J. Chem. Phys.*, **50**:294–303, 1969.
- [139] RICHARD A. PINKOWITZ AND PHILIP AISEN. **Zero-Field Splittings of Iron Complexes of Transferrin.** *J. Biol. Chem.*, **247**:7830–7834, 1972.
- [140] ROLAND AASA. **Re-interpretation of the Electron Paramagnetic Resonance Spectra of Transferrins.** *Biophys. Biochem. Res. Comm.*, **49**:806–812, 1972.
- [141] M. I. SCULLANE, L. K. WHITE, AND N. D. CHASTEEN. **An Efficient Approach to Computer Simulation of EPR Spectra of High-Spin Fe(III) in Rhombic Ligand Fields.** *J. Magn. Reson.*, **47**:383–397, 1982.
- [142] E. MARGARET PRICE AND J. F. GIBSON. **Electron Paramagnetic Resonance Evidence for a Distinction between the Two Iron-binding Sites in Transferrin and in Conalbumin.** *J. Biol. Chem.*, **24**:8031–8035, 1972.
- [143] JOHN K. GRADY, ANNE B. MASON, ROBERT C. WOODWORTH, AND N. DENNIS CHASTEEN. **The effect of salt and site-directed mutations on the iron(III)-binding site of human serum transferrin as probed by EPR spectroscopy.** *Biochem. J.*, **309**:403–410, 1995.
- [144] PHILIP AISEN, RICHARD A. PINKOWITZ, AND ADELA LEIBMAN. **EPR and Other Studies of the Anion-Binding Sites of Transferrin.** *Ann. New York Acad. Sci.*, pages 337–346, 1973.
- [145] JEAN DUBACH, BETTY JEAN GAFFNEY, KUNDALIKA MORE, GARETH R. EATON, AND SANDRA S. EATON. **Effect of the synergistic anion on electron paramagnetic resonance spectra of iron-transferrin anion complexes is consistent with bidentate binding of the anion.** *Biophys. J.*, **59**:1091–1100, 1991.
- [146] B. J. GAFFNEY, B. C. MAGUIRE, R. T. WEBER, AND G. G. MARESH. **Disorder at metal sites in proteins: a high-frequency EMR study.** *Appl. Magn. Reson.*, **16**:207–221, 1999.

Bibliography

- [147] DONALD A. FOLAJTAR AND N. DENNIS CHASTEEN. **Measurement of Nonsynergistic Anion Binding to Transferrin by EPR Difference Spectroscopy.** *J. Am. Chem. Soc.*, **104**:5775–5780, 1982.
- [148] QING-YU HE, ANNE B. MASON, ROBERT C. WOODWORTH, BEATRICE M. TAM, ROSS T. A. MACGILLIVRAY, JOHN K. GRADY, AND N. DENNIS CHASTEEN. **Inequivalence of the Two Tyrosine Ligands in the N-Lobe of Human Serum Transferrin.** *Biochemistry*, **36**:14853–14860, 1997.
- [149] QING-YU HE, ANNE B. MASON, ROWCHANAK PAKDAMAN, N. DENNIS CHASTEEN, BONNIE K. DIXON, BEATRICE M. TAM, VINH NGUYEN, ROSS T. A. MACGILLIVRAY, AND ROBERT C. WOODWORTH. **Mutations at the Histidine 249 Ligand Profoundly Alter the Spectral and Iron-Binding Properties of Human Serum Transferrin N-Lobe.** *Biochemistry*, **39**:1205–1210, 2000.
- [150] ANNE B. MASON, PETER J. HALBROOKS, NICHOLAS G. JAMES, SUSAN A. CONNOLLY, JULIA R. LAROUCHE, VALERIE C. SMITH, ROSS T. A. MACGILLIVRAY, AND N. DENNIS CHASTEEN. **Mutational Analysis of C-Lobe Ligands of Human Serum Transferrin: Insights into the Mechanism of Iron Release.** *Biochemistry*, **44**:8013–8021, 2005.
- [151] ANNE B. MASON, PETER J. HALBROOKS, NICHOLAS G. JAMES, SHAINA L. BYRNE, JOHN K. GRADY, N. DENNIS CHASTEEN, CEDRIC E. BOBST, IGOR A. KALTASHOV, VALERIE C. SMITH, ROSS T. A. MACGILLIVRAY, AND STEPHEN J. EVERSE. **Structural and Functional Consequences of the Substitution of Glycine 65 with Arginine in the N-Lobe of Human Transferrin.** *Biochemistry*, **48**:1945–1953, 2009.
- [152] ANNE B. MASON, PETER J. HALBROOKS, JULIA R. LAROUCHE, SARA K. BRIGGS, MARQUE L. MOFFETT, JON E. RAMSEY, SUSAN A. CONNOLLY, VALERIE C. SMITH, AND ROSS T.A. MACGILLIVRAY. **Expression, purification, and characterization of authentic monoferric and apo-human serum transferrins.** *Prot. Expr. Purif.*, **36**:318–326, 2004.
- [153] G. FEHER, J.P. ALLEN, M.Y. OKAMURA, AND D.C. REES. **Structure and function of bacterial photosynthetic reaction centres.** *Nature*, **339**:111–116, 1989.
- [154] RICHARD J. COGDELL AND HARRY A. FRANK. **How carotenoids function in photosynthetic bacteria.** *Biochim. Biophys. Acta*, **895**:63, 1988.
- [155] HARRY A. FRANK AND RICHARD J. COGDELL. **Carotenoids in photosynthesis.** *Photochem. Photobiol.*, **63**(3):257–264, 1996.
- [156] HIDEKI HASHIMOTO, RITSUKO FUJII, KAZUHIRO YANAGI, TOSHIYUKI KUSUMOTO, ALASTAIR T. GARDINER, RICHARD J. COGDELL, ALEKSANDER W. ROSZAK, NEIL W. ISAACS, ZEUS PENDON, DARIUSZ NIEDZWIEDSKI, AND HARRY A. FRANK. **Structures and function of carotenoids bound to reaction centers from purple photosynthetic bacteria.** *Pure Appl. Chem.*, **78**(8):1505–1518, 2006.
- [157] MARC LUTZ, JACQUES KLEO, AND FRANCOISE REISS-HUSSON. **Resonance Raman scattering of bacteriochlorophyll, bacteriopheophytin and spheroidene in reaction centers of *Rhodospseudomonas spheroides*.** *Biochem. Biophys. Res. Commun.*, **69**(3):711–717, 1976.
- [158] MARC LUTZ, ILEANA AGALIDIS, GUY HERVO, RICHARD J. COGDELL, AND FRANCOISE REISS-HUSSON. **On the state of carotenoids bound to reaction centers of photosynthetic bacteria: a resonance Raman study.** *Biochim. Biophys. Acta*, **503**:287–303, 1978.
- [159] YASUSHI KOYAMA, MARIKO KITO, TOMOKO TAKII, KIYOSHI TSUKIDA, AND JINPEI YAMASHITA. **Configuration of the carotenoid in the reaction centers of photosynthetic bacteria - Comparison of the resonance Raman spectrum of the reaction center of *Rhodospseudomonas sphaeroides* G1C with those of *cis-trans* isomers of β -carotene.** *Biochim. Biophys. Acta*, **680**:109–118, 1982.
- [160] YASUSHI KOYAMA, TOMOKO TAKII, KAYOKO SAIKI, AND KIYOSHI TSUKIDA. **Configuration of the carotenoid in the reaction centers of photosynthetic bacteria. (2) Comparison of the resonance Raman lines of the reaction centers with those of the 14 different *cis-trans* isomers of β -carotene.** *Photobiochem. Photobiophys.*, **5**:139–150, 1983.
- [161] T. O. YEATES, H. KOMIYA, A. CHIRINO, D. C. REES, J. P. ALLEN, AND G. FEHER. **Structure of the reaction center from *Rhodobacter sphaeroides* R-26 and 2.4.1: Protein-cofactor (bacteriochlorophyll, bacteriopheophytin, and carotenoid) interactions.** *Proc. Natl. Acad. Sci. U.S.A.*, **85**:7993–7997, 1988.
- [162] B. ARNOUX, A. DUCRUI, F. REISS-HUSSON, M. LUTZ, J. NORRIS, M. SCHIFFER, AND C.-H. CHANG. **Structure of spheroidene in the photosynthetic reaction center from *Y Rhodobacter sphaeroides*.** *FEBS Lett.*, **258**(1):47–50, 1989.
- [163] ULRICH ERMILER, GÜNTER FRITZSCH, SUSAN K. BUCHANAN, AND HARTMUT MICHEL. **Structure of the photosynthetic reaction centre from *Rhodobacter sphaeroides* at 2.65 Å resolution: cofactors and protein-cofactor interactions.** *Structure*, **2**:925–936, 1994.
- [164] KATHERINE MCAULEY, PAUL K. FYFE, JUSTIN P. RIDGE, RICHARD J. COGDELL, NEIL W. ISAACS, AND MICHAEL R. JONES. **Ubiquinone binding, ubiquinone exclusion, and detailed cofactor conformation in a mutant bacterial reaction center.** *Biochemistry*, **39**:15032–15043, 2000.
- [165] ALEKSANDER W. ROSZAK, KIMBERLEY MCKENDRICK, ALASTAIR T. GARDINER, IAIN A. MITCHELL, NEIL W. ISAACS, RICHARD J. COGDELL, HIDEKI HASHIMOTO, AND HARRY A. FRANK. **Protein regulation of carotenoid binding: gatekeeper and locking amino acid residues in reaction centers of *Rhodobacter sphaeroides*.** *Structure*, **12**:765–773, 2004.
- [166] PETER KOK, JÜRGEN KÖHLER, EDGAR J.J. GROENEN, RONALD GEBHARD, INEKE VAN DER HOEF, JOHAN LUGTENBURG, ARNOLD J. HOFF, ROYA FARHOOSH, AND HARRY A. FRANK. **Towards a vibrational analysis of spheroidene. Resonance Raman spectroscopy of ^{13}C -labelled spheroidenes in petroleum ether and in the *Rhodobacter sphaeroides* reaction centre.** *Biochim. Biophys. Acta*, **1185**:188–192, 1994.
- [167] PETER KOK, JÜRGEN KÖHLER, EDGAR J.J. GROENEN, RONALD GEBHARD, INEKE VAN DER HOEF, JOHAN LUGTENBURG, ROYA FARHOOSH, AND HARRY A. FRANK. **Resonance Raman spectroscopy of ^2H -labelled spheroidenes in petroleum ether and in the *Rhodobacter sphaeroides* reaction centre.** *Spectrochim. Acta, Part A*, **53**:381–392, 1997.
- [168] BARRY W. CHADWICK AND HARRY A. FRANK. **Electron-spin resonance studies of carotenoids incorporated into reaction centers of *Rhodobacter sphaeroides* R26.1.** *Biochim. Biophys. Acta*, **851**:257–266, 1986.
- [169] ILEANA AGALIDIS, MARC LUTZ, AND FRANCOISE REISS-HUSSON. **Binding of carotenoids on reaction centers from *Rhodospseudomonas sphaeroides* R26.** *Biochim. Biophys. Acta*, **589**:264–274, 1980.
- [170] S. SHOCHAT, T. ARLT, C. FRANCKE, P. GAST, P. I. VAN NOORT, S. C. M. OTTE, H. P. M. SCHELVIS, S. SCHMIDT, E. VIJGENBOOM, J. VRIEZE, W. ZINTH, AND A. J. HOFF. **Spectroscopic characterization of reaction centers of the (M)Y210W mutant of the photosynthetic bacterium *Rhodobacter sphaeroides*.** *Photosynth. Res.*, **40**:55–66, 1994.
- [171] G. FEHER AND M. Y. OKAMURA. *The Photosynthetic Bacteria*, chapter 19. Chemical composition and properties of reaction centers, pages 349–386. Plenum Press New York, 1978.

- [172] M. J. FRISCH, G. W. TRUCKS, H. B. SCHLEGEL, G. E. SCUERIA, M. A. ROBB, J. R. CHEESEMAN, JR. J. A. MONTGOMERY, T. VREVEN, K. N. KUDIN, J. C. BURANT, J. M. MILLAM, S. S. IYENGAR, J. TOMASI, V. BARONE, B. MENNUCCI, M. COSSI, G. SCALMANI, N. REGA, G. A. PETERSSON, H. NAKATSUJI, M. HADA, M. EHARA, K. TOYOTA, R. FUKUDA, J. HASEGAWA, M. ISHIDA, T. NAKAJIMA, Y. HONDA, O. KITAO, H. NAKAI, M. KLENE, X. LI, J. E. KNOX, H. P. HRATCHIAN, J. B. CROSS, V. BAKKEN, C. ADAMO, J. JARAMILLO, R. GOMPERTS, R. E. STRATMANN, O. YAZYEV, A. J. AUSTIN, R. CAMMI, C. POMELLI, J. W. OCHTERSKI, P. Y. AYALA, K. MOROKUMA, G. A. VOTH, P. SALVADOR, J. J. DANNENBERG, V. G. ZAKRZEWSKI, S. DAPPRICH, A. D. DANIELS, M. C. STRAIN, O. FARKAS, D. K. MALICK, A. D. RABUCK, K. RAGHAVACHARI, J. B. FORESMAN, J. V. ORTIZ, Q. CUI, A. G. BABOUL, S. CLIFFORD, J. CIOŚLÓWSKI, B. B. STEFANOV, G. LIU, A. LIASHENKO, P. PISKORZ, I. KOMAROMI, R. L. MARTIN, D. J. FOX, T. KEITH, M. A. AL-LAHAM, C. Y. PENG, A. NANAYAKKARA, M. CHALLACOMBE, P. M. W. GILL, B. JOHNSON, W. CHEN, M. W. WONG, C. GONZALEZ, AND J. A. POPLER. *Gaussian 03, Revision E.01*. Gaussian, Inc., Wallingford, CT, 2004.
- [173] S. CALIFANO. *Vibrational States*. Wiley, London, 1976.
- [174] A. B. MYERS, R. A. HARRIS, AND R. A. MATHIES. **Resonance Raman excitation profiles of bacteriorhodopsin**. *J. Chem. Phys.*, **79**:603–613, 1983.
- [175] HARRY A. FRANK AND CAROL A. VIOLETTE. **Monomeric bacteriochlorophyll is required for the triplet energy transfer between the primary donor and the carotenoid in photosynthetic bacterial reaction centers**. *Biochim. Biophys. Acta*, **976**:222–232, 1989.
- [176] ROYA FARHOOSH, VEERADEJ CHYNWAT, RONALD GEBHARD, JOHAN LUGTENBURG, AND HARRY A. FRANK. **Triplet energy transfer between the primary donor and carotenoids in *Rhodobacter sphaeroides* R-26.1 reaction centers incorporated with spheroidene analogs having different extends of π -electron conjugation**. *Photochem. Photobiol.*, **66**:97–104, 1997.
- [177] SHELDON W. MAY AND JONG-YUAN KUO. **Preparation and Properties of Cobalt(II) Rubredoxin**. *Biochemistry*, **17**:3333–3338, 1978.
- [178] FADI BOU-ABDALLAH AND N. DENNIS CHASTEEN. **Spin concentration measurements of high-spin ($g' = 4.3$) rhombic iron(III) ions in biological samples: theory and application**. *J. Biol. Inorg. Chem.*, **13**:15–24, 2008.
- [179] MEINRAD GOOD AND MILAN VAŠÁK. **Spectroscopic Properties of the Cobalt(II)-Substituted α -Fragment of Rabbit Liver Metallothionein**. *Inorg. Chem.*, **25**:3328–3334, 1986.
- [180] HUUB J.M. DE GROOT, RONALD GEBHARD, INEKE VAN DER HOEF, ARNOLD J. HOFF, JOHAN LUGTENBURG, CAROL A. VIOLETTE, AND HARRY A. FRANK. **^{13}C magic angle spinning NMR evidence for a 15,15'-cis configuration of the spheroidene in the *Rhodobacter sphaeroides* photosynthetic reaction center**. *Biochemistry*, **31**:12446–12450, 1992.

Bibliography

Samenvatting

In bijna de helft van alle bekende eiwitten en enzymen maakt een overgangsmetaalion deel uit van de actieve plaats. Dit hangt ongetwijfeld samen met de flexibiliteit van de chemische coördinatie en van de elektronische structuur van overgangsmetaalionen. Deze elektronische structuur is zeer sterk verweven met de (geometrische) structuur van de actieve plaats en de functie. Informatie over de elektronische structuur van deze actieve centra kan worden verkregen met electron-paramagnetische-resonantie (EPR) spectroscopie.

In een typisch EPR experiment wordt de absorptie gemeten van microgolven van een vaste frequentie door het te bestuderen paramagnetische monster, terwijl het magneetveld wordt opgevoerd. De meest gebruikte frequentie is 9.5 GHz of X band. Er zijn echter legio paramagnetische systemen waarvoor EPR spectroscopie bij hogere frequentie nieuwe informatie oplevert, of waarvoor slechts de combinatie van EPR bij verschillende frequenties een complete interpretatie van de EPR spectra mogelijk maakt.

Bij high-spin overgangsmetaalionen, bijvoorbeeld, is als gevolg van de aanzienlijke spin-baan koppeling de ontaarding van de magnetische subniveaus reeds geheel of gedeeltelijk opgeheven zonder dat een magneetveld aanwezig is. Dit wordt aangeduid als de nulveldsplitsing. Indien de nulveldsplitsing voor een bepaald spinsysteem groter is dan de energie van de toegepaste microgolven, kan het onmogelijk worden om een overgang te induceren, of, als een EPR signaal kan worden waargenomen, is het moeilijk om op grond hiervan de absolute waarde van de nulveldsplitsing te bepalen.

Realisatie van EPR spectroscopie bij hogere microgolffrequenties, met name boven de 200 GHz, is niet eenvoudig, maar de afgelopen decennia zijn op dit gebied aanzienlijke vorderingen gemaakt. Een struikelblok is momenteel het verkrijgen van voldoende gevoeligheid bij hogere frequenties. Hoge gevoeligheid en stabiliteit van het EPR signaal gedurende de lange tijd die gemoeid is met het opnemen van een spectrum zijn in het bijzonder van belang als men hoog-frequente EPR spectra wil opnemen van een (bevroren) oplossing van eiwitten of enzymen, waarvan de actieve plaats een high-spin overgangsmetaalion bevat.

De nulveldsplitsing reflecteert de lokale elektronische structuur van de actieve plaats, maar vertaling naar informatie over de moleculaire energieniveaus en golf-

Samenvatting

functies is niet eenvoudig. De afgelopen jaren is veel vooruitgang geboekt met geavanceerde kwantum-chemische berekeningen, die deze vertaalslag kunnen maken, maar het werk hieraan is geenszins voltooid. Dit vormt een belangrijke motivatie voor de nauwkeurige bepaling van nulveldsplittingsparameters van verschillende overgangsmetaalionen, in verschillende coördinaties, te gebruiken als ijking voor de berekeningen, niet alleen in hun biologische omgeving, maar ook in modelcomplexen.

Hoofdstuk 2 laat zien dat, door gebruik te maken van een single-mode trilholt met hoge kwaliteitsfactor en een speciaal ontwerp van de bevestiging van de modulatiespoel, het met de in Leiden ontwikkelde 275.7 GHz (J band) EPR spectrometer zeer wel mogelijk is om continuous-wave (cw) spectra op te nemen van 20 nl bevroren oplossing van 1 mM Fe(III)-EDTA, een standaard coördinatiecomplex waarin een Fe^{3+} ion is gebonden in de high-spin vorm. De gevoeligheid en stabiliteit van de spectrometer worden verder geïllustreerd aan de hand van J-band EPR spectra van het eiwit rubredoxine. In de geoxideerde toestand bevat de actieve plaats van rubredoxine, dat een rol speelt bij electrontransport in diverse micro-organismen, een high-spin Fe^{3+} ion in een bij benadering tetraëdische coördinatie van vier zwavel atomen afkomstig van vier cysteine residuen. Opvallend zijn de zeer kleine verschillen in de nulveldsplittingsparameters die worden gevonden voor rubredoxines van verschillende organismen, wat illustreert hoe nauw elektronische structuur en functie met elkaar verweven zijn.

In Hoofdstuk 3 worden de mogelijkheden van de J-band spectrometer verder verkend. Onderwerp van studie is de actieve plaats van het eiwit desulforedoxine, dat sterk verwant is aan rubredoxine. In de literatuur is het X-band spectrum van de actieve plaats van desulforedoxine bekend, maar hieruit kan slechts een schatting worden gemaakt van de nulveldsplittingsparameters. Uit het J-band spectrum van desulforedoxine zijn deze parameters voor het high-spin Fe^{3+} centrum van desulforedoxine nauwkeurig bepaald. Een simulatie van het experimentele X-band spectrum met deze parameters laat kleine verschillen, orde van grootte 1 mT, zien tussen de berekende en gemeten resonantievelden. Natuurlijke variatie in de conformatie van de actieve plaatsen en de manier waarop deze wordt meegenomen in de simulatie speelt hierin zeer waarschijnlijk een rol.

Het Fe^{3+} ion in de actieve plaats van desulforedoxine kan worden gesubstitueerd met Co^{2+} en ook deze gesubstitueerde vorm is bestudeerd met EPR spectroscopie. Bij J band konden geen EPR signalen worden waargenomen, maar het X-band spectrum maakt het mogelijk de nulveldsplittingsparameters te schatten. Bovendien is getracht een EPR signaal van Co(II)-rubredoxine waar te nemen, maar dit is niet gelukt. De verschillen in structuur tussen de actieve plaatsen van rubredoxine en desulforedoxine zijn tamelijk subtiel en dit maakt de verschillen in de nulveldsplittingsparameters opvallend. Begrip van de oorsprong van deze verschillen kan alleen worden verkregen uit een volledige berekening van de elektronische structuur.

In Hoofdstuk 4 wordt gepulste ENDOR bij 94.9 GHz (W band) ingezet om de on-

gepaarde-electronendichtheid op de liganden van het complex $\text{Co}[(\text{SPPH}_2)(\text{SP}^i\text{Pr}_2)\text{N}]_2$ te verkennen. In dit complex zorgen twee bidentaalliganden voor een bij benadering tetraëdische zwavelcoördinatie van het centrale high-spin Co^{2+} ion. De symmetrie van het complex als geheel is slechts C_2 . De hyperfijninteractie met de fosforkernen in de liganden blijkt afhankelijk te zijn van de chemische groepen die aan het fosfor zijn gebonden. Met andere woorden, de Co-S bindingen zijn verschillend als gevolg van een subtiel verschil relatief ver van het Co(II)S_4 centrum.

In Hoofdstuk 5 wordt de studie beschreven van het complex $\text{Fe}[(\text{SPPH}_2)_2\text{N}]_2$ met EPR spectroscopie bij 275.7 GHz en 94.1 GHz. De combinatie van EPR spectroscopie bij J en W band maakt het mogelijk de nulveldsplittingsparameters van de twee conformaties, die het complex blijkt aan te nemen, zeer nauwkeurig te bepalen. De J-band EPR spectra van een kristal laten zien dat beide conformaties voorkomen in twee sites die ten opzichte van elkaar 90 graden gedraaid zijn om de z-as van het spin systeem. Zeer opmerkelijk is dat deze resultaten van hoogfrequente EPR spectroscopie niet compatibel zijn met de resultaten van Röntgen diffractie, die bij kamertemperatuur een eenheidscel laten zien met daarin slechts twee moleculen verbonden via een inversiecentrum.

Hoofdstuk 6 geeft de resultaten van cw EPR bij J band aan het eiwit transferrin, dat een belangrijke rol speelt in de ijzerstofwisseling van alle gewervelden. De meeste vormen van transferrin bestaan uit twee homologe lobben, die beide een high-spin Fe^{3+} ion zeer sterk, doch reversibel, kunnen binden. In de literatuur vindt men vele EPR spectra van transferrin, in verschillende vormen en onder verschillende omstandigheden, de oudste reeds uit 1963. De informatie die kan worden verkregen uit de X-band spectra is echter beperkt: de twee gebonden ijzerionen kunnen niet van elkaar worden onderscheiden en de voor ijzer gebonden aan transferrin zeer karakteristieke vorm van het X-band spectrum is niet begrepen. In J-band spectra van human serum transferrin kunnen duidelijk signalen van twee verschillende high-spin ijzercentra worden onderscheiden. Doordat ook J-band spectra zijn bestudeerd van twee mutanten van human serum transferrin, waarin via een lokale mutatie binding van ijzer door een van de twee lobben onmogelijk is gemaakt, is vastgesteld dat deze twee signalen inderdaad afkomstig zijn van de ijzerionen gebonden in de twee homologe lobben. Bovendien zijn de experimentele spectra van deze individuele ijzercentra begrepen en goed te simuleren.

In het werk dat in Hoofdstuk 7 wordt beschreven, wordt geen gebruik gemaakt van EPR spectroscopie, maar van resonante-Raman spectroscopie. Resonante-Raman spectroscopie wordt toegepast om de vibratiemodes van de cofactor sferoideen in het fotosynthetische reactiecentrum van *Rhodobacter sphaeroides* waar te nemen. Dit caroteen speelt vermoedelijk een rol in de bescherming van het reactiecentrum tegen overbelichting, maar het onderliggende mechanisme is niet volledig begrepen. In de literatuur bestaat geen consensus over de configuratie die het sferoideen aanneemt in het reactiecentrum. Vanzelfsprekend is kennis van deze configuratie nodig voor het begrip van de rol die het caroteen speelt in de fotoprotectie.

Samenvatting

In de afgelopen twee decennia is in onze onderzoeksgroep, in samenwerking met andere groepen, een methode ontwikkeld om de resonante-Raman spectra van sferoïdeen, die uiteraard afhankelijk zijn van de configuratie, te berekenen. Deze berekeningen zijn ontwikkeld en geïjkt met behulp van experimentele resonante-Raman spectra van isotoop-gelabeld sferoïdeen, dat was gereconstitueerd in het reactiecentrum van *Rb. sphaeroides* R26, een mutant die geen sferoïdeen produceert.

In Hoofdstuk 7 worden resonante-Raman spectra, gedetecteerd bij verschillende excitatiegolflengtes, van sferoïdeen in het wild-type reactiecentrum vergeleken met spectra van sferoïdeen gereconstitueerd in het reactiecentrum van de mutant R26. Combinatie van deze spectra met resultaten van de berekeningen heeft het mogelijk gemaakt vast te stellen dat de configuratie van sferoïdeen in het reactiecentrum van wild-type *Rb. sphaeroides* 15,15'-*cis* is. Bovendien is vastgesteld dat sferoïdeen in gereconstitueerde R26 reactiecentra voorkomt in twee configuraties, namelijk 15,15'-*cis* en 13,14'-*cis*.

List of publications

- Silvia Sottini, Guinevere Mathies, Peter Gast, Dimitrios Maganas, Panayotis Kyritsis and Edgar J. J. Groenen,
“A W-band pulsed EPR/ENDOR study of Co(II)S₄ coordination in the Co[(SPPPh₂)(SPiPr₂)N]₂ complex”,
Phys. Chem. Chem. Phys., 11 (2009) 6727-6732.
(Chapter 4 of this thesis)
- G. Mathies, H. Blok, J.A.J.M. Disselhorst, P. Gast, H. van der Meer, D.M. Miedema, R.M. Almeida, J.J.G. Moura, W.R. Hagen and E.J.J. Groenen,
“Continuous-wave EPR at 275 GHz: Application to high-spin Fe³⁺ systems”,
J. Magn. Res., 210 (2011) 126-132.
(Chapter 2 of this thesis)
- Guinevere Mathies, Marc C. van Hemert, Peter Gast, Karthick B. Sai Sankar Gupta, Harry A. Frank, Johan Lugtenburg, and Edgar J. J. Groenen,
“Configuration of Spheroidene in the Photosynthetic Reaction Center of *Rhodobacter sphaeroides*: A Comparison of Wild-Type and Reconstituted R26”,
J. Phys. Chem. A, 115:34 (2011) 9552-9556.
(Chapter 7 of this thesis)
- Guinevere Mathies, Rui M. Almeida, Peter Gast, José J. G. Moura and Edgar J. J. Groenen,
“Multi-frequency EPR study of Fe³⁺ and Co²⁺ in the active site of desulfuredoxin”,
in preparation.
(Chapter 3 of this thesis)
- Guinevere Mathies, Spyros Chatziefthimiou, Dimitrios Maganas, Yiannis Sanakis, Silvia Sottini, Panayotis Kyritsis and Edgar J. J. Groenen,
“High-frequency EPR study of the pseudo-tetrahedral high-spin Fe(II) complex Fe[(SPPPh₂)₂N]₂”,
in preparation.
(Chapter 5 of this thesis)

List of publications

- Guinevere Mathies, Ashley N. Steere, N. Dennis Chasteen, Anne B. Mason and Edgar J. J. Groenen,
“The two Fe³⁺ binding sites in human serum transferrin distinguished by high-frequency EPR”,
in preparation.
(Chapter 6 of this thesis)

Curriculum vitae

van Guinevere Mathies, geboren te Leiden op 1 juli 1981.

Na het behalen van mijn gymnasiumdiploma op het Herbert Vissers College te Nieuw-Vennep in juni 1999 begon ik in september van dat jaar met de studie natuurkunde aan de Universiteit Leiden. Een jaar later behaalde ik mijn propedeuse. In het voorjaar van 2002 maakte ik voor het eerst kennis met de Molecular Nano-Optics and Spins (MoNOS) groep tijdens de Introductie Experimentele Natuurkunde. In de groep van prof. dr. Michel Orrit werkte ik onder andere aan de fluorescentie karakteristiek van rhodamine 6G. Ik koos voor de afstudeerrichting Experimentele Natuurkunde en het eerste deel van de anderhalf jaar experimentele onderzoeksstage bracht ik door in de groep van prof. dr. Joost Frenken en dr. Tjerk Oosterkamp. Ik werkte aan een simulatie van de beweging van de tip van de scanning tunneling microscoop (STM), zowel in het tijddomein als in het frequentiedomein. Het tweede deel van de experimentele onderzoeksstage voerde ik uit in de groep van prof. dr. Shimon Weiss aan de University of California, Los Angeles. Met behulp van totale-interne-reflectie fluorescentie microscopie (TIRFM) bleek het mogelijk de laterale diffusie van individuele van quantum dots voorziene lipiden in lipide dubbellagen waar te nemen. De analyse van de data verrichtte ik later Leiden in de groep van prof. dr. Thomas Schmidt. Tijdens mijn studietijd was ik assistent bij het eerstejaars natuurkundig practicum. Als lid van de reiscommissie van studievereniging De Leidsche Flesch organiseerde ik mede de studiereis van 2002 naar Zwitserland. In oktober 2005 studeerde ik af in Leiden.

In het voorjaar van 2006 begon ik met een promotieonderzoek onder leiding van prof. dr. Thomas Röckmann en dr. Geert-Jan Roelofs bij de vakgroep Atmosferische Fysica en Chemie op het Institute of Marine and Atmospheric Research (IMAU) van de Universiteit Utrecht. Hier onderzocht ik de invloed van eigenschappen van aërosol op de vorming van wolken, zowel met behulp van computersimulaties als met behulp van experimentele simulaties in de wolkenkamer van ECN in Petten. Om verschillende redenen heb ik in de winter van 2007 besloten om met dit onderzoek te stoppen. In het jaar dat ik bij het IMAU werkte gaf ik het werkcollege kwantummechanica 1. Hierna heb ik tijdelijk gewerkt op de IT afdeling van zorginstelling Careyn te Zoetermeer.

In september 2007 begon ik aan mijn promotieonderzoek in de MoNOS groep

Curriculum vitae

in Leiden, onder leiding van prof. dr. Edgar Groenen. De belangrijkste resultaten hiervan zijn opgenomen in dit proefschrift. Ik heb mijn werk gepresenteerd op conferenties in Brussel (Juni 2010, 18th Meeting of the Benelux EPR Society), Veldhoven (Maart 2011, Scientific meeting on Chemistry related to Physics & Material Sciences, studiegroep Spectroscopie en Theorie) en Frankfurt (Augustus 2011, EUROMAR/8th European Federation of EPR Groups Meeting). Bovendien heb ik seminars gegeven bij het Institute for Molecules and Materials, RU Nijmegen, het Francis Bitter Magnet Laboratory, MIT, Cambridge, MA, het MPI für Bioanorganische Chemie, Mülheim an der Ruhr en het Helmholtz Zentrum Berlin. Tijdens mijn promotie heb ik geassisteerd bij het eerstejaars natuurkundig practicum en verzorgde ik het werkcollege kwantummechanica 2. Daarnaast heb ik een bachelorstudent en een masterstudent begeleid tijdens hun onderzoeksstage in de MoNOS groep. Bovendien was ik lid van het promovendiplatform van de Casimir Research School, dat onder meer belast is met de organisatie van de tweejaarlijkse Casimir Spring School.

Acknowledgement

Een promotieonderzoek succesvol afronden doe je niet alleen. Graag noem ik de mensen die een belangrijke rol hebben gespeeld.

Allereerst wil ik mijn promotor, Edgar Groenen, bedanken voor zijn vertrouwen in mij en voor het haarfijn weten aan te wijzen waar de gaten zitten.

Ik wil ook graag Peter Gast bedanken voor het leren omgaan met cryogene vloeistoffen, de in Leiden ontwikkelde spectrometers en gevoelige biologische monsters, voor vruchtbare discussie, het advies “Ga het nou maar gewoon meten!” en hulp bij experimenten op zondag; Huib Blok, voor hulp met mijn eerste J-band experimenten en uitleg; Jos Disselhorst, voor zijn technische ondersteuning, die veel meer is dan dat, het bier aan het einde van Tweede Paasdag 2011, het op het oog rechtbuigen van transfer lines en de introductie fijnmechanica op vroege dinsdagochtenden; Harmen van der Meer, voor zijn fantastische fijnmechanische vaardigheden, het voor de zoveelste keer in en uit elkaar halen van de nieuwe insert en het maken van weer een nieuwe modulatiespoel. And, of course, I would like to thank everyone else in the MoNOS group.

Zonder goede ondersteuning schiet het onderzoek niet op. Ik wil daarom bedanken: Arno van Amersfoort, voor het voorkomen van computerfrustraties, Frans Folst, voor zijn kwartsbewerkingskwaliteiten, Hans van Kuyk en Wilfred van der Geest, voor het op zeer korte termijn vullen van heliumvaten, Henriëtte van Leeuwen, voor haar secretariële ondersteuning en René Overgaauw, voor fijn soldeerwerk.

Tot slot wil ik mijn ouders bedanken, voor alle dingen die ouders tot goede ouders maken; Susan, Yung Chin, omdat jullie zijn wie jullie zijn; iedereen met wie ik zo veel volleybal, of heb gevolleybald, voor alle trainingen, wedstrijden en spelplezier, en vriendschap. Zonder jullie had dit boekje niet tot stand kunnen komen.

Acknowledgement
